

**Scanning tunneling microscopy study of
Bi₂Se₃(0001) and of FeSe and Bi
nanostructures on Bi₂Se₃(0001)**

Dissertation

zur Erlangung des Doktorgrades der Naturwissenschaften
(Dr. rer. nat.)

der

Naturwissenschaftlichen Fakultät II
Chemie, Physik und Mathematik

der Martin-Luther-Universität
Halle-Wittenberg,

vorgelegt von

Herrn **Vasilii Sevriuk**

geb. am 29.12.1989 in Leningrad (Sankt Petersburg), Russland

Gutachter:

- PD Dr. Dirk Sander
- Prof. Dr. Wolf Widdra
- Prof. Dr. Claus Schneider

Verteidigungsdatum: 26.06.2017

Contents

1	Introduction	1
2	Scanning tunneling microscopy for the study of topological insulators and superconductors	5
2.1	Scanning tunneling microscopy (STM) and spectroscopy (STS)	5
2.2	Topological insulators	8
2.2.1	Bi ₂ Se ₃ and Bi bilayers	11
2.3	Unconventional superconductors	11
2.3.1	Conventional superconductors	12
2.3.2	Cuprates and iron-based unconventional superconductors . .	13
2.3.3	FeSe	15
3	Experimental setup	18
3.1	Cryogenic Scanning Tunneling Microscope	18
3.2	New preparation chamber	23
4	Preparation and characterization of Bi₂Se₃(0001)	26
4.1	<i>In situ</i> and <i>ex situ</i> cleavage	28
4.2	Sample preparation by sputtering-annealing cycles	29
4.3	Surface characterization by low-energy electron diffraction (LEED) and Auger electron spectroscopy (AES)	31
4.4	Scanning tunneling microscopy and spectroscopy of Bi ₂ Se ₃	32
5	FeSe on Bi₂Se₃(0001)	35
5.1	Preparation of FeSe nanocrystals on Bi ₂ Se ₃ (0001)	36
5.2	LEED and AES characterization	36
5.3	STM and STS study of FeSe	38
6	Bi bilayer on Bi₂Se₃(0001)	43
6.1	Bi bilayer preparation by atomic hydrogen exposure	43
6.2	STM topography of the Bi bilayer surface	45
6.3	STS results of the Bi bilayer	45

7 Discussion	47
7.1 Tuning the Bi ₂ Se ₃ thermal annealing procedure	47
7.2 Bi ₂ Se ₃ surface states	50
7.3 Formation of FeSe nanocrystals on the Bi ₂ Se ₃ surface	52
7.4 FeSe nanocrystal: in-plane crystal structure	54
7.5 FeSe on Bi ₂ Se ₃ : a candidate for an unconventional superconductor .	56
8 Conclusion and Outlook	61
Bibliography	65
Publications and conference contributions	77
A Photographs of the STM system	79
B Example of a Matrix script and a LabVIEW program	83
Acknowledgements	87
Curriculum vitae	89

Chapter 1

Introduction

Nowadays topological insulators (TI) attract a lot of attention due to their unique physical properties and due to a novelty of the phase of matter, which they represent [1–4]. This phase of matter is not only different from classical liquid, gas and solid states, but also differs from ferromagnetic or superconducting phases. This phase of matter has no relationship with symmetry breaking, in contrast to second order phase transitions. In a TI certain fundamental physical properties are preserved and cannot be changed unless a phase transition happens [2], which is the essential criteria for the phase. This phase is defined by the topological features of the electronic band structure. Topology is a field of mathematics, which studies properties of different spaces under continuous transformations with no regard to their metrics. Electronic band structures can be considered as such spaces. Thus, materials with different topological classes of their electronic band structure are attributed to different topological phases.

Topological insulators are closely related to the quantum Hall effect (QHE) [5, 6]. In a 2D class of TI, as well as in QHE, there are so-called topologically protected edge states [7] (the topologically protected surface states are 3D analogs of these [8]).

The topologically protected states are the main feature of TI. Their main characteristics are: robustness against surface modifications and disorder, strong electron spin-orbit coupling, and linear electron dispersion [2]. Linear electron dispersion leads to the formation of a double cone in the electronic band structure, a so-called Dirac cone results. These properties make TI a promising candidate for spintronics and quantum computation [9, 10].

New opportunities for spintronics and quantum computation arise from an interplay between TI and other phenomena, such as magnetism. This may lead to a strong control of skyrmions by electric field [11]. In combination with superconductors (SC), so-called Majorana bound states may be observed [12, 13]. Thus, due to their unique surface properties, 3D TIs have a substantial potential as substrates. Thus the development and understanding of TI surface preparation with a perfect atomic structure and a defined electronic structure is mandatory.

Bi_2Se_3 is a promising example of a TI substrate due to its relatively simple atomic structure and well-known electronic properties [2, 14, 15]. A usual technique for the $\text{Bi}_2\text{Se}_3(0001)$ surface preparation is cleavage [16–18]. However, cleavage cannot be applied for thin crystals and films. Also, multiple cleavage processes can lead to a large amount of wasted material. One alternative is to apply methods which are also used for the preparation of metallic samples, such as ion sputtering and annealing [19]. One of the questions I answer in my thesis: is there any difference between cleaved Bi_2Se_3 and a surface prepared by sputtering and annealing? We

will see that both preparations provide comparable results.

Topological insulators are especially interesting in combination with other quantum phenomena. Thus we study the possibility to grow superconducting and magnetic thin films on Bi_2Se_3 substrates.

Epitaxial growth generally requires the supply of the film material. One possible simplification is to use atoms, which are supplied by the substrate. As an example we investigated if it is possible to grow FeSe on the Bi_2Se_3 surface without Se deposition and what would be the material characteristics in this case? As I will demonstrate, epitaxial FeSe on $\text{Bi}_2\text{Se}_3(0001)$ can be grown successfully by this approach.

FeSe attracts a lot of interest as it is a base material of so-called iron-based SCs [20, 21], new materials, which challenging for SC theory and industrial applications. Iron-based SCs are interesting, because they are a new second big family of unconventional SCs, in addition to the cuprate SCs. The comparison of the theoretical and experimental results obtained with these two families opens new insights to understand better the physical origin and parameters of the SC state. FeSe thin films attracted tremendous interest after the report of an unexpectedly high T_c of FeSe unit-cell thin films on a SrTiO_3 (STO) substrate [22, 23]. The reported T_c as high as 100 K [23] was even more surprising as bulk FeSe has a $T_c = 8.5$ K [24]. A discussion of the role of epitaxial strain, defect formation and substrate electronic bands on T_c was started. However, the nature of the high T_c is still not clear. The question arises if FeSe grown on $\text{Bi}_2\text{Se}_3(0001)$ is a high-temperature unconventional SC? My work shows that the grown FeSe nanocrystal has a SC gap-like feature in the electron density of states (DOS). This result in connection with theoretical studies suggests that SC in FeSe is plausible. I provide new insights to this topic.

The interplay between FeSe and Bi_2Se_3 can lead to Majorana bound states [12, 13], which are extremely important for quantum computation [25]. Majorana bound states are also called Majorana zero modes. They are a special type of excitations in SC, where the hole excitation is not distinguishable from electron excitation. Thus, the particle and anti-particle behave similarly, that is why these objects are also called partihole [26]. Majorana bound states have unusual quantum statistics, which helps to create and store qubits nonlocally, and this helps to make qubits more robust. These interesting objects can be found in the interplay of SC and TI, or in some unconventional SCs, where they occur in vortices [26].

Another interesting possibility is the Bi bilayer (BL), which was shown to be an example of a 2D topological insulator [27, 28]. However, due to the compressive strain in Bi BL on $\text{Bi}_2\text{Se}_3(0001)$ (the lattice mismatch is around -9%), the Bi BL band gap is closed and Bi BL becomes a metal [29]. But the Bi BL is also interesting for future research on a MnBi alloy on the Bi_2Se_3 surface. This compound is a candidate for skyrmion spin texture [30]. I prepared Bi BL on Bi_2Se_3 by atomic hydrogen etching [31] without need of supplying Bi.

All these propositions lay in a field of planar technology and surface studies [32, 33]. One key instrument of surface science is the scanning tunneling microscope (STM). Since its invention in the 1980's by Binnig and Rohrer [34–36], STM initiated the evergrowing field of scanning probe microscopy (SPM). SPM is the only well-established technique which allows to address single atoms and, at the same time, to study surfaces and their electronic properties on the nanometer scale. Due to its atomic resolution [34] and the possibility to probe the density of states (DOS) by scanning tunneling spectroscopy (STS) [37, 38], STM is an important tool for all

surface science studies, and I employed it in my thesis.

My research was performed using a low-temperature UHV STM (Omicron) with a Janis helium bath cryostat. Due to the larger complexity of the Bi_2Se_3 substrate preparation as compared to metal surfaces used previously [39, 40], it was reasonably assumed that the sample preparation and its characterization would be a demanding and complicated task.

Thus, the existing STM system was significantly extended to include supplementary surface science techniques *in situ* for the low-temperature STM. A new preparation chamber with LEED, AES facilities and different stages for sputtering, annealing and cleavage was installed by me. The chamber base pressure is as low as 3×10^{-11} mbar, significantly better than it was in the previous preparation chamber. This powerful combination of complementary techniques allows to prepare also complex, multielement substrates and nanostructures reliably and to answer the questions raised above.

This thesis is structured as follows. Chapter 2 introduces basic concepts of STM, TI and unconventional SC. A full description of the used STM and the new preparation chamber is given in chapter 3. The preparation of the Bi_2Se_3 surface, FeSe and Bi BL and corresponding STM, LEED and AES results are reported in chapters 4, 5 and 6, respectively. A detailed discussion is given in chapter 7. The STM results for different preparations of $\text{Bi}_2\text{Se}_3(0001)$ are given in section 7.1. A comparison of the STS result on the prepared Bi_2Se_3 surface with photoemission data is given in section 7.2. The formation and the atomic structure of the FeSe nanocrystals are analyzed in section 7.3 and section 7.4. Section 7.5 presents the analysis of the STS results on epitaxial FeSe nanocrystals with conjoint theoretical study and photoemission data. A conclusion of the thesis and an outlook are given in chapter 8.

Chapter 2

Scanning tunneling microscopy for the study of topological insulators and superconductors

In this thesis I used the 3D topological insulator Bi_2Se_3 as a substrate. I also studied two types of nanostructures grown on the $\text{Bi}_2\text{Se}_3(0001)$ surface: FeSe nanoislands and Bi bilayer (BL) films. The main experimental technique, which was used in this thesis, is scanning tunneling microscopy (STM).

This chapter is dedicated to the basic theory and some illustrative experimental results which are useful for a better understanding of the STM experiment, the studied materials, the results and their later discussion. I confine the presentation to a brief exposition. Comprehensive theory and experimental reviews can be found in the references, which are given in this chapter.

This chapter is arranged in three separate sections. The first section is dedicated to STM basics. The second section introduces topological insulators and gives some information on Bi_2Se_3 and Bi BL. I discuss in the third section unconventional iron-based superconductivity, focussing on FeSe bulk and thin films.

2.1 Scanning tunneling microscopy (STM) and spectroscopy (STS)

In my thesis I present STM constant current images and scanning tunneling spectroscopy (STS) curves and images. The goal of this section is to convey the basic theory of STM, to unravel the experimental process, and to illustrate the connection between STS data on the differential conductance and the electron density of states (DOS) of the sample.

STM relies on the quantum phenomenon of tunneling. The tunneling effect is an example of quantum mechanics at work. For an electron, according to classical physics, it is impossible to penetrate a potential barrier U_b with an energy lower than the barrier height $E < U_b$. However, for an electron wave function we can find a solution which corresponds to a penetration of the barrier. The probability P of the penetration, which is also known as the transmission coefficient, is for a step-like barrier:

$$P = e^{-2kd}, \quad (2.1)$$

where d is the thickness (spatial extent) of the barrier and

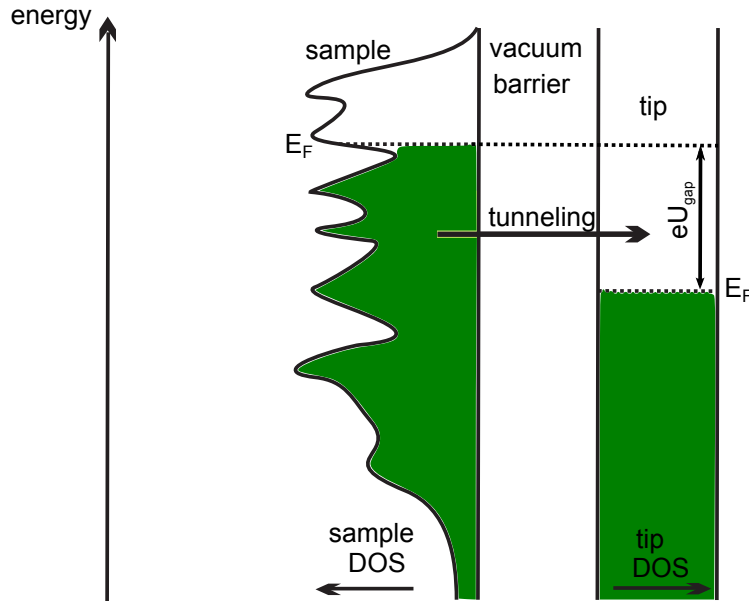


Figure 2.1: Schematic view of the tip-sample tunneling process. The tip electronic density of states (DOS) is idealized by a constant function. Occupied states are marked green. The tunneling voltage is negative with respect to sample, which leads to electron tunneling from the sample to the tip.

$$k = \frac{\sqrt{2m(U_b - E)}}{\hbar}, \quad (2.2)$$

is the decay constant. If we consider a vacuum gap between two pieces of the same material as the barrier for an electron at the Fermi level, then U_b equals the work function of the material ϕ .

I consider the STM tunneling process with an applied bias U_{gap} , see Fig. 2.1. If we assume that both U_{gap} and the difference between the work function of the sample and the tip are negligible in comparison with the absolute value of the mean tip-sample work function $\phi = \frac{1}{2}(\phi_{tip} + \phi_{sample})$ we can rewrite the decay constant as:

$$k = \frac{\sqrt{2m\phi}}{\hbar}. \quad (2.3)$$

The typical work function lies in the range of 3 – 6 eV [41] which gives $k \approx 10 \text{ nm}^{-1}$. This means that the probability of the penetration (see Eq. 2.10) decreases one order of magnitude per 1 Å change of the barrier thickness. This estimation shows that the apex of the STM tip is almost exclusively responsible for the tip-sample tunneling. This is a key aspect to reach high spatial resolution in STM.

For more complicated and not symmetric shapes of the barrier, there is the Wentzel-Kramers-Brillouin (WKB) approximation [41, 42]. Here, the spatial dependence of the decay constant is considered as:

$$P = \exp\left(\int_{z_1}^{z_2} k(z) dz\right), \quad (2.4)$$

where z_1 and z_2 are the edges of the barrier.

With these formulas we can understand the general dependence of the tip-sample tunneling conductance, but what are the absolute values? The question can be answered approximately with the application of Landauer theory [41]. Landauer made a calculations for a one-dimensional free-electron gas in a square shape potential [43], and this approximation shows nice agreement with experiments for nearly free-electron metals [44, 45] and it can be generalized.

The most far-reaching result, in my opinion, for the STM theory has been obtained by Bardeen twenty years before the STM was developed. After the first experiments on the verification of the BCS theory done by Giaever [46] and Nicol, Shapiro and Smith [47], Bardeen started to develop the many-body theory of tunneling which leads to [41, 48]:

$$I = \frac{4\pi e}{\hbar} \int_0^{eU_{gap}} \rho_{sample}(E_{F,s} + \epsilon) \rho_{tip}(E_{F,t} - eU_{gap} + \epsilon) T(\epsilon, eU_{gap}) d\epsilon, \quad (2.5)$$

where $\rho_{sample/tip}$ is the tip/sample density of states respectively, U_{gap} is the applied voltage and $T(\epsilon, eU_{gap})$ is the transmission coefficient, which is given by the tunneling matrix element as defined by:

$$T(\epsilon, eU_{gap}) = -\frac{\hbar^2}{2m} \int_{\Sigma} (\chi \nabla \psi - \psi \nabla \chi) dS, \quad (2.6)$$

where ψ is an electronic wave function of the sample, χ is a wave function of the tip, and the surface integral is taken on a separation surface, which is located roughly in the middle of the gap [41].

The suitability of the formula 2.5 for a flat sample and a tip wave function characterized by an s -state was shown later by Tersoff and Hamann [38, 49]. The Tersoff-Hamann model became the “standard” model for STM theory. Within this theory it is also necessary to consider ρ_{sample} as a function of the distance to the center of the tip wave function. The so-called local density of states (LDOS) of the sample at the tip position needs to be considered.

The Tersoff-Hamann model works well down to surface feature sizes of the order of 0.3 nm [38, 49]. That is the reason why this model underestimates the atomic corrugation observed in experiments [50, 51]. In an effort to obtain better agreement between experiment and theory more complicated models for tip electronic states were considered [52–55].

In general, taking into account d - or p - tip states gives better agreement with experimental results. Four types of the tip wave function with corresponding tunneling matrix elements are given in table 2.1 [41].

Here, C (and $C_{ij}^{o/e}$) are coefficients which can be obtained by first-principles calculations, $\kappa_{0/1}$ are the spherical Bessel functions and \mathbf{r}_0 is a position of the tip wave function. This results show us that, if the tip state has orbital lobes with different phases, the spatial derivative of the sample wave function contributes. In such a case, the spatial variations of the sample wave function and DOS are amplified.

A more comprehensive description of tunneling can be obtained on the basis of the Landauer-Büttiker formalism [43, 56, 57]. It includes the general aspects of electron transport in mesoscopic structures, and it treats tunneling as a scattering problem. It introduces a concept of including independent, different tunneling

channels. It has been successfully applied to STM theory [58–60].

However, the basic Tersoff-Hamann model is sufficient for most cases. Even the transmission coefficient $T(\epsilon, eU_{gap})$ dependence on U_{gap} is often negligible. Within a simple picture of the tip DOS (see Fig. 2.1), the differentiation of Eq. 2.5 gives:

$$\frac{dI}{dV}(U_{gap}) = \frac{4\pi e}{\hbar} \rho_{sample}(E_{F,s} + eU_{gap}) \rho_{tip}(E_{F,t}) T(eU_{gap}, eU_{gap}). \quad (2.7)$$

This expression shows that under these assumptions the dI/dV signal is proportional to the sample LDOS. dI/dV curves are obtained experimentally by a lock-in technique, described in the next chapter. Thus, STM differential conductance spectroscopy gives direct information about the LDOS on the atomic scale.

Equation 2.7 is valid only if the tip DOS has the idealized step-like structure (see Fig. 2.1), which cannot be taken for granted. A preparation of the tip apex before and during the STS measurements is usually required. The preparation method involves a fairly empirical processes of modifying the tip apex *in situ* by voltage pulses and controlled tip indentations [41, 61]. The same procedure is also used to clean the tip apex or to change its shape and remove multiple tips [52].

A comprehensive review of STM theory and a complete description of experimental aspects can be found in numerous textbooks [41, 61–63].

2.2 Topological insulators

Topological insulators are distinguished from other insulators by a topology of the electronic band structure [2, 64, 65]. Different topologies are general features of different classes of topological spaces (a generalization of metric spaces), which are distinguished by the possibility to continuously transform one space into another [66]. In this way, the metric properties of the spaces are not important. One example are surfaces of 3D bodies, as shown in Fig. 2.2.

A donut in this case is not distinguishable from a cup, but completely different from a sphere, see Fig. 2.2. We cannot transform the donut to the sphere without closing a hole in it, which breaks a continuous transformation.

Most TI and their electronic band structure were already well-known [67]. The concept of TI is important as it not only defines a new kind of matter, but it also leads to a new type of phase classification.

Tip state	Wave function	Matrix element
s	$C_{00}\kappa_0(k \mathbf{r} - \mathbf{r}_0)\sqrt{\frac{1}{4\pi}}$	$\frac{2\pi C\hbar^2}{km}\psi(\mathbf{r}_0)$
p_z	$C_{10}\kappa_1(k \mathbf{r} - \mathbf{r}_0)\sqrt{\frac{3}{4\pi}}\frac{z-z_0}{ \mathbf{r}-\mathbf{r}_0 }$	$\frac{2\pi C\hbar^2}{km}\frac{\partial\psi}{\partial z}(\mathbf{r}_0)$
p_x	$C_{11}^o\kappa_1(k \mathbf{r} - \mathbf{r}_0)\sqrt{\frac{3}{4\pi}}\frac{x-x_0}{ \mathbf{r}-\mathbf{r}_0 }$	$\frac{2\pi C\hbar^2}{km}\frac{\partial\psi}{\partial x}(\mathbf{r}_0)$
p_y	$C_{11}^e\kappa_1(k \mathbf{r} - \mathbf{r}_0)\sqrt{\frac{3}{4\pi}}\frac{y-y_0}{ \mathbf{r}-\mathbf{r}_0 }$	$\frac{2\pi C\hbar^2}{km}\frac{\partial\psi}{\partial y}(\mathbf{r}_0)$

Table 2.1: Examples of the tip wave function with calculated matrix element for the tunneling current, see Eq. 2.6 [41].

It is fundamentally different from the well-known Landau symmetry-breaking theory [68]. This theory explains a phase transition with respect to a local order parameter, which breaks a symmetry of a ground state of a system. A local magnetization in magnetic materials is a good example of the local order parameter. This parameter can be defined in a single crystal unit cell and at a temperature lower than the Curie temperature, when the average local magnetization of the crystal is not zero, corresponding rotation symmetry is broken [69]. However, no symmetry is broken in TI. TI is the new phase of matter in the sense that it has some features which are particularly connected to this phase and cannot be demolished without phase transitions.

A TI has close relationships with the quantum Hall effect (QHE) [5, 6, 70]. In the QHE a sample with a two-dimensional (2D) electron gas is held under high magnetic field, which gives rise to the formation of Landau levels [71]. These levels form an insulating state [72] inside the sample, while a nondissipative current is flowing along the edge, which means zero resistance at zero temperature. The current appears due to the conducting edge states. These states are formed due to the evolution of Landau levels at the edges of the sample [5]. From the experiment it is well established that the Hall conductivity in this case varies in a step-like manner with increasing magnetic field and equals:

$$\sigma_{xy} = \frac{e^2}{h}n, \quad (2.8)$$

where n is an integer number, which is also the number of conducting edge channels and the number of occupied Landau levels in the bulk of the sample.

As was explained by Thouless, Kohmoto, Nightingale and den Nijs (TKNN) [73, 74], the number n in the Hall conductivity formula 2.8 is identical to a topological invariant Z , which depends on a “geometry” of the band structure. TKNN theory showed that this invariant is an instrument to work out differences between quantum Hall states (the states with different number of the edge conducting channels are also different from a view of topology) and the normal insulator state. The TKNN theory tells us that we cannot transform a quantum Hall state (QHS) ($Z=1$) to the normal insulator ($Z=0$), vacuum for example, without changing the topology of the band structure and thus closing the band gap. This is why there are metallic states on the edge of the QHS, which are topologically protected.

The QHE only occurs when time reversal symmetry is broken (by the magnetic field). However, it was shown, that the quantum spin-Hall state (QSHS) can also occur due to spin-orbit interaction in semiconductors [75, 76] and in graphene [77], where the time reversal symmetry is not broken. This establishes another topological class of insulators. In this case, the TKNN invariant is zero. The spin edge current in the QSHS is a composition of opposite spin currents of the QHE. This renders

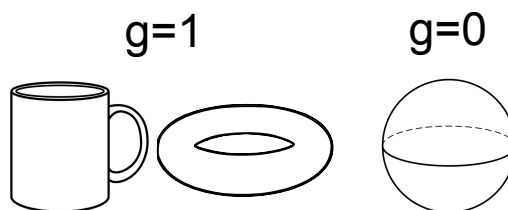


Figure 2.2: Schematic of a cup, a donut and a sphere, with denoted number of holes g .

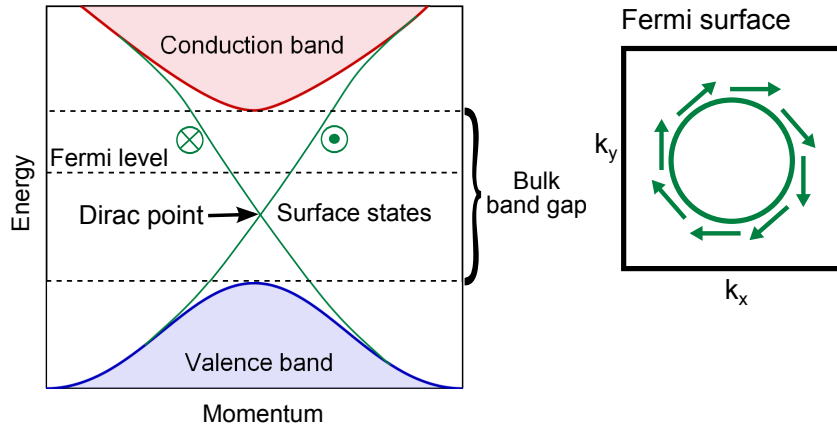


Figure 2.3: An idealized band structure of a topological insulator [79]. The topologically protected surface states are within the bulk band gap. These states have spin-momentum locking (the direction of the electron spin is strongly constrained by the direction of its momentum), which is denoted by green arrows (and \odot , \otimes), and the electron dispersion is linear in first approximation. Such dispersion means that the electrons behave like a massless Dirac fermion. Thus, this TI protected surface states form the so-called Dirac cone. The point where spin-up and spin-down states cross is the Dirac point. The direction of the spin is always perpendicular to the momentum, but stays in the XY plane, so it looks like the spin is wrapping around the Dirac cone, that is why it often called helical Dirac cone.

spin-up and spin-down currents of the QSHS with opposite values of Z , which are not zero, but the sum is zero.

Hence another classification is needed, which is based on a study of a behaviour in the half Brillouin zone (where k and $-k$ are never both included) of a function:

$$f = \langle u_m(k) | \theta | u_n(k) \rangle, \quad (2.9)$$

where $u_m(k)$, $u_n(k)$ is an occupied Bloch functions, and θ is time reversal anti-unitary operator. The full theory can be found in the work of C. L. Kane and E. J. Mele [78]. This new topological invariant is usually denoted Z_2 . It is 0 for normal insulators and 1 for topological insulators.

The easy rule to understand whether the surface (or edge) state of the insulator is topologically protected, and thus whether the insulator is a TI, is to count how many times this band crosses the Fermi energy as a function of wave vector from the center to the edge of the first Brillouin zone. If it crosses an odd number of times, this indicates a TI. Other more complicated features and a detailed description of the main aspects of the TI theory are given in numerous reviews [2, 64, 65] and textbooks [80, 81].

The bulk band structure of a 3D TI is similar to that of a usual insulator, and all interesting physics is happening at the surface. The surface states of TI are the hallmark of the TI phase, and so they cannot be destroyed without destroying the phase itself. These surface states are also unique due to the fact that they appear in a shape of the helical Dirac cone in the electronic band structure [2], see Fig. 2.3. This means that electrons in these states have a linear dispersion and strong spin-orbit coupling.

2.2.1 Bi₂Se₃ and Bi bilayers

Bi₂Se₃ is a model system due to its electronic structure, which is characterized by a single Dirac cone at the Γ -point on the surface [14], see Fig. 2.4. It has a bulk band gap from -0.1 to -0.5 eV [15]. The topology of the electronic structure of this material is not trivial due to the inversion between the different parity p-states of Bi and Se atoms induced by spin-orbit coupling (SOC) [14]. The energy position of the Dirac point is found in experiments to be located below the Fermi energy at -0.3 eV [15]. This energy position is ascribed to n-doping, resulting from Se vacancies [15].

The combination of the 3D TI surface with epitaxial films and nanostructures are interesting subjects, which I addressed in my thesis. One of the studied systems is the Bi bilayer. Theory proposed that the free-standing ultrathin Bi film (up to three BL) is a 2D TI [27, 28]. However, in experiments the BL is grown on a substrate [82–85], in our case Bi₂Se₃(0001). Thus, theory should include the substrate to consider possible effects of strain, charge transfer and atomic coordination. Theory proposed that due to compressive strain between Bi BL and Bi₂Se₃(0001) (the lattice mismatch is around -9%), the Bi BL band gap is closed, and the Bi BL becomes a metal [29]. Also some experimental and theoretical results show that the Bi BL does not affect the Bi₂Se₃ surface states. However, due to charge transfer an additional Dirac cone appears in the Bi BL electronic structure with the Dirac point in proximity to the Fermi level [15, 86].

2.3 Unconventional superconductors

FeSe thin films and nanostructures are possible candidates for a high critical temperature in superconductivity [22, 23, 87, 88]. FeSe is also interesting in combination with 3D TI, because this combination may lead to a so-called topological SC and Majorana bound states, which are potential candidates for use in quantum computation [12, 13]. FeSe belongs to a family of unconventional superconductors. The superconducting nature in these materials is not fully understood yet. Here, I discuss some basic concepts of unconventional SCs to underline the difference between

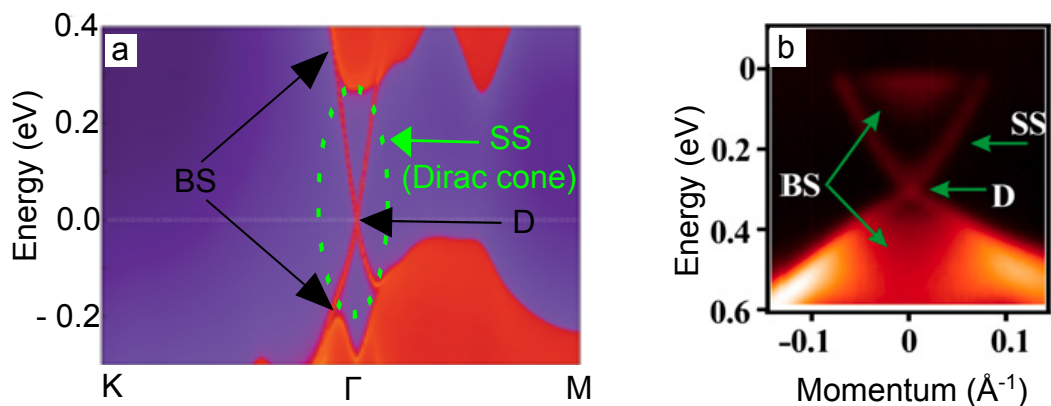


Figure 2.4: (a) Calculated band structure of pristine Bi₂Se₃, as presented in reference [14], (b) angle-resolved photoemission spectroscopy (ARPES) result from reference [15], with denoted bulk states (BS), surface states (SS) and Dirac point (D).

conventional and unconventional SC, to explain STM experiments on SCs and to show future prospects of FeSe.

2.3.1 Conventional superconductors

The first microscopic theory of SC was established by Bardeen, Cooper and Schrieffer (BCS theory) [89]. This theory still represents the paradigm for an understanding of SC.

BCS theory was developed on the assumption of an attractive electron-electron interaction in the form of an electron-phonon coupling. For a SC like aluminum (Al) or zinc (Zn) the results of this theory are in agreement with experiment. These materials are called conventional SC. The idea of electron-phonon interaction was inspired by the isotope effect [90]. Basically one can understand conventional SC by imagining that one electron emits a phonon which is absorbed by another electron. This process leads to a momentum exchange between the electrons. If the attraction provided by the phonon exchange is stronger than the intrinsic repulsion between electrons, at least in a small energy window, then this mechanism leads to the formation of Cooper pairs, and to a breakdown of the Fermi liquid behaviour of metals [90]. Classical SC theory is well described in numerous textbooks [90–92].

Next we will discuss some BCS theory predictions, which can be probed by STM. One strength of STM is its potential to measure the electronic local density of states of the sample surface. In general SC is characterized by the SC gap (Δ_{SC}) in the DOS. The size of this gap is proportional to the strength of the electron pairing. According to BCS theory only electrons near the Fermi surface can take part in the effective attractive interaction. Consequently, the SC gap is situated near the Fermi level.

But the presence of a gap in the DOS is not the ultimate sign of the SC state. A gap in the DOS, as probed by differential conductance spectroscopy in STM, can be produced by a dielectric state of the sample surface or of the tip apex. One signature of the SC gap according to BCS theory are so-called coherence peaks [93]. They describe an increase of the DOS in proximity of $\pm\Delta_{\text{SC}}$. A further experimental evidence of a SC state is the temperature and magnetic field dependence of Δ_{SC} . When field or temperature are close to the critical values, Δ_{SC} decreases with increasing field or temperature due to the reduction of the SC fraction of electrons, and the gap disappears at the respective critical values.

BCS theory gives the ratio between Δ_{SC} at zero temperature and T_c as:

$$\frac{2\Delta_{\text{SC}}}{k_{\text{B}}T_c} = 3.52, \quad (2.10)$$

where k_{B} is the Boltzmann constant. The coefficient 3.52 identifies a conventional SC, which corresponds to classic BCS theory with electron-phonon coupling. The ratio is very different for unconventional SC. Some examples of experimental results are given in table 2.2 [94, 95].

As can be seen in the presented examples SC phenomena are rich and difficult to classify. The first reason to establish a family of unconventional superconductors were discoveries of heavy fermion SC [97] and high-temperature SC [98]. Also even before the high temperature SC were discovered first proposals for another origin

(non-phononic: exciton, magnetic *etc.*) of electron-electron pairing were given [99–101].

2.3.2 Cuprates and iron-based unconventional superconductors

Usually people use the term “conventional SC” as a synonym of “can be described by the BCS theory”, but I found that different people understand these terms slightly differently. I do not want to establish here a new strict classification, but to avoid some misunderstandings I think it is good to shed some light on this point. At first, I want to say that the terms “conventional” and “unconventional” have no direct relationship with the critical temperature, not only because some of the unconventional SCs have low critical temperature [24], but also because some of experiments deal with conventional superconductivity at 203 K [102]. Also, first experiments on unconventional SC were performed before high T_c SC was reported [101].

I point out that the term “BCS theory” is often used for slightly different things. Some people tend to say that all theories related to electron-phonon interaction are covered by BCS theory, including also strong electron-phonon coupling (for example, lead (Pb) is a material with a strong coupling, which is clearly attributed to conventional SCs) [90]. For other people strong coupling cannot be related even to extended BCS theory [103, 104]. Also, one can find that BCS theory is applied to unconventional SC [105]. From this point of view BCS theory does not mean that attractive interaction between electrons is phonon-mediated. The most rigorous classification for conventional and unconventional SCs, which I found in use, is based on the symmetry of the SC gap function [106]. The SC gap function can be understood as the electron binding energy. In the simplest BCS case it is a constant, however in general it is a function of electron momentum. It can have different amplitude and phase in different parts of the Fermi surface, which leads to the different SC gap values in different directions. This can be measured with Josephson junctions experiments and critical current measurements [107, 108]. When we have a simple s-symmetry gap function, this indicates conventional SC. Usually, but not always, this means that we can use BCS theory with phonon-mediated attractive

	T_c , K	Δ_{SC} , meV	$\frac{2\Delta_{SC}}{k_B T_c}$
conventional SC, BCS theory, theoretical ratio is 3.52			
Al [94]	1.18	0.18	3.52
Zn [94]	0.85	0.13	3.55
Tl [94]	2.38	0.37	3.59
conventional SC extension of BCS with strong coupling consideration [90] theoretical ratio is 4-5, depending on the material [96]			
Pb [94]	7.2	0.33	4.29
Hg [94] (α phase)	4.15	0.82	4.6
unconventional SC			
HgBa ₂ CuO ₄ [94]	94	24	5.9
FeSe [95]	8.5	2	5.5

Table 2.2: Examples of different superconducting materials with BCS and non-BCS like ratios $\frac{2\Delta_{SC}}{k_B T_c}$.

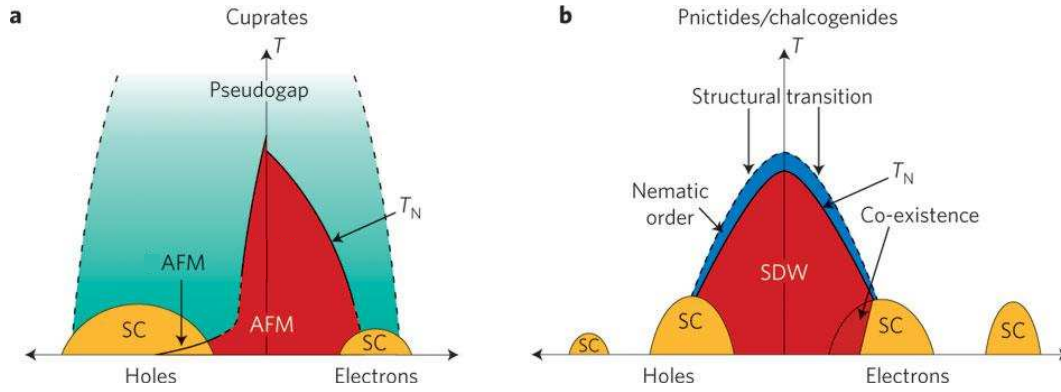


Figure 2.5: Simplified phase diagrams of the cuprates (a) and iron pnictides/chalcogenides (b) superconductors [114]. AFM - antiferromagnetism. SDW - spin density waves.

interactions. In my thesis I use the classification based on the SC gap function symmetry.

In unconventional SC the Coulomb repulsive interaction between electrons dominates. The formation of Cooper pairs is possible only if we have a phase shift in electron wave functions along the Fermi surface, which removes the repulsion between the electrons with a specific momentum. This phase shift is mirrored by the behaviour of the SC gap function and its phase. For example, cuprates have a d-wave pair state. This means that the amplitude and the phase of the SC gap function is different in different directions [109]. The proximity effect and critical currents measurements in different directions clearly show a SC gap amplitude anisotropy [108], and the phase difference can be measured with Josephson junction experiments [107].

However, the nature of superconductivity in cuprates, which were the first discovered unconventional high T_c superconductors, is not clear yet. There are alternative models presented in textbooks [110, 111]. The complexity of the cuprate atomic structure and various possibilities for electron-electron interactions suggest spin waves, interlayer coupling, and other models [110]. The possibility of the phonon nature of the superconductivity is also not fully excluded [112]. So it is possible that with the correct inclusion of the Coulomb interaction and other effects the the lack of isotope effect and the high T_c in cuprates can still be explained by electron-phonon interaction, like it was done for Mo, Os, Ru, and some other materials [90, 112, 113].

Surprisingly the theory of iron-based superconductors (IBSC) has a general consensus on the role of magnetic spin fluctuations as the origin of SC [20, 21]. The IBSCs have attracted a lot of attention since the first experimental report in 2008 [115]. There are similarities and differences from the cuprate SC, and these are pointed out in the following. Both families of unconventional SC are layered structures, in both of them the d-orbitals are playing a significant role in the Cooper pairing and in both the antiferromagnetic state in the phase diagram is close to the SC state, see Fig. 2.5. The main difference between these two types of the SCs is that cuprates are Mott insulators, while the IBSC are metals or semimetals [20, 116].

2.3.3 FeSe

In this work, I studied α -FeSe. FeSe is the simplest iron chalcogenide SC. Bulk FeSe has relatively small $T_c=8.5$ K [24]. Following its discovery a tremendous activity has developed aiming to increase T_c by applying pressure, chemical doping and symmetry reduction [87, 118–120]. Also thin films of FeSe were studied [22, 23, 87, 88]. The most promising results in an attempt to increase T_c were obtained with FeSe thin films on a SrTiO₃ (STO) substrate. STM results suggest $T_c=77$ K and Δ_{SC} of approximately 22 meV [22]. A four probe transport measurement reported $T_c=100$ K [23] for one unit-cell (UC) thick FeSe.

Paramagnons, collective excitations of the electron spin structure, are a plausible mechanism of a pairing in FeSe and other iron SC [121–123]. Recent experimental [124, 125] and theory [126] results on iron pnictides support the idea of a multiband $s\pm$ superconductivity with singlet pairing. The same theoretical result was obtained also for FeSe [127]. Some STM experiments show an absence of so-called in gap states in local DOS of FeSe produced by nonmagnetic impurities [128]. This fact can be naively used to rule out SC gap sign change possibility, which is the feature of $s\pm$ SC [128]. However, attentive theory studies make this idea unfounded [129, 130].

The spin fluctuation mechanism as applied to bulk FeSe can be summarized in the following way. The theory of SC tells that only electrons which have an energy in close proximity to the Fermi level, take part in the Cooper pair formation. The Fermi surface of the IBSC presents an s-shape hole pocket at the Γ -point and an s-shape electron pockets at the M-points [127, 131], see Fig. 2.6. Due to an incipient antiferromagnetic instability the system features strong spin fluctuations

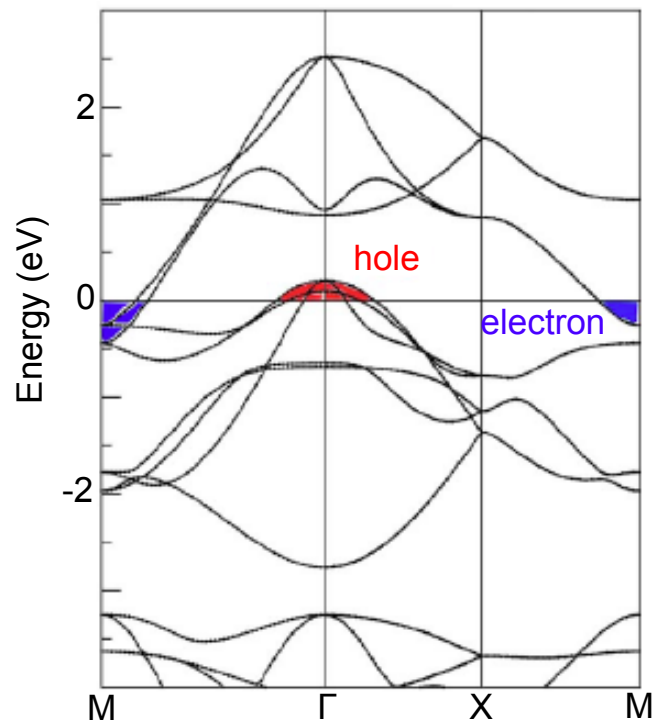


Figure 2.6: The band structure of FeSe presented in reference [117] with denoted electron and hole pockets. (Electron/hole pocket - contour of Fermi energy in the Brillouin zone with the positive/negative electron effective mass.)

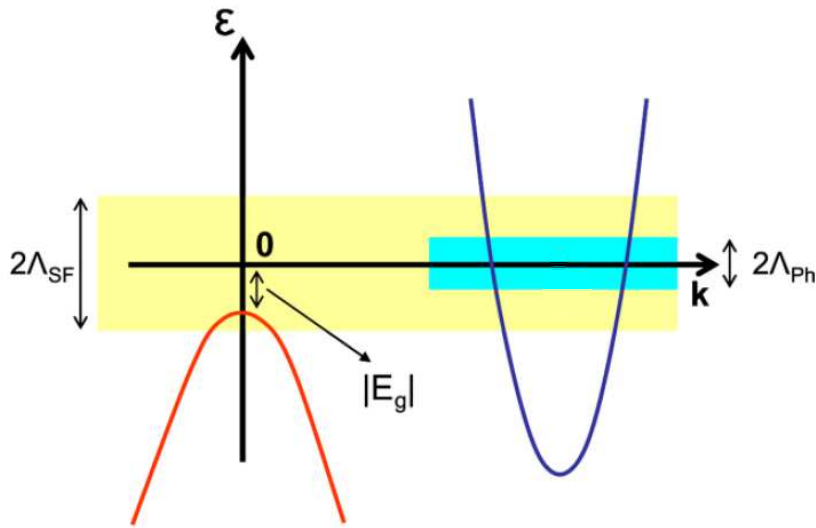


Figure 2.7: Sketch describing a theoretical model from paper [132]. Representative of the incipient band (red) and regular band (blue). SC is driven by phonons in the regular (blue indicates a pairing cutoff energy $2\Lambda_{\text{Ph}}$) band. SC is induced in the incipient band through spin fluctuations (yellow indicates a pairing cutoff energy $2\Lambda_{\text{SF}}$). T_c is inversely proportional to E_g .

with a momentum connecting these two electronic structures. The electrons can be scattered by the spin fluctuations, and so these fluctuations transmit the interaction between electron and hole pockets. In spite of the fact that the interaction is of Coulomb type and therefore repulsive, it can still provide Cooper pair binding if the states in the hole and electron pocket are quantum mechanically out of phase. As was already said this phase shift is mirrored by the behaviour of the SC gap function. So it leads to the different phase of the gap function in the electron and hole pockets. Nevertheless, the SC gap function is isotropic. This statement is difficult to prove experimentally. However, the technique, which is already successfully used for the IBSC, can be also applied to FeSe [124].

Low electron density is a feature of the IBSC. This is puzzling due to a first approach consideration of low T_c in such systems [90]. T_c is low for pristine bulk FeSe, but not for FeSe films and some other materials, which are based on FeSe. SC of FeSe films on STO, for example, is even more puzzling, due to the fact, that there is no hole pocket at the Γ -point in this system [133]. This feature can be tackled by different theoretical approaches [134]. So-called incipient bands are a good candidate for a possible explanation [132]. “Incipient” means that the band is away from the Fermi level, but within a pairing cutoff energy, see Fig. 2.7 (band denoted by red). Based on the discussion by Xiao Chen *et al.* [132] such bands can lead to an increased critical temperature. A simplified description of this proposition can be considered as follows. Electrons interact with each other inside the relatively large electron pockets at the M-points via phonons, and they interact also with electrons from the band which is presented weakly at the Fermi level or even stays beneath it at the Γ -point. The interband interaction is provided by the spin fluctuations. Thus, both phonon and spin interactions contribute to SC here.

This model was also applied to explain increased T_c (in comparison with bulk)

in the FeSe films [132]. In this case, a smaller hole pocket at the Γ -point in the thin films can lead to higher T_c . But the detailed understanding of SC in FeSe is still under debate [122, 135]. The reviews by Igor Mazin [131, 136] present references of the current research and future prospects of IBSC.

Chapter 3

Experimental setup

A successful and reliable study of the structural and electronic properties on the atomic scale of a clean crystal surface requires complex research tools with certain prerequisites. Usual challenges are the contamination of the surface, involved sample preparation, electronic, acoustic noise and changing temperatures from 10 K to 1000 K. In my research I used not only a commercially available UHV cryogenic STM from Omicron, but I also added a specially developed UHV preparation chamber to the STM system. Our Omicron STM, which I will briefly describe in section 3.1, is based on the STM described by Hug *et al.* [137] The sophisticated preparation chamber, which I added to the system, is described in section 3.2.

Figures 3.1(a) and (b) show photographs of the full new UHV STM system. To indicate the added complexity and experimental possibilities, the previous preparation chamber is shown in (c) for comparison, where only a differentially pumped ion gun and some evaporators were present.

The whole system is supported by a four leg air damping system. This system itself sits on a concrete block ($4 \times 4 \times 4 \text{ m}^3$), which is isolated from the laboratory foundation and is based on a sand bed. The STM system is enclosed in a sound proof cabin.

One of the goals which I pursued during my work was setting up and adapting the preparation chamber by adding tools for the *in situ* cleavage of layered substrates. This aspect is described in chapter 4.1 for the preparation of Bi_2Se_3 surfaces from bulk samples.

3.1 Cryogenic Scanning Tunneling Microscope

The scheme in Fig. 3.1(d) indicates the vertical lift which is used to move the STM head, see Fig. 3.2, between the cryostat and the STM chamber. The STM chamber is at room temperature. At this position tip and sample exchange are performed. The pressure inside the STM chamber is less than 10^{-11} mbar, and I estimate it is one order of magnitude lower at the STM cryostat position, due to the cryogenic pumping of the inner wall of the UHV cryostat inset, held at 4 K, by liquid ^4He .

The cryostat is manufactured by the Janis Corporation. It consists of two liquid helium (He) and one liquid nitrogen (N) reservoirs. Inside the cryostat, surrounding the STM head, a superconducting split coil magnet is mounted. It can produce a magnetic field of up to 8 T along the vertical direction. The base temperature of the STM in the cryostat is 10 K. A resistive heater, installed on the STM head, allows to increase the temperature in a controlled manner, the maximum temperature is of

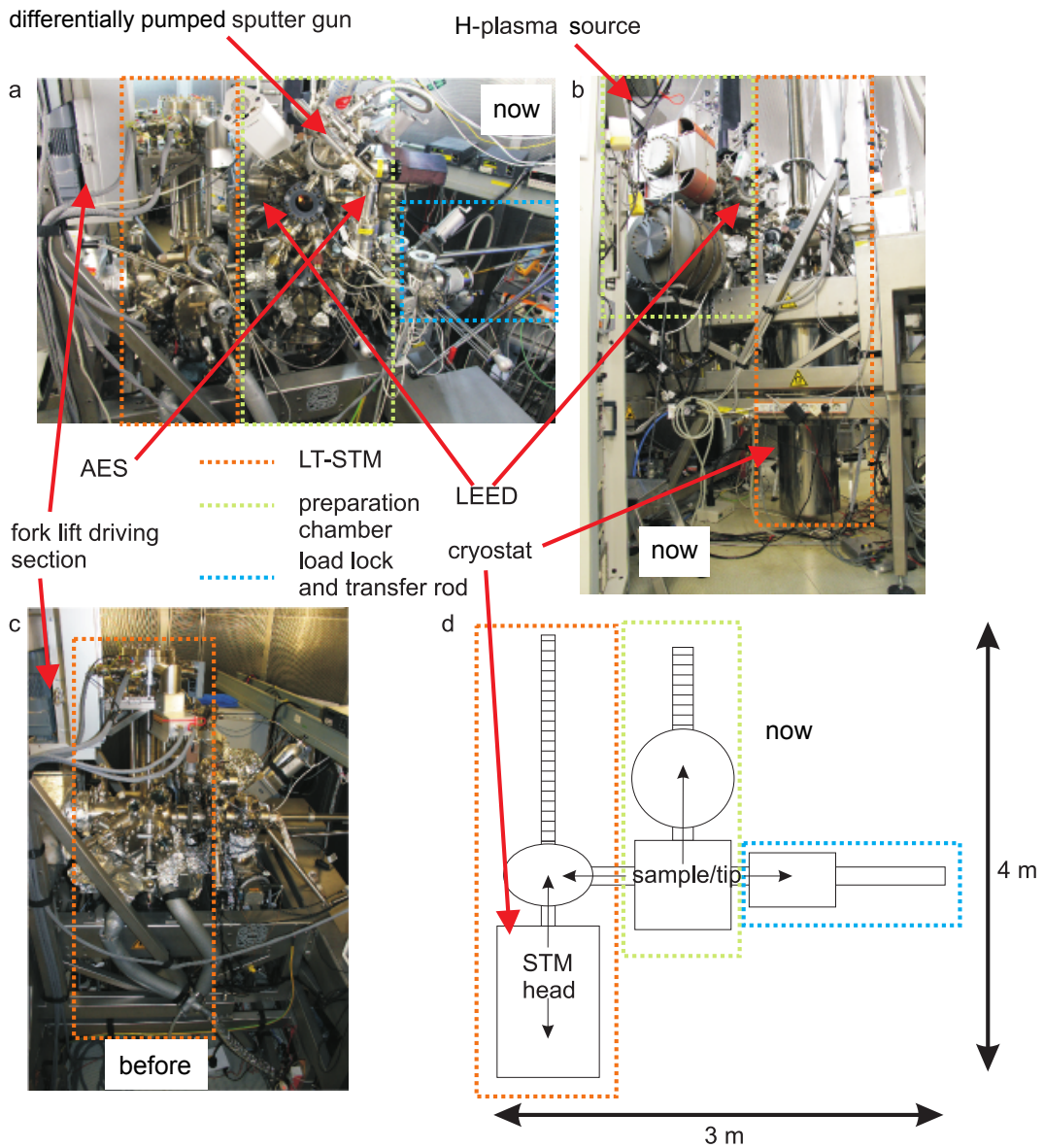


Figure 3.1: The ultra-high vacuum (UHV) chamber, supported by a stainless steel frame, consisting of (separated by gate valves) the low-temperature scanning tunneling microscope chamber, newly added preparation chamber (with additional surface characterization tools) and load lock and transfer rod part. (a) South side view with STM lowered down into the cryostat. (b) North side view. (c) The previous set up of the STM system, without preparation chamber, for comparison. (d) Scheme of the UHV system with denoted transport directions for the sample/tip and the STM head. Larger photographs of the system are provided in the Appendix A.

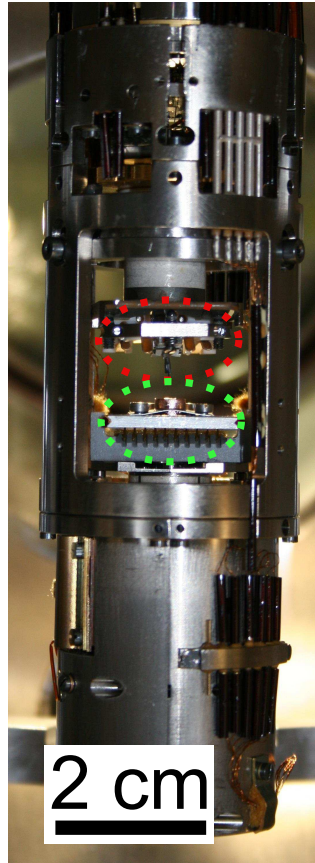


Figure 3.2: Head of the STM with inserted tip holder with the tip, see Fig. 3.3, encircled in red and sample on the sample plate, see Fig. 3.6, encircled in green.

order 30 K. The STM temperature is monitored by CernoxTM sensors, mounted in proximity to the sample position. This sensor allows a wide range of temperature measurements from 100 mK to 420 K [138]. It is read by a Lakeshore temperature controller [139]. This controller is also used to operate the heater on the STM head.

The STM head has also its own noise vibrational isolation system, which consists of a spring suspension and 3 stages eddy current damping. The noise isolation leads to a tip-sample noise level of order ± 200 fm. Thermal drift and piezo creep remain detectable. The drift can be around 1-5 nm per 24 hours at equilibrium temperature. Piezo creep is significant (nonlinear distortions in the 1-2% range) only during large scans (>300 nm), but not critical in small scans (<200 nm). The performance and the low noise in STM measurements was fully retained and is of outstanding quality also after the modification of the system with added components.

Tips are installed to the STM head on a special tip holder, see Fig. 3.3. Before the tip is loaded to the UHV chamber, it is spot welded to a Ta L-piece on the Ti-plate (see Fig. 3.3). This part is attached to the Omicron tip-holder by screws. The tip preparation by *ex situ* electrochemical etching is well explained in various books [41, 61–63] and previous theses [140, 141].

The main parts of the STM electronic scheme are denoted in Fig. 3.4. The piezoelectric scanner is attached to the sample and to the Z-step motor for coarse approach. The X,Y- piezo motors for coarse positioning move the tip laterally. The tip is positioned above the sample by the X,Y - coarse motion. In STM operation,

the sample is scanned via the scanner piezo, while the tip remains stationary. The tunneling voltage is applied to the sample, while the tip is virtually grounded. The tunneling voltage is referred as the sample bias. Further aspects are addressed in several reviews [41, 61–63].

The transimpedance amplifier, due its function for the transformation of a weak tunneling current signal of the order of nanoamperes to a voltage signal must be positioned as close to the tip as possible. This improves the signal-to-noise ratio of the tunneling current I and differential conductance measurements dI/dV . This is why the transimpedance amplifier, unlike all other STM electronics, is connected directly at the UHV chamber feedthrough of the tip contact wire.

The lock-in amplifier is used to obtain the differential conductance signal (dI/dV). An AC signal from it modulates the DC sample bias. I used a frequency of 4–5 kHz for the lock-in AC signal to set it well above the feedback loop reaction time to prevent a modulation of the tip-sample distance.

The amplitude of the lock-in signal is an important parameter for the dI/dV measurements. It needs to be well chosen with respect to the energy range and energy width of expected LDOS features. An high AC amplitude limits the energy resolution. For the lock-in AC signal a V_{rms} (root mean square) was taken in the range 1–10 mV, which corresponds to 3–28 mV peak-to-peak amplitude. The low amplitude has been specially used for the superconducting gap measurements, because the STS features in this case can be as small as few mV [142].

The main advantage of the lock-in measurement in comparison with numerical differentiation of the $I(V)$ signal is the better signal-to-noise ratio. To calibrate the lock-in output and transform it to conductance units we use the $I(V)$ signal, which is always recorded. This procedure implies the search of the linear coefficient and offset for the lock-in STS curve to fit it as best as possible to the calculated $dI/dV(V)$ curve from the $I(V)$ measurements. Thus the units for all the STS curves presented in this work are nS (nanoSiemens).

In Fig. 3.4 the “computer” block comprises two units: a control unit (CU) of the STM and a personal computer (PC) with a special software and connection to the CU. All of the presented studies were done with the MATRIX CU. The MATRIX CU is the conventional CU supplied by Omicron for their recent scanning probe

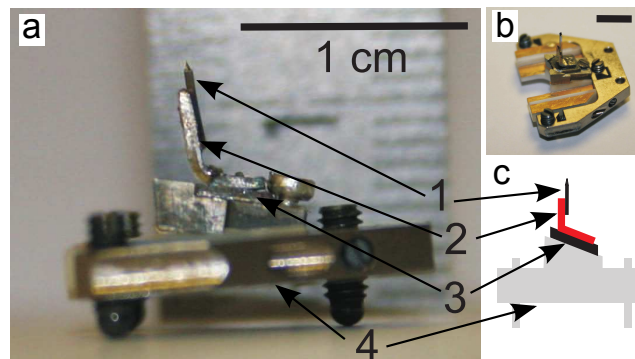


Figure 3.3: (a) Photograph of the tip (1) mounted on the in-house modified (2) Omicron tip holder (4). The tip is spot-welded to a Ta L-piece (2, red (c)), which is spot-welded to the Ti plate (3). (b) Zoom-out photograph of the same construction (black bar: 1 cm). (c) Schematic of the tip holder. This tip holder can be exchanged *in situ* with a wobble stick, with the STM in the upper position.

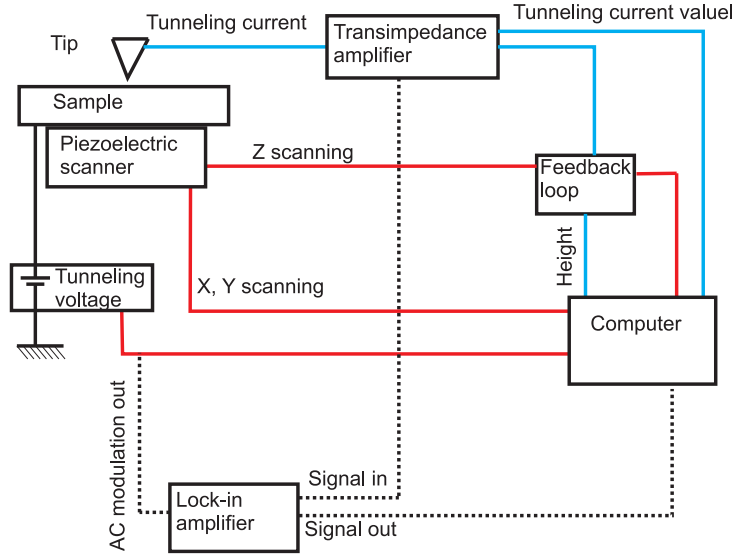


Figure 3.4: Simplified STM scheme. The main control signals coming from the computer are marked by red, the main information channels coming to the computer are marked by blue. In constant current mode, the tip sample voltage is set by the user through the program interface, and the tip-sample distance ($\sim 4\text{-}5 \text{ \AA}$) is kept constant by Z - movement of the piezo scanner, while the in-plane scanning is set by the computer. The Z coordinate is controlled by a feedback loop, with parameters specified by the computer. The signal from it goes to computer as apparent height. We obtain differential conductance (dI/dV) signals by a lock-in technique. In scanning tunneling spectroscopy (STS) mode, scanning is stopped and the feedback circuit is opened, the voltage between sample and tip is varied, and the corresponding tunneling current $I(V)$ and its derivative $dI/dV(V)$ are recorded simultaneously.

microscopy (SPM) systems.

The software version used on the PC was Matrix 3.2. This software has also a built-in script programming language compiler, which is used to add some additional functionality to the software and thus to the STM. The software also has the possibility to work with the LabVIEW platform, but due to the different architecture it leads to a low performance of the PC. It is better to separate possible complex programs on the Matrix and on other parts. In my work, I used the programming possibilities to integrate the control and the parameter tracing of the lock-in, superconducting magnet and the temperature controller to the STM software. I also used the Matrix script language to make automated algorithms for the acquisition of serial images or spectroscopy curves with parameter variation. Some examples of the programs, which I created, are provided in the Appendix B.

An important part of the STM software is the storage and export of the STM scanner calibration data. The calibration parameters for the piezoelectric scanner are verified during STM of known surfaces. A Cu(111) surface, imaged at atomic resolution, was used for the X-, Y-, Z-calibration (mono-atomic steps of Cu(111) terraces) and the *in situ* cleaved $\text{Bi}_2\text{Se}_3(0001)$ surface for crosschecking the X- and Y- calibration.

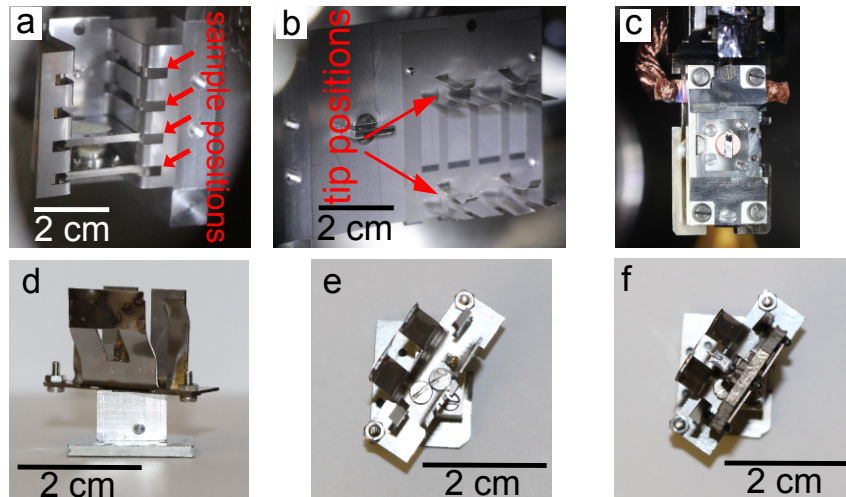


Figure 3.5: Photographs of the garage (a), (b) and the tip holder adapter (d), (e), (f), which I developed for the new preparation chamber, and the sample holder of the vertical transfer rod (c), with inserted sample, see Fig. 3.6. (a) The sample garage (two lower positions are occupied by luminescence screens). (b) The tip garage (two positions for tips). (d), (e) Different views of the tip holder adapter for the vertical transport of tips. (f) Tip holder adapter with a tip inside.

3.2 New preparation chamber

In situ STM experiments are the best solution for studying surfaces on the atomic scale. Thus the preparation chamber is often mandatory for the STM studies. The general parameters of the newly added preparation chamber are described first.

The chamber is separated from the STM and load lock/transfer rod parts by gate valves. The base pressure of the chamber is as low as 3×10^{-11} mbar. This pressure allows to store tips and samples for months without significant loss of surface and apex qualities. I installed a self designed garage with two slots for tips and four for samples in the preparation chamber. Some other additional devices, such as luminescence screens, see Fig. 3.5, can also be stored there, if they are mounted on a sample plate (see Fig. 3.6).

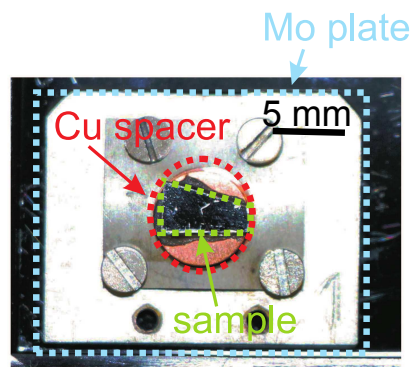


Figure 3.6: Photograph of a typical Bi_2Se_3 sample glued to the Cu spacer by a graphitec adhesive [143]. The Cu spacer is attached to the conventional Omicron Mo sample plate by a Mo foil with four screws.

Tips and samples are loaded to the chamber through a load lock, which is separated from the UHV chamber by a gate valve. It can be pumped down for sample/tip transfer in a few hours. The tip/sample is then transferred to the horizontal transfer rod. This rod is also separated from the preparation chamber while it is fully retracted in its tube. The transfer rod part of the chamber has a base pressure of 1×10^{-9} mbar. It remains the same during the transfer from the load lock. With turbo pumps on, the lowest pressure of this part of the chamber is 2×10^{-10} mbar.

The tip preparation is performed in the preparation chamber. The goal of this step is to remove adsorbates and oxides from the tip apex, thereby increasing its stability of the tunneling process. For this the tip is moved to the proximity of the cold circular filament and a high voltage (1.3 kV) is applied between filament and tip. Then the filament is heated until the tip current reaches 50–60 mA, and then the filament current is immediately switched off. This procedure excludes excessive heating of the tip holder, while the tip temperature reaches 2000° C for 1–2 seconds. The temperature is checked by a W-hairpin pyrometer (Keller Mikro-Pyrometer PV11).

The preparation chamber itself is separated into two parts by a horizontal gate valve. The lower chamber (see Fig. 3.1(d)) has a cylindrical shape. It is mainly used for the storage of samples and for tips and tip/sample transport. There is also Ti sublimation pump and a LN_2 cryo pump, which are used additionally to the turbo and ion pumps, when needed. There are also three electromagnet coils for a magneto-optic Kerr effect (MOKE) experiments. The MOKE was not used for the research presented in this work. The sample temperature during MOKE studies is variable in the range from 160–750 K.

All of the preparation and surface science related studies except tip flashing and STM studies are realized on the end of the vertical transfer rod of the preparation chamber. There is the sample holder, which has an additional adapter for the tip holders, see Fig. 3.5. So the tip and the sample both can be easily transported to the top part of the preparation chamber. The transfer rod has a small inner reservoir for liquid nitrogen. A filament is available for HV assisted sample heating. During all steps of the tip/sample preparation the temperature can be varied in the range specified above. The heating can also be used for sample annealing. The temperature of the sample is controlled by a type-K thermocouple and independently checked by the infra-red thermometer (IMPAC 140 [144]). Higher sample temperatures up to 2300 K are reachable on the heating stage of the horizontal transfer rod.

The gate valve between top and bottom parts of the preparation chamber is essential as the top part contains also the differentially pumped ion gun and the plasma source (see Fig. 3.1(a), (b)). Their use is linked with a gas flow into the chamber. The differentially pumped ion gun is used for argon sputtering with the Ar pressure inside the chamber reaching 1×10^{-8} mbar. However, the plasma source is used for atomic hydrogen treatment of the surface. The H_2 pressure during this process is around 2×10^{-5} mbar. Such a high pressure is required because the amount of the atomic hydrogen with respect to the number of an H_2 molecules is approximately only 1%, see chapter 6.1. The exposure time of the H-plasma treatment of the sample is around 1–5 seconds. During this time not only the gate valve of the ion pump of the preparation chamber, but also the gate valve between the top and bottom parts of the chamber are closed. It takes around 1 hour to evacuate the hydrogen from the chamber to reach low 10^{-10} mbar pressure after H-plasma usage. We use a plasma cracker source with the assistance of the electron

cyclotron resonance effect. This plasma source is produced by SPECS GmbH. It uses a microwave energy with a frequency of 2.45 GHz, produced by the magnetron source. The H-treatment of the sample is mainly controlled by the hydrogen pressure and the magnetron current. The atomic H etches away mainly Se, and it is used to prepare Bi bilayer (BL) on the Bi_2Se_3 surface [31].

The newly added preparation chamber is also used for material deposition. There are four metal evaporators connected to the chamber to deposit magnetic materials (Cr, Co, Fe). A magnetic tip can be prepared and used to perform spin-STM studies [145–147]. However this potential is not presented in my work. For the sample preparation I used a 99.995% purity iron rod to evaporate Fe onto the substrate.

Since the LT-STM experiments can only be started after a long cool down time of order 12 h, it is very useful to have other surface characterization technique available. Inside the top part of the preparation chamber there are also low-energy electron diffraction (LEED) and Auger electron spectroscopy (AES) setups. The description of theory and experiment basics of this techniques can be founded in many reviews (in particular in references [148, 149] for AES and [150, 151] for LEED).

The Omicron rear view LEED optics (available under the name SPECTALEED) was used in this work. The reciprocal surface lattice of the studied surfaces can be studied. The absolute values of the lattice constants were obtained by STM, in quantitative agreement with the LEED analysis.

A cylindrical mirror analyzer (CMA) with integral electron beam gun from Varian was used for Auger spectroscopy. The electron beam energy was 3 keV with the anode current of 150 μA and the sample current of approximately 150 nA. The differentiated AES spectra were obtained with a lock-in technique with a frequency of 17 kHz and the peak-to-peak voltage of 0.5 V. The CMA energy range was usually 0-1000 eV with a 5 minutes scanning time. The AES was used for checking the chemical composition of the sample surface.

The detailed sample preparation which includes the $\text{Bi}_2\text{Se}_3(0001)$ surface preparation, the FeSe nanocrystals and Bi BL preparation are discussed in the corresponding chapters 4.1, 4.2, 5.1, 6.1.

Chapter 4

Preparation and characterization of $\text{Bi}_2\text{Se}_3(0001)$

I present an alternative preparation method, as compared to the widely used cleavage, for obtaining atomically clean and well characterized $\text{Bi}_2\text{Se}_3(0001)$. This method is based on ion bombardment with subsequent annealing. It was proposed due to different drawbacks of the cleavage, which has been in use as a standard preparation technique for van-der-Waals bonded, layered materials [16–18]. For instance, it is impossible to use cleavage for thin crystals and films. Moreover, we can also reduce the amount of wasted material and preparation time using this method. Here, I characterize this method and compare it with conventional cleavage.

The surface of a cleaved Bi_2Se_3 crystal has been studied intensively [16–18]. However, there are not so many STS results on this subject [153]. There are still some questions about the surface states representation in dI/dV curves and STS maps. Thus $\text{Bi}_2\text{Se}_3(0001)$ serves as a reference for further studies.

Starting point of our studies are $\text{Bi}_2\text{Se}_3(0001)$ single crystals, which were grown by the Bridgman method [154]. The Bi_2Se_3 crystal has a closed-packed structure shown in Fig. 4.1 with different spacings between atomic layers along the z-direction.

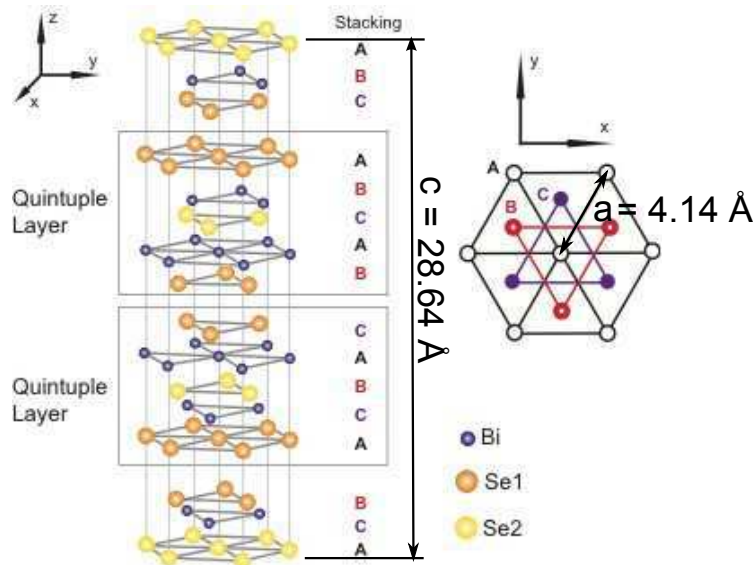


Figure 4.1: The rhombohedral unit cell of Bi_2Se_3 with denoted quintuple layers (QL). The crystal has a layered structure, where adjacent QL are bonded to each other by van-der-Waals force. The direction of the z-axis is (0001) [152].

The lattice constants of bulk Bi_2Se_3 are in the basal plane $a = 4.14 \text{ \AA}$ and along the c -axis $c = 28.64 \text{ \AA}$. Bi_2Se_3 is a layered material and is built up along the (0001) direction by so-called quintuple layers (QL). The layer sequence within the QL is Se-Bi-Se-Bi-Se (see Fig. 4.1) [152]. The QLs are bonded by van-der-Waals forces.

We use samples with a lateral size of around $7 \times 7 \text{ mm}^2$ and an approximate thickness of 0.5 mm, which we cleave *in vacuo* or, alternatively, prepare by ion bombardment and annealing. The Bi_2Se_3 sample is glued on a copper spacer, which is fixed to the STM sample plate by screws, see Fig. 3.6. The adhesive Resbond 931 C from Polytec PT [143] was used for the gluing.

Cleavage of layered substrate materials, such as Bi_2Se_3 , is an established preparation technique [16–18]. The suitability of Bi_2Se_3 for cleaving is due to its layered atomic structure. Cleaving occurs between van-der-Waals (vdW) bonded QL [155]. However, this technique sometimes leads to the destruction of the sample.

Ion bombardment with subsequent annealing is an alternative preparation method, which does not suffer from this drawback of uncontrolled cleavage. It was used as the main surface preparation method in this work. This procedure leads to surfaces which compared favorably to samples cleaved *in vacuo* both in view of the morphology and of the low density of impurities at the surface.

Nevertheless, *ex situ* and *in situ* cleavage was used for the preparation of reference surfaces and also as additional method for re-preparing contaminated, visually rough or overheated samples.

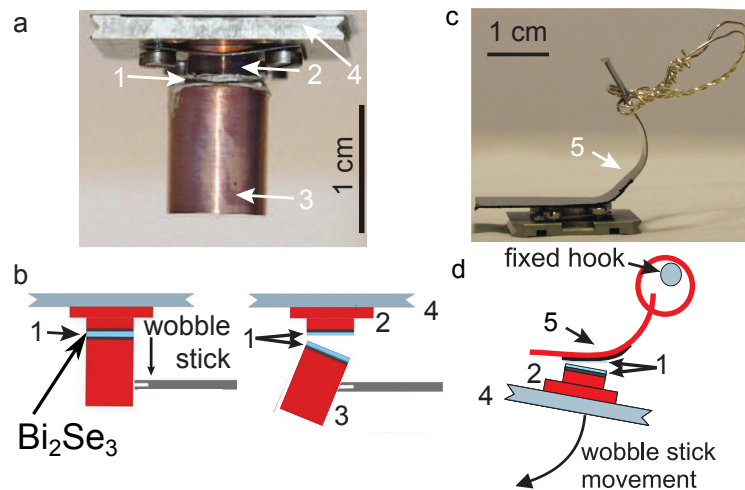


Figure 4.2: *In situ* cleavage of a sample glued between two Cu parts (a), and by using an adhesive tape (c). (a) Photograph of the mounted sample prepared for the cleaving procedure in the preparation chamber: a Bi_2Se_3 crystal (1) is glued between a Cu spacer (2) and a Cu cylinder (3). These parts are supported by a Mo STM sample plate (4). (b) The schematic shows the *in vacuo* sample cleaving by pressing a wobble stick against the Cu cylinder. (c) Photograph of the mounted sample prepared for the load-lock cleaving procedure, with the help of an adhesive tape: steel plate with wire loop (5) is attached to the top of the sample by the double side carbon adhesive tape instead of the Cu cylinder (3). (d) The schematic shows the sample cleavage by moving the setup with a wobble stick, while a wire loop is held by a hook which was preinstalled in the load lock. This method is also referred to as “exfoliation” [156].

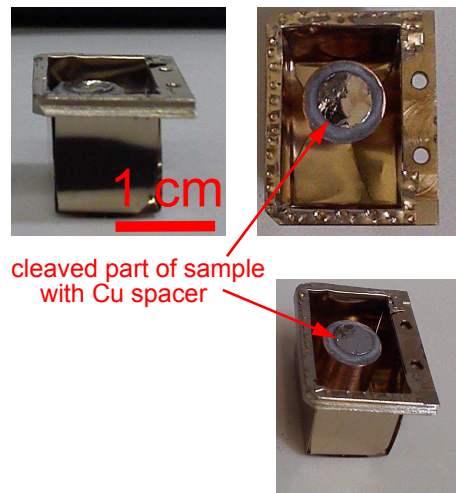


Figure 4.3: Special basket for the *in situ* cleavage after the cleavage procedure with the Cu cylinder and the cleaved-off part of the crystal.

4.1 *In situ* and *ex situ* cleavage

Ex situ cleavage is performed after crystal growth. All crystals which were received were *ex situ* cleaved at first by the supplier [155]. We also used this method if the surface of the crystal from the beginning or after some experiments has too many defects or low optical reflectivity. A double side carbon adhesive tape was used for this [157]. However, this technique was replaced by the *in situ* cleavage procedure, which gave a superior surface quality.

Figure 4.2 illustrates the two cleavage procedure techniques: I describe first the technique shown in (a), (b) and then the method shown in (c), (d).

A copper cylinder is glued to the surface of a Bi_2Se_3 crystal which itself is glued to a Mo sample holder, using the conductive adhesive Resbond 931 C from Polytec PT [143]. Before cleaving, the sample with the copper cylinder is transported to the preparation chamber and rotated to face downwards. A wobble stick is used inside the ultra-high vacuum (UHV) chamber to gently press against the Cu cylinder, while the sample holder is kept in a fixed position in the sample garage. The resulting torque leads to a smooth cleavage of the Bi_2Se_3 crystal, and the Cu cylinder automatically drops down, away from the freshly cleaved surface. This configuration allows reliable *in vacuo* cleavage.

Despite a low base pressure of the preparation chamber of 3×10^{-11} mbar, even after 24 hours inside of the chamber, the sample with glued cylinder leads to a pressure of 3×10^{-10} mbar. We ascribe this to the degassing of the glue. And during the cleavage itself the pressure rises to $5 - 8 \times 10^{-10}$ mbar for a minute. The gluing of the cylinder requires high accuracy to avoid a spillover of the glue over the sides of the sample. We remove the cylinder with its glue out of the preparation chamber with the wobble stick and the transfer rod with a specific basket, shown in Fig. 4.3. This removable basket is mounted below the sample plate, at the sample garage, during the cleavage.

A simpler *in situ* cleavage procedure was also developed. The geometry of the new setup is presented in Fig. 4.2(c) and (d). This new approach exploits the

cleavage inside of the load lock. The load lock during the cleavage is pumped out and the gate valve between the UHV chamber and the lock is opened. The pressure after the opening is stabilized at 1×10^{-9} mbar and stays the same during the cleavage.

During the cleavage the sample is held by the wobble stick. Then it is gently moved in such a way that the metal loop is caught by the rigid hook inside the load lock. After this the sample is carefully moved further in the load lock, while the metal plate with the top part of the sample stays on the hook, and a fresh surface is thus prepared by this exfoliation. After this, the sample is immediately moved to the UHV chamber, and the rest of the setup can be easily moved out when the load lock is vented.

The steel plate attachment by the adhesive tape is much more reliable than the Cu cylinder gluing. And the cleavage procedure is much faster. Also, if the sample itself has been already in use in UHV this new technique does not lead to a substantial pressure increase in the preparation chamber. To enhance the adhesion between tape and crystal it is advisable to press both together by 50 g weight in air for a few hours before transfer into the load lock. The best results were achieved with at least 5 hours pressing and 24 hours load lock pumping on the sample with the attached metal plate.

4.2 Sample preparation by sputtering-annealing cycles

We studied Bi_2Se_3 samples cleaved *in air* and *in vacuo*, which subsequently have been exposed to Ar-ion bombardment (energy: 1–2 keV, sample current density: $j \approx 0.1 \mu\text{A}/\text{mm}^2$, for 15 min) and annealing cycles (temperature: 670–690 K, time 1 hour). The best results in the surface preparation were obtained with 2–3 cycles of ion bombardment and annealing.

The annealing procedure was done by slowly heating the sample by a 22 W filament heater. The maximum temperature (670–690 K) is reached after 30 minutes, and it is maintained for half an hour.

The annealing time and temperature are critical parameters, and this aspect is elucidated further in the discussion. However, briefly I can say that an increase of the sample annealing temperature by 50 K destroys the surface by thermal decomposition, and the surface reflectivity is lost, see Fig. 4.4. A lower annealing

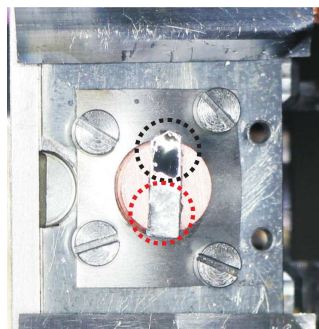


Figure 4.4: Photograph of the sample after annealing (720 K). A large part of the surface (encircled in red) changes its reflectivity, while only less than one third of the sample surface maintains in a mirror like surface finish (encircled in black).

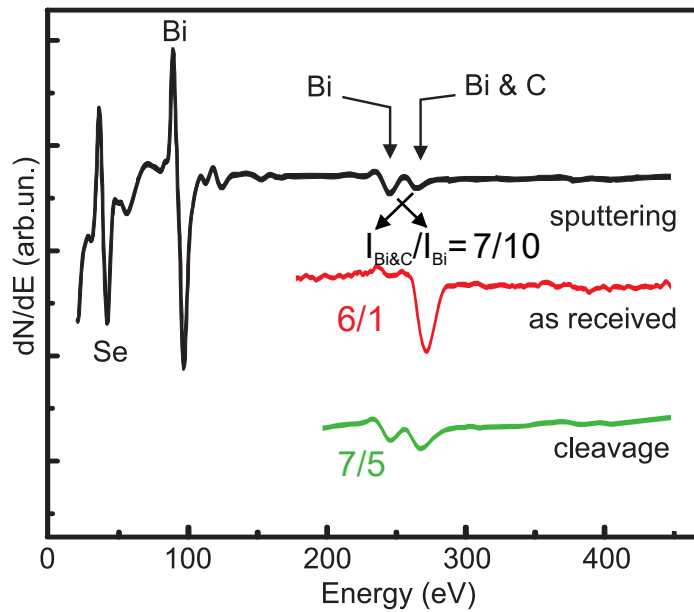


Figure 4.5: Differentiated Auger electron spectra for differently prepared samples. Top curve: cleaning by sputtering. Center curve: as received. Bottom curve: cleaved. Primary electron energy: 3 keV. The ratios indicate the peak height ratio of the adjacent features of Bi and Bi&C.

temperature of 620 K leads to an inhomogeneous surface morphology, where surface damage by ion bombardment remains visible.

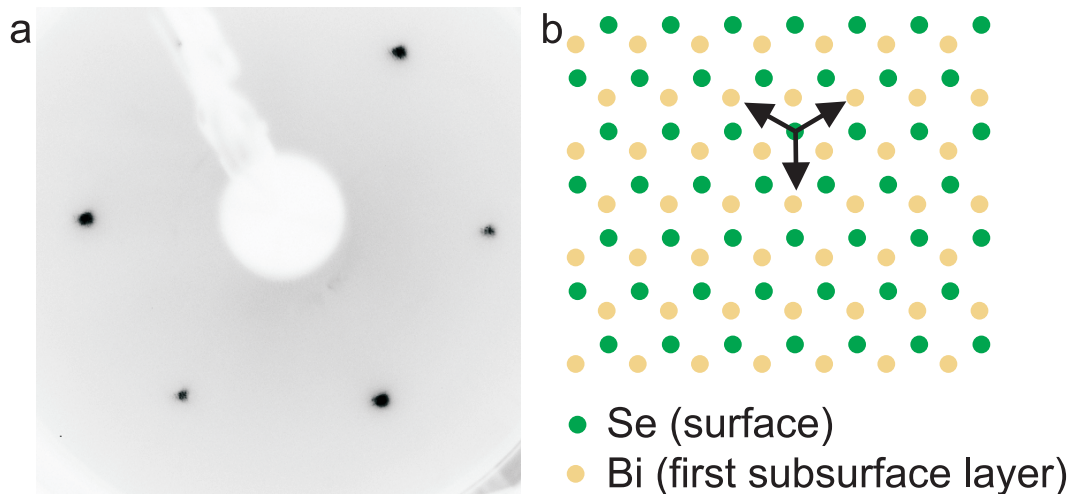


Figure 4.6: (a) LEED pattern of Bi_2Se_3 at an electron energy of 38 eV. (b) Hard sphere model of the $\text{Bi}_2\text{Se}_3(0001)$ surface (green) and the subsurface (orange) atomic layer. The hexagonal arrangement of Se surface atoms has sixfold symmetry, which leads to six diffraction spots on the LEED pattern. The crystal itself has a threefold symmetry due to its stacking along the c -axis. This is visible on the image by the different intensities of the LEED spots.

4.3 Surface characterization by low-energy electron diffraction (LEED) and Auger electron spectroscopy (AES)

AES spectra of the Bi_2Se_3 surface were used as a first criterion to judge the surface cleanliness. The most common contamination of Bi_2Se_3 is carbon [158]. The carbon AES peak C-KLL energy position is 272 eV, which is close to the Bi-NNO peak at 268 eV. As can be seen in Fig. 4.5, these two peaks are hardly resolved in the AES spectra. For the cleanliness criterion the ratio between the peak height at 268–272 eV and the Bi peak height at 248 eV is taken. A ratio of 7/10 indicates a clean Bi_2Se_3 surface [158].

The neighboring C and Bi AES peaks near 270 eV are most pronounced for the as received sample. After *in vacuo* cleavage the peak intensity is reduced. The lowest ratio between the combined C and Bi peak and the Bi peak is obtained by sputtering and annealing cycles. This ratio is 7/10, which characterizes a clean sample in AES [158]. Unfortunately, the resulting peak shift from 272 to 268 eV with decreasing C is not very pronounced, and it is not exploited further.

The surface contamination, which is present after the cleavage, is ascribed to bulk contaminations. In addition, the carbon-based adhesive may contribute. Both preparation schemes, cleavage and ion bombardment with annealing, result in surfaces with comparably good quality, as checked by STM.

The LEED pattern identifies a well ordered surface, as is shown in Fig. 4.6. The hexagonal arrangement of six diffraction spots reflect the expected symmetry of the surface unit cell of $\text{Bi}_2\text{Se}_3(0001)$. The intensity shows a three-fold symmetry, which is caused by the bulk structure of the Bi_2Se_3 crystal.

We observe broad LEED spots for samples which were prepared by ion bombardment and annealing at a low temperature of $T_{\text{ann}} < 623$ K, indicative of a reduced crystallographic long-range order. Under these conditions, an unexpected long-range quasi-hexagonal superstructure appears, as detected by STM. A more detailed discussion of this phenomenon will be given in chapter 7.1.

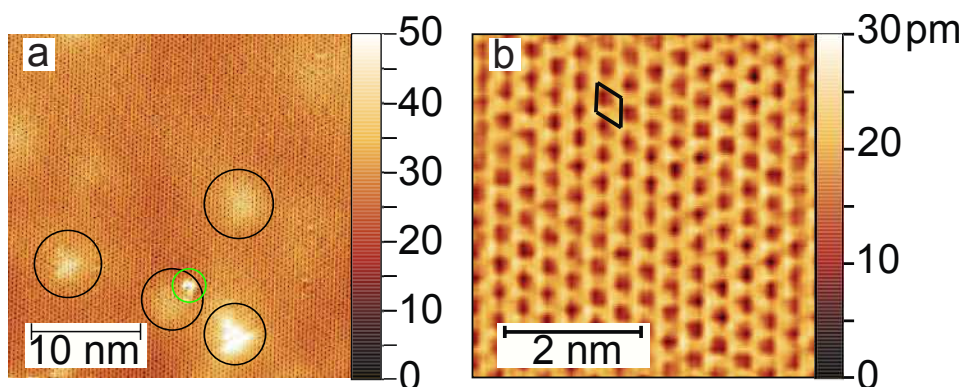


Figure 4.7: STM image of *in vacuo* cleaved Bi_2Se_3 . Some protrusions appear which are 15 or 30 pm high (encircled in black), see [17]. A surface contamination (encircled in green) is visible (a). Atomically resolved surface structure of $\text{Bi}_2\text{Se}_3(0001)$, (b), in a zoom-in of the top part of (a), black lines indicate the surface unit cell. Tunneling parameters: $U = -0.1$ V, $I_T = 1$ nA, $T = 10$ K.

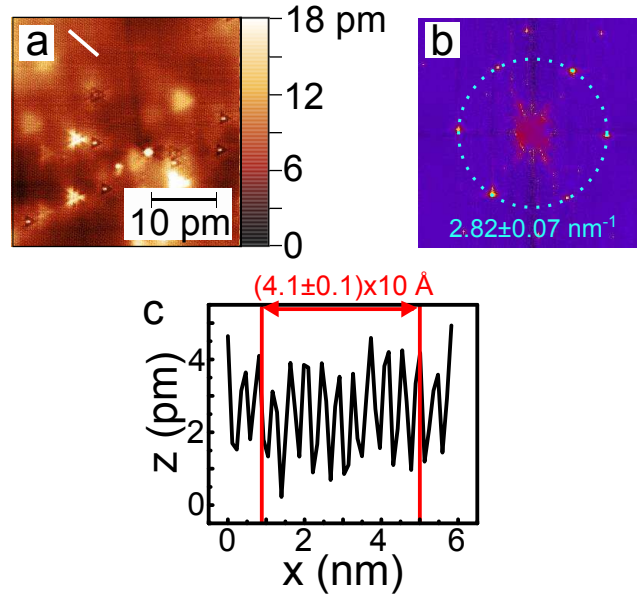


Figure 4.8: One of the STM images taken for calibration verification (a). Fast Fourier transform image of the STM image (b). The Fourier transform shows spots corresponding to a distance between atomic rows. This distance is $\frac{\sqrt{3}}{2}a$, where a is the lattice constant. A circle with a radius corresponding to $3.54 \pm 0.09 \text{ \AA}$ is denoted. This corresponds to $a = 4.1 \pm 0.1 \text{ \AA}$. An apparent height profile along the white line in the image (a) reveals the atomic corrugation. The error bar for the distance along x is 2 %.

4.4 Scanning tunneling microscopy and spectroscopy of Bi_2Se_3

Atomically flat terraces are obtained after cleaving. They are separated by steps with a height of a quintuple layer (QL: 9.5 \AA). We present in Fig. 4.7(a) a constant-current STM image of an as-cleaved $\text{Bi}_2\text{Se}_3(0001)$ surface, which has not been ion-bombarded. STM suggests surface contamination of the order of 0.1 %. The image reveals an atomically flat and clean surface with few protrusions (apparent height $\leq 20 \text{ pm}$). They are ascribed to subsurface defects [16, 159]. Figure 4.7(b) shows a zoom-in, which reveals the atomic corrugation. The hexagonal surface unit cell with base vectors $a = 4.14 \text{ \AA}$ is indicated. This unit cell was used to cross-check the in-plane STM scanner calibration. Atomically resolved STM constant current images with a $30 \times 30 \text{ nm}$ size were obtained for this purpose on two different cleaved samples in different surface areas. Then line profiles and Fourier transforms of these images were analyzed. The average misfit between the well-known hexagonal Bi_2Se_3 surface lattice [152] with 4.14 \AA atomic distances and the STM results was taken for the calibration of the scanner. After the corresponding calibration matrix was included in the STM program, atomically resolved STM constant current images were taken for the verification of the calibration process, see Fig. 4.8.

We found that annealing of ion bombarded samples to $T_{\text{ann}} = 670\text{--}690 \text{ K}$ gives good results, and a typical resulting STM image is presented in Fig. 4.9. Figure 4.9(a) shows a large scale image of terraces, separated by a QL step (0.95 nm), as revealed in the line scan of (b). A zoom-in (c) shows a terrace with some protrusions with an apparent height of 70 pm . We ascribe the protrusions tentatively to adatoms, possibly due to surface contaminations. Their density corresponds to a surface coverage of 0.5 %. We cannot confirm the presence of carbon by AES, as the

surface coverage is too low. We speculate that the protrusions could be due to Bi, Se or C, which are common sources of contamination for this system [19]. Further studies are called for to clearly identify the atomic nature of these protrusions.

The zoom-in in Fig. 4.9(d) reveals the atomic corrugation indicative of clean $\text{Bi}_2\text{Se}_3(0001)$, as shown above for the *in vacuo* cleaved-only preparation in Fig. 4.7(b). On the atomic level, the structural uniformity is interrupted by subsurface defects, comparable to those found for the cleaved Bi_2Se_3 sample, shown in Fig. 4.7(a). These defects have been reported before, and they are ascribed to point defects below the topmost surface [16, 159].

Figure 4.10 shows the differential conductance dI/dV measured by STS on the sample shown in Fig. 4.9(b), away from the protrusions. We find that the dI/dV signal increases sharply below -0.3 V and above 0 V sample bias. Between these voltages the signal is fairly constant. Also, a shallow dip in STS near -300 meV is observed, which is a signature of the Dirac point, as previously reported [16].

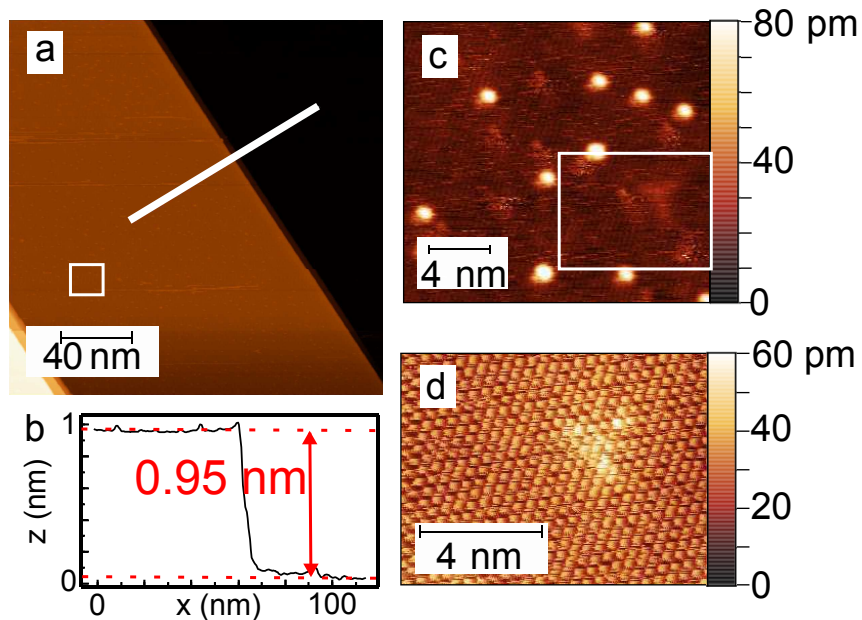


Figure 4.9: STM images of a sputtered and annealed ($T_{\text{ann}} = 670\text{--}690\text{ K}$) sample. (a) Large scale STM constant current image. $U = +0.7\text{ V}$, $I_{\text{T}} = 0.5\text{ nA}$. An apparent height profile along the white line is shown in (b). It reveals a step height of 0.95 nm . (c) Zoom-in of the area in white square in (a) shows some protrusions with an apparent height of 70 pm ascribed to adatoms. $U = +0.4\text{ V}$, $I_{\text{T}} = 0.2\text{ nA}$. (d) Zoom-in of the area in white square in (c) reveals the atomic corrugation. $U = -0.4\text{ V}$, $I_{\text{T}} = 0.15\text{ nA}$, $T = 10\text{ K}$.

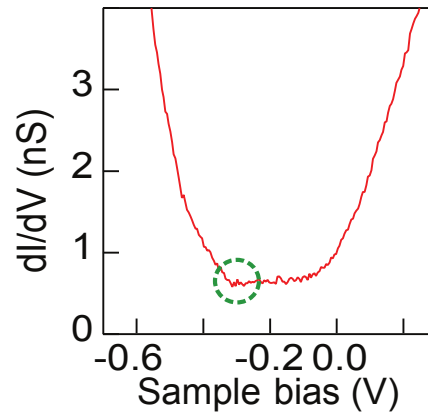


Figure 4.10: STS of Bi_2Se_3 with a shallow dip near -0.3 V (marked by the green circle), which can be interpreted as an indication of the Dirac point. Stabilization parameters: $U_{stab} = -0.4$ V, $I_{stab} = 0.15$ nA, $T = 10$ K.

Chapter 5

FeSe on $\text{Bi}_2\text{Se}_3(0001)$

Studies of unconventional SCs, such as FeSe, are a matter of great interest due to the possible impact on the SC theory and theoretical predictions about high T_c SC [131, 136]. FeSe, in particular, attracted a lot of attention after FeSe films on STO were studied [22, 23]. In these films the critical temperature was found to be more than ten times higher (100 K) [23] than in bulk FeSe (8 K) [24]. However, the physical origin of this surprisingly high T_c is still under debate.

In our work we studied a possibility to use the Bi_2Se_3 substrate for FeSe growth for two reasons. Firstly, FeSe can be produced by iron deposition with subsequent annealing, where no additional Se source is needed. Secondly, the composition of the 3D TI and SC can lead to the formation of so-called Majorana bound states [12, 13, 165], which are proposed ingredients for quantum computation [25].

The structure of FeSe nanocrystals, studied in this work, is not very different from bulk FeSe. In both cases the structure consists of triple layers (see Fig. 5.1) bonded by van-der-Waals forces. The TL has a Se-Fe-Se stacking. It has the structure of a rectangular prism. The thickness of a single TL (the distance between top and bottom Se layers) is around 3 Å [163]. However, the lattice constant of bulk FeSe in the z-direction (see Fig. 5.1) is 5.52 Å [163]. This larger lattice constant along the z-direction is ascribed to a weak van-der-Waals bonding with a large bond length between adjacent TLs. Bulk FeSe at 300 K has a tetragonal structure.

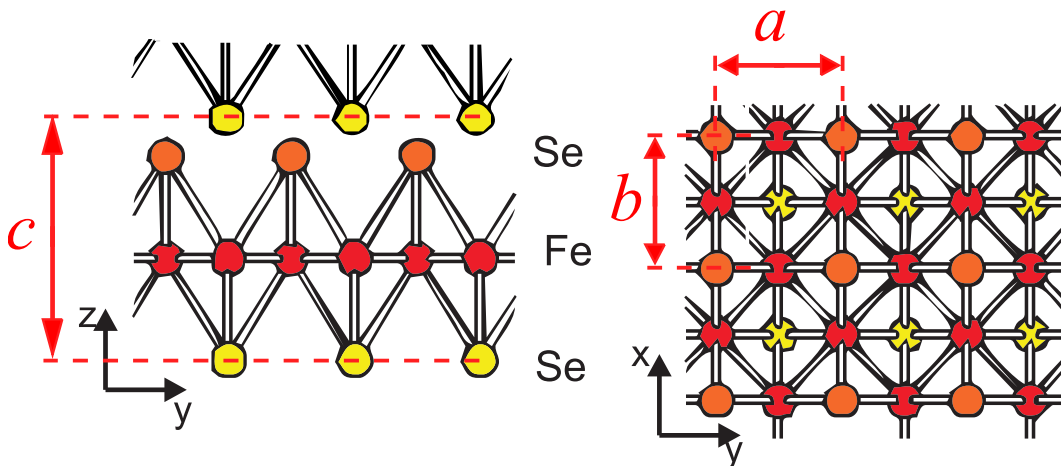


Figure 5.1: Hard sphere model of one α -FeSe triple layer (TL). In a bulk FeSe crystal TL are stacked along the z-direction and bonded by van-der-Waals forces. The bulk crystal has a tetragonal structure ($a = b = 3.77$ Å, $c = 5.52$ Å), which can be changed to a reduced symmetry of a orthorhombic system by applying pressure [160, 161], low-temperature [162, 163], or by epitaxial constraints [164].

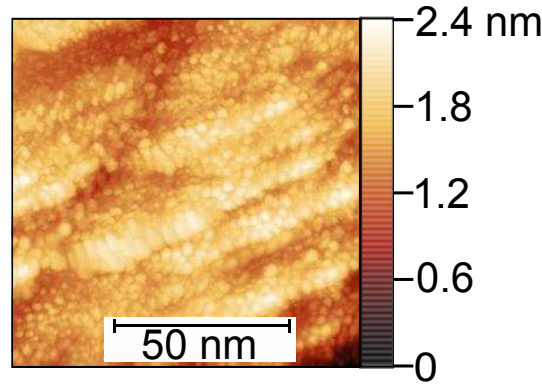


Figure 5.2: STM image of the Bi₂Se₃ surface covered by Fe clusters, after room temperature Fe deposition. The Fe clusters appear as rounded protrusions with an average size of 4 nm and of an apparent height of 0.1 nm. $U = 0.7$ V, $I_T = 0.1$ nA, $T = 10$ K.

However, upon cooling to 70 K a phase transition occurs, the crystal structure changes to orthorhombic. The lattice constants a and b , see Fig. 5.1, which are given by the distances between Se or Fe atoms in one layer, changes from 3.77 Å to two different values in x- and y-directions with $a \approx 3.75$ Å and $b \approx 3.77$ Å (depending on temperature) [163].

5.1 Preparation of FeSe nanocrystals on Bi₂Se₃(0001)

Fe was deposited onto the Bi₂Se₃ surface at room temperature by thermal evaporation from a 99.995 % purity Fe rod with a rate of approximately 0.5 ML (ML: monolayer) per minute, as checked by surface coverage studies on a single crystal metal substrate, Cu(111), by STM. We define 1 ML as a single layer Fe with a surface atomic density of the Bi₂Se₃(0001) surface. The surface unit cell of Bi₂Se₃ has a size of $4.14^2 \text{Å}^2 \sin(120^\circ)$, corresponding to an atomic density of 1 ML: $6.74 \times 10^{14} \text{cm}^{-2}$.

We produce FeSe nanocrystals by post-deposition annealing of the Fe covered surface at 620 K for 50 minutes. After deposition iron forms structureless clusters, as revealed by STM (see Fig. 5.2). Upon annealing Fe starts to form FeSe nanocrystals, which transform into islands, which can be identified by LEED and STM. It is speculated that Se is supplied by the Bi₂Se₃ substrate to form FeSe upon annealing [166].

5.2 LEED and AES characterization

AES was used during the FeSe preparation. It was crucial for the tuning of the deposition parameters and even more so for tuning the annealing procedure. The presence of iron on the sample surface is indicated by three pronounced peaks in AES spectra at 600, 654, and 705 eV, see Fig. 5.3. I observed that the Fe intensity in AES decays rapidly, if the annealing temperature is of the order or higher than 670 K. Diffusion of Fe into the Bi₂Se₃ bulk is a plausible explanation for the loss of Fe.

The inspection of the LEED pattern provides quantitative information on the metric of the adlayer after annealing relative to that of the substrate. Figure 5.4(a)

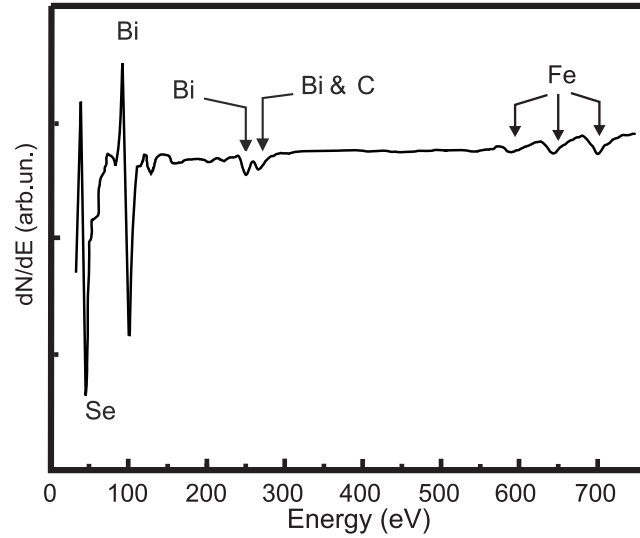


Figure 5.3: Differentiated Auger electron spectrum of Bi_2Se_3 after 1 ML Fe deposition at 300 K with denoted characteristic peaks of Bi, C, Fe. Primary electron energy: 3 keV.

shows the LEED pattern of the pristine $\text{Bi}_2\text{Se}_3(0001)$ surface. A trigonal arrangement of diffraction spots reflects the $p3m1$ plane group symmetry of the $\text{Bi}_2\text{Se}_3(0001)$ surface. Figure 5.4(b) reveals that deposition of 0.7 ML Fe and subsequent annealing leads to the appearance of additional diffraction spots, which we ascribe to the formation of FeSe in three rotational domains. The unit cells of the respective domains are indicated by different colors in Fig. 5.4(b). From the first order LEED spots it is clear that the FeSe in-plane structure has different lattice constants a and b , which means that the structure of the FeSe nanocrystals is orthorhombic even at room temperature. A more detailed analysis of the FeSe structure is given in the discussion.

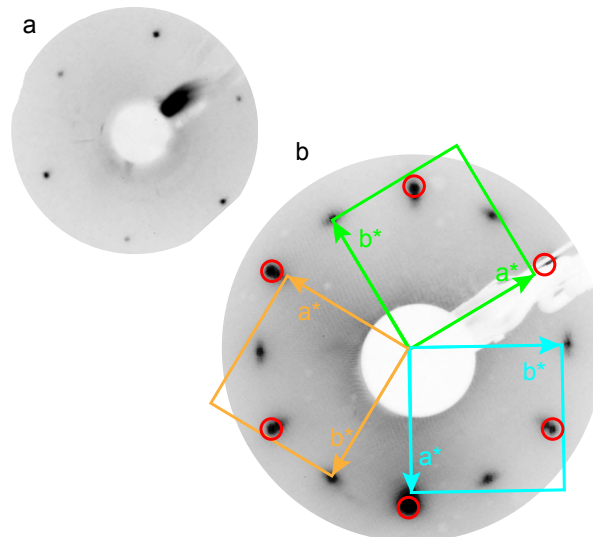


Figure 5.4: LEED pattern of Bi_2Se_3 at an electron energy of 38 eV (a), and of $\text{FeSe}/\text{Bi}_2\text{Se}_3$ at 51 eV (b). All diffraction spots in (a) and those circled in red in (b) are first order Bi_2Se_3 reflections. The remaining spots are due to FeSe. These spots are ascribed to three domain orientations. The corresponding reciprocal space unit vectors are shown in yellow, green, and blue.

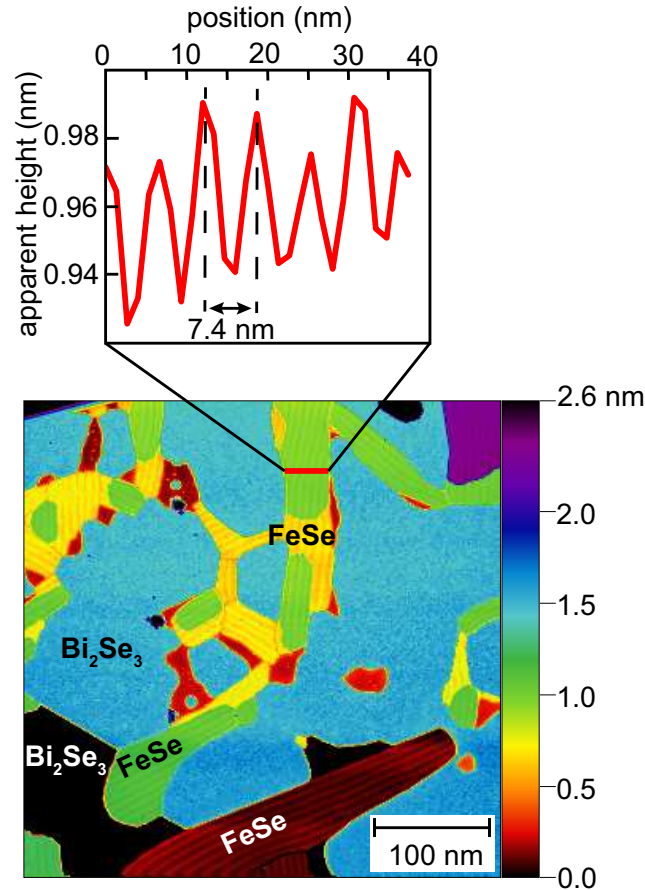


Figure 5.5: Large-scale, constant-current STM image of FeSe nanocrystals grown on Bi₂Se₃(0001). Terraces of Bi₂Se₃, separated by QL height steps (0.95 nm), and smaller step heights between Bi₂Se₃ and FeSe regions are observed. The FeSe regions show a stripe contrast in the apparent height, which is revealed by the line profile through a FeSe island at the top of the image. Bi₂Se₃ and FeSe regions are identified by atomically resolved STM, see text for details. Red patches are ascribed to Bi₂Se₃ regions, where smaller than QL height steps are observed. $U = -0.3$ V, $I_T = 1$ nA, $T = 10$ K.

5.3 STM and STS study of FeSe

The STM image of Fig. 5.5 is measured after deposition of ≈ 0.7 ML of Fe on Bi₂Se₃ at room temperature and annealing at 630 K for 10 minutes. Figure 5.5 is a large-scale STM image, which reveals the coexistence of Bi₂Se₃ and FeSe regions, as labelled in the image. The regions of Bi₂Se₃ and FeSe are identified by the atomic corrugation and symmetry of the surface, which are different for both phases. Atomically resolved STM on the Bi₂Se₃(0001) phase reveals a surface unit cell with an angle of 60° between the surface unit vectors, which have a length of approximately 4.1 ± 0.1 Å. Corresponding measurements on FeSe reveal orthogonal surface unit cell vectors with comparable length of approximately 3.8 ± 0.2 Å. Error bars are determined from the statistical error considering roughly 100 measurements.

Figure 5.5 shows mostly elongated FeSe islands, with lateral extension exceeding a few hundred nm. Their orientation suggests a preferential growth along axes, which are rotated by 60° from each other, revealing the $p3m1$ symmetry of the underlying substrate surface. A close inspection of the height levels of FeSe suggests that the FeSe nanocrystals are formed and are embedded in the Bi₂Se₃ surface. Non-integer

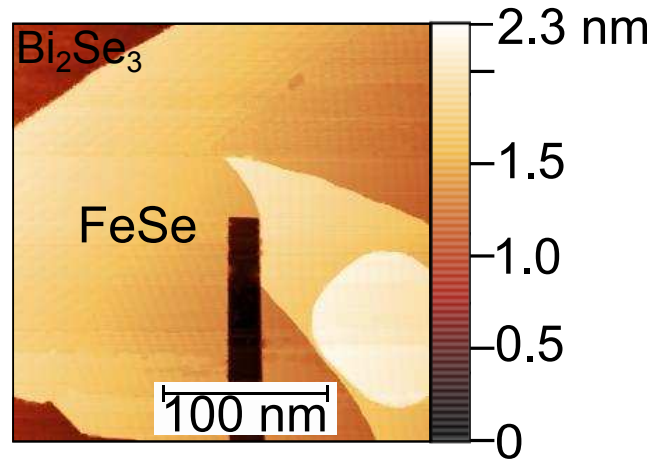


Figure 5.6: Large-scale, constant-current STM image of FeSe grown on $\text{Bi}_2\text{Se}_3(0001)$ after applying a higher annealing temperature (up to approximately 650 K). FeSe with a large lateral extension was formed, which occupies almost the whole image. $U = 0.7$ V, $I_T = 1$ nA, $T = 10$ K.

embedding depths in units of quintuple and triple layers thickness are observed. This depth distribution is characteristic for the chosen annealing temperature. A plausible reason for the complicated FeSe nanocrystals height distribution are dislocations on the Bi_2Se_3 surface, which lead to non-QL steps on the Bi_2Se_3 substrate.

A higher annealing temperature (up to approximately 650 K) leads to the formation of larger FeSe regions, separated by Fe free Bi_2Se_3 , see Fig. 5.6. At an annealing temperature as high as 670 K it becomes almost impossible to find FeSe on the sample surface. We ascribe this tentatively to a diffusion of Fe into the substrate.

Another important finding of the STM study is an observation of a stripe contrast on the FeSe islands. We ascribe the stripe pattern to a Moiré superlattice, which has been observed before in the related system Bi_2Se_3 on FeSe [167], see Fig. 5.7. The line scan in Fig. 5.5 reveals a length of 7.4 nm for the spatial periodicity of the stripe contrast.

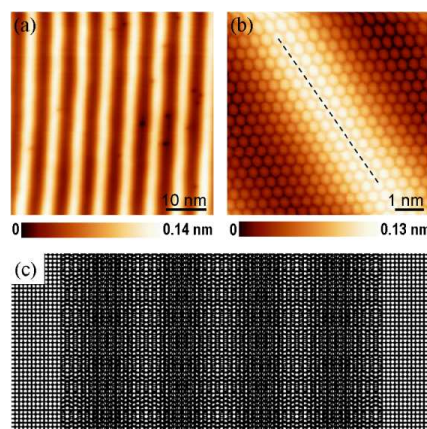


Figure 5.7: Result presented by Wang *et al.* [167]. (a) and (b) STM images of the “inverted” system: Bi_2Se_3 QL on the FeSe surface. (c) Simulation of the stripe contrast. Adopted from [167].

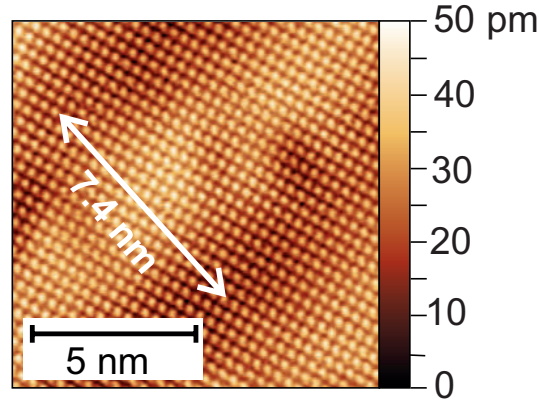


Figure 5.8: Atomically-resolved STM image of FeSe on Bi₂Se₃(0001). The stripe pattern appears as a 7.4 nm periodic modulation of the apparent height. The amplitude of this modulation is ≈ 20 pm. Tunneling parameters: $U = +0.7$ V, $I_T = 1$ nA, $T = 10$ K.

The zoom-in into a FeSe region in Fig. 5.8 shows the atomic corrugation indicative of the surface unit cell symmetry of FeSe. We point out that no surface defects are apparent in STM, and we ascribe this to the structural coherency of the FeSe nanocrystals, leading to either FeSe or Bi₂Se₃ areas. The spatial modulation with a periodicity of 7.4 nm, mentioned above (see linescan in Fig. 5.5), is indicated in Fig. 5.8. The vertical amplitude of this apparent height modulation is ≈ 20 pm. The stripe directions are predominantly aligned along the sides of the FeSe regions.

Atomic resolution STM images of the FeSe regions, see Fig. 5.9, reveal an rectangular lattice with a periodicity of 3.8 ± 0.2 Å and 3.7 ± 0.2 Å. This compares favorably with the bulk lattice constant of FeSe of 3.77 Å [24, 168]. However, the precision of the STM is not sufficient to establish beyond doubts a slight difference of the in-plane lattice vectors.

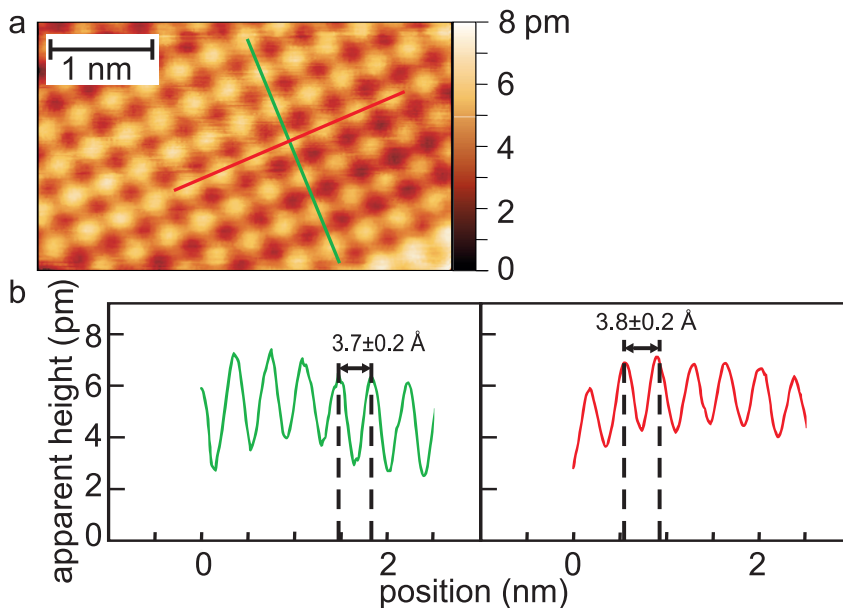


Figure 5.9: (a) STM topography image of the FeSe surface lattice. (b) Two line profiles along the crystal lattice vectors with denoted atomic distance 3.8 Å (red, perpendicular to FeSe stripe contrast) and 3.7 Å (green, parallel FeSe stripe contrast). Tunneling parameters: $U = +0.3$ V, $I_T = 0.2$ nA, $T = 10$ K.

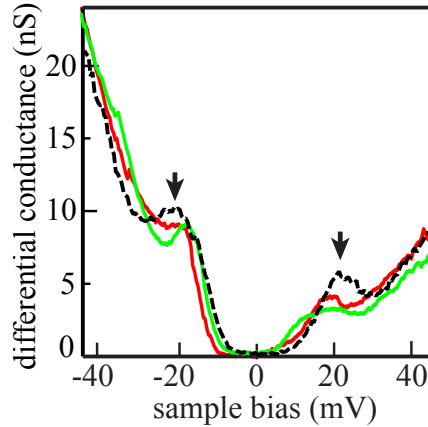


Figure 5.10: Differential conductance of a three triple layer (TL) thick FeSe nanocrystal with two peaks at +22 and -22 mV (arrows), and the gap ($dI/dV=0$) between them. Three different curves (black, red, green) were measured with the same conditions and position, one line of the STM image was scanned between the measurements. Stabilization parameters: $U_{stab} = +50$ mV, $I_{stab} = 0.5$ nA, $T = 10$ K.

The STS studies of the FeSe nanocrystals reveal two peaks at +22 and -22 mV and a gap-like feature between them, as shown in Fig. 5.10. The shape of these features are not well reproducible. The reason for this is not clear at the moment. Possible explanations are spatial variation of a possible SC state of FeSe, an effect of small variations in preparation conditions and a tip induced change in local properties of the sample.

The STS curve can be interpreted as an indicator of a SC gap. However, field and temperature depended studies have not been performed yet. My attempts to do so suffered from instabilities of the respective dI/dV measurements. These complications are ascribed to an instability of the tip apex, triggered by the close proximity between tip and sample at the chosen stabilization parameters. This effect can be reduced by an employment of lower stabilization current and higher stabilization voltage. However, this did not produce reliable results due to the low $I(V)$ and dI/dV signals.

Chapter 6

Bi bilayer on $\text{Bi}_2\text{Se}_3(0001)$

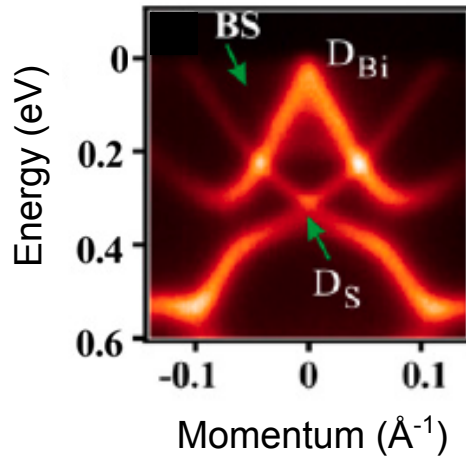


Figure 6.1: ARPES data from reference [15] taken on a Bi BL on a $\text{Bi}_2\text{Se}_3(0001)$ substrate. The following spectroscopic features are identified: Bi and Bi_2Se_3 Dirac points D_{Bi} and D_{S} , respectively, and bulk state bands (BS).

The possibility to prepare Bi BL on Bi_2Se_3 without Bi deposition, but by atomic H etching is an interesting aspect. Further, the rich electronic band structure of this system, which is established by theory and ARPES [15], see Fig. 6.1, makes it attractive for STS experiments. The idea is to exploit this system in the future to prepare MnBi, which is a perspective candidate for skyrmions [30]. This opens the way to exploit the TI surface state to control skyrmion parameters [11]. This control of skyrmions is relevant for applications in quantum computation and data storage [11].

The Bi BL has an in-plane hexagonal closed-packed structure as the Bi_2Se_3 crystal [169]. The epitaxial in-plane compressive strain of the Bi BL on Bi_2Se_3 is -9% (Bi_2Se_3 lattice constant: 4.14 \AA ; Bi lattice constant 4.54 \AA) [169].

6.1 Bi bilayer preparation by atomic hydrogen exposure

The Bi BL preparation method, which I used during my work, was adopted from the experiments presented by Shokri *et al.* [31]. The basic idea of this procedure is the exposure of $\text{Bi}_2\text{Se}_3(0001)$ to atomic hydrogen. The atomic hydrogen source is described in chapter 3.2. Atomic hydrogen consumes Se via the following reaction:

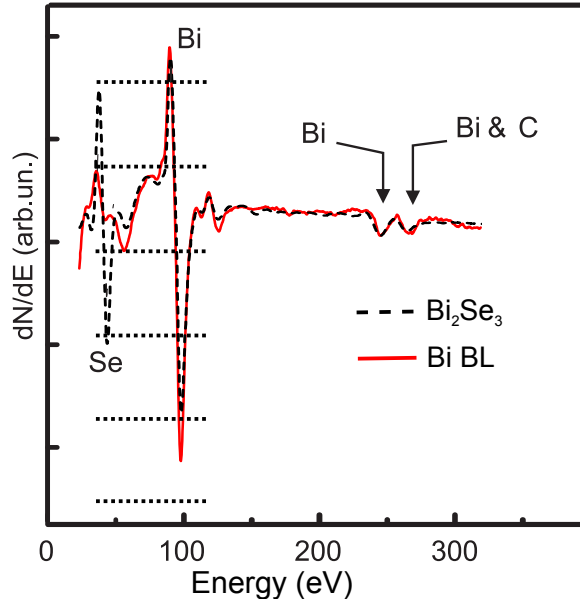


Figure 6.2: Differentiated Auger electron spectra for the Bi BL and Bi_2Se_3 surfaces. Dotted lines create an additional scale in Bi BL Se (43 eV) peak height, which shows that the intensity of the Bi (101 eV) peak is approximately 5 times larger than the intensity of Se (43 eV). Primary electron energy: 3 keV.



In addition, hydrogen also works like a sputtering gas. The results from the previous study [31] and my observations show that the sputtering influence of the hydrogen atoms is significant after the first formation of the Bi BL. The formation of the Bi BL is revealed by AES.

The AES spectrum of the $\text{Bi}_2\text{Se}_3(0001)$ sample after 2 s H-plasma exposure is given in Fig. 6.2. The previous work [31] established that the full formation of the Bi BL leads to a 0.23 ratio between the Se (43 eV) and the Bi (101 eV) peak intensities. As can be seen in Fig. 6.2, the established preparation of the Bi BL formation gives a comparable ratio of 0.2.

In the previous research by Shokri *et al.*, the ratio of 0.23 was obtained by a 1400 L (Langmuir) exposure [31]. The Langmuir defines a gas exposure to a surface, which is determined by the pressure and the time of exposure. 1 L corresponds to a surface coverage of about one monolayer. The pressure of the preparation was 5×10^{-5} mbar. The time of the preparation can be estimated as 37 seconds. To compare these parameters to our result we estimate the percentage of the atomic hydrogen to molecular hydrogen for two preparations.

Two H atoms are needed to react with one Se atoms, see eq. 6.1, and two layers of Se must be evaporated to form a Bi BL. In total, 4 L of atomic H is needed to produce a Bi BL (we need to cover the surface by atomic H atleast four times, provided the reaction probability is one). This corresponds roughly to 0.1 % of the 1400 L of molecular+atomic H used in the preparation [31]. In my preparation the sample was exposed to approximately 100 L. This corresponds to 1–2 % atomic H from H_2 .

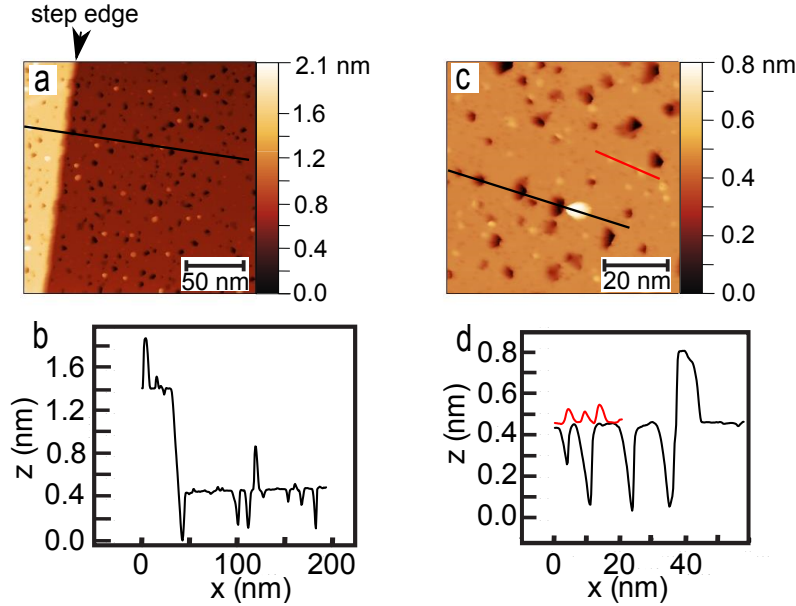


Figure 6.3: (a), (c) STM constant current images of a Bi BL surface layer on Bi_2Se_3 . The step edge of the underlying Bi_2Se_3 crystal can be seen on the image (a). An apparent height profile along the black line is shown in (b). It reveals a step height of 0.95 nm. Depressions and protrusions are shown clearer on image (c). Apparent height profiles along black and red lines are shown in (d), respectively. The line scans reveal a hole depth of 0.4 nm and two types of protrusions with 0.35 nm and 0.08 nm height. Tunneling parameters: $U = +0.5$ V, $I_T = 50$ pA. $T = 10$ K.

6.2 STM topography of the Bi bilayer surface

Constant current STM of the Bi_2Se_3 surface after the Bi BL preparation shows a superior quality due to the metallic behaviour of Bi. The topography shows flat surfaces with large terraces, separated by steps with a height of the Bi_2Se_3 QL, see Fig. 6.3. Step edges with other heights were not observed. I conclude that the surface of the Bi_2Se_3 crystal is fully covered by the Bi BL, without significant areas with deviating Bi BL coverage.

However, there are different types of the protrusions and depressions on the surface. As can be seen in Fig. 6.3(c) and (d), there is one type of depression, which can be characterized by a maximum depth of 0.4 nm. This depth correspond to the height of one Bi BL on the Bi_2Se_3 surface [31]. In addition, there are two different types of protrusions with 0.35 nm and 0.08 nm height. They are ascribed to an additional Bi BL structure and to one Se layer on the Bi BL surface, respectively [31]. The shape and the structure of these features cannot be well established due to the high mobility of Bi atoms, even at low temperature [170]. This high mobility makes Bi difficult to image in STM [169].

6.3 STS results of the Bi bilayer

Figure 6.4(d) shows two typical dI/dV curves, which were obtained on the Bi BL surface. We can clearly see two peaks at the positive sample bias at 0.2 V and 0.28 V. From the STS maps, shown in Fig. 6.4(b) and (c), I can conclude that the

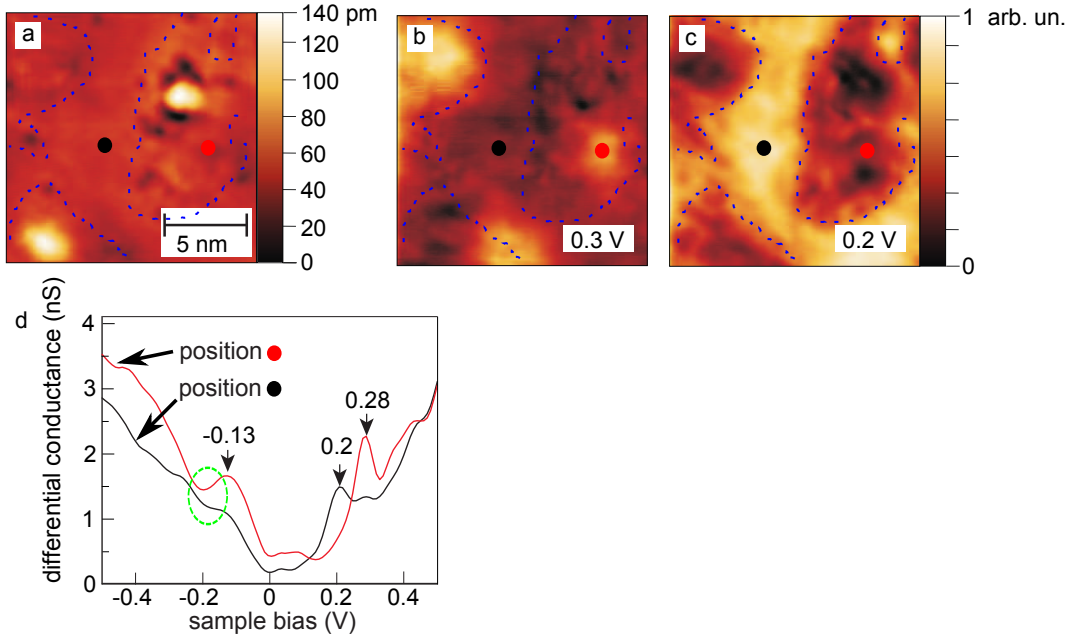


Figure 6.4: (a) STM topography images of the Bi BL surface. Tunneling parameters: $U = +0.2$ V, $I_T = 0.2$ nA. (b), (c) STS maps taken on the area (a) at the respective tip-sample voltages. (d) Two dI/dV spectra taken at different positions (indicated by black and red circles respectively). There are three peaks in the dI/dV signal (indicated by black arrows). The STS map (b) shows that the peak at 0.28 V corresponds to small areas around surface defects, while the peak at 0.2 V corresponds to the pristine Bi BL surface, which can be seen in bright in (c). The pristine Bi BL surface is denoted by dashed dark blue lines in (a), (b) and (c). Also we can see that the peak at -0.13 V is pronounced in the red curve (d). However, we can also notice that this feature is present in the black curve also. A dip (encircled by green) near the peak at -0.13 V can be attributed to the Bi_2Se_3 surface state Dirac point.

peak at 0.2 V corresponds to the pristine Bi BL. The peak at 0.28 V corresponds to areas with defects. However, not all defects lead to the presence of this peak.

We can also identify a peak at -0.13 V with a subsequent dip in dI/dV spectroscopy. This peak is pronounced close to the defects. Similarly to the STS studies of Bi BL on the Bi_2Te_3 surface [171], I can speculate that the dip at -0.2 V corresponds to the Bi_2Se_3 surface state Dirac point.

Under these assumptions we can clearly say that during the preparation of the Bi BL the electronic band structure of the Bi_2Se_3 surface was also modified. The Dirac point was shifted from -0.3 V (see chapter 4) to -0.2 V.

Previously, similar effects on the electronic properties of the Bi_2Se_3 surface were obtained by carbon surface doping [19]. However, further ARPES and theory studies are needed to clarify this point.

Chapter 7

Discussion

7.1 Tuning the Bi_2Se_3 thermal annealing procedure

The preparation procedure of Bi_2Se_3 consists of two steps: sputtering (Ar ion bombardment) and thermal annealing. For a better understanding of the obtained results, sputtering and annealing on the *in vacuo* cleaved samples were studied separately.

Figure 7.1 shows the Bi_2Se_3 surface after sputtering. The formation of “wormlike” structures is observed. The largest step height, extracted from the STM image, is approximately 0.87 nm, which is 0.08 nm lower than 1 QL step height. However, this difference can be explained by the presence of narrow fissures. These features are possibly sharper than the tip apex, which prevents the apex from reaching the bottom of the fissure. This makes the apparent depth of the fissure smaller.

This assumption helps to interpret the apparent heights properly. Thus we need to add 0.08 nm correction to the height scale of the STM image. This will give us the heights measured from the lowest level, which corresponds to the last Se layer of the underlying QL. This operation gives $0.33 + 0.08 = 0.41$ nm and $0.62 + 0.08 = 0.7$ nm. The first result coincides with the thickness of a single Bi BL obtained by SXRD [31]. The second result corresponds to a Se-Bi-Bi-Se structure [31]. The presence of a Bi BL means that the sample is depleted of Se after the ion bombardment. This indicates preferential sputtering of Se, which is plausible as the Se atomic mass is three times lower than that of Bi [172, 173].

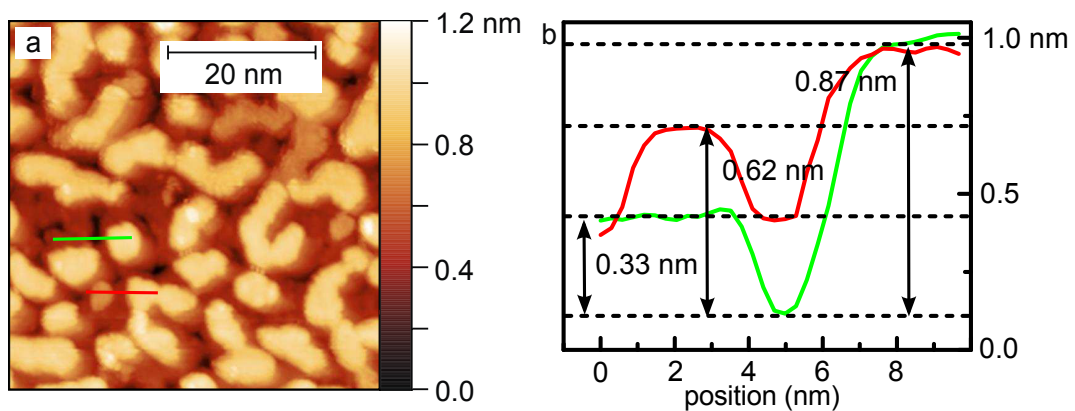


Figure 7.1: (a) STM image of an *in vacuo* cleaved Bi_2Se_3 sample after ion bombardment (ion beam energy: 400 eV, sample current density ≈ 20 nAmm $^{-2}$, 15 min). Tunneling parameters: $U = +0.4$ V, $I_T = 200$ pA. The image reveals four different height levels, as indicated by the line profiles (b) along the green and red lines shown in (b).

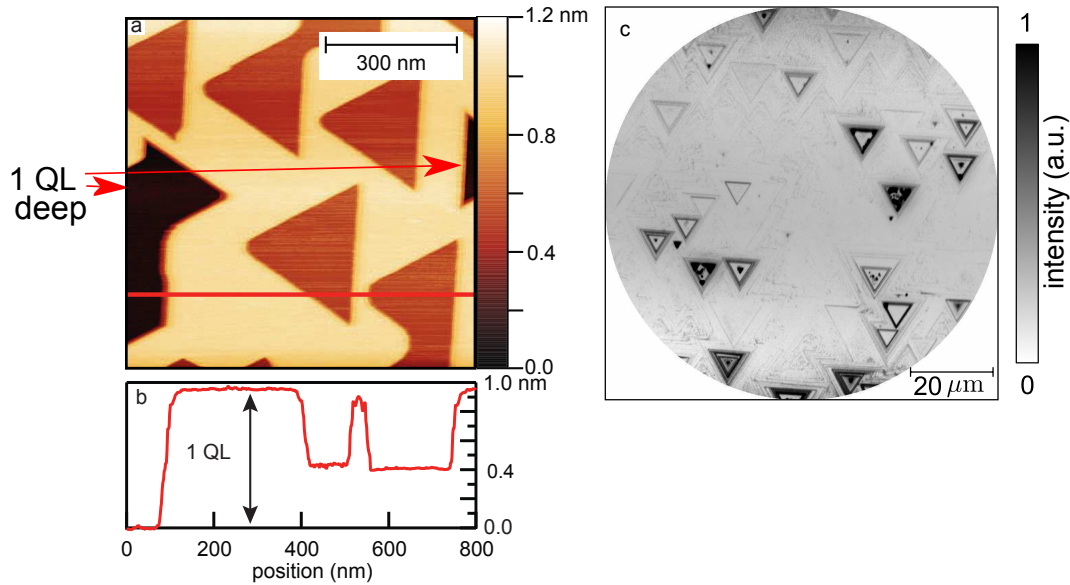


Figure 7.2: (a) STM image of the *in vacuo* cleaved sample without ion bombardment after three 30 min long annealing processes at 620 K. Tunneling parameters: $U = +0.4$ V, $I_T = 200$ pA. Depressions with two distinct depths can be clearly distinguished: the depths are either 1 QL (0.95 nm) or 0.50–0.55 nm, as indicated in (b) by the line profile along the red line shown in (a). (c) Photoemission electron microscopy (PEEM) image of Bi_2Se_3 surface, cleaned by sputtering-annealing cycles. A Hg-Xe discharge lamp was used ($h\nu = 5.9$ eV) [164]. An enhanced photoemission from edges of triangular substrate surface structures is seen.

I also studied the annealing of *in vacuo* cleaved crystals, without sputtering. Figure 7.2(a) shows that annealing at 620 K creates triangular depressions on the surface. They are 0.95 and 0.55 nm deep, respectively. Our observation of the change of morphology during a series of annealing steps at 620 K suggests that the depressions are formed by atomic evaporation from the surface. Similar observations were obtained during thermal desorption of Se from a Bi_2Se_3 crystal [174]. The depression formation begins with nm-sized triangles, which grow to a lateral size of hundreds of nanometers.

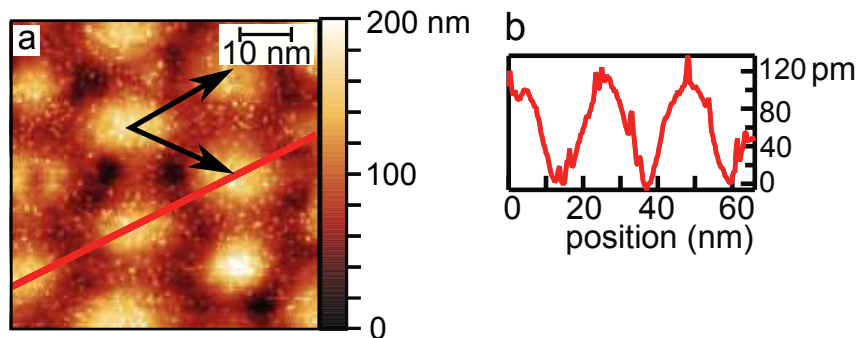


Figure 7.3: STM image of a Bi_2Se_3 sample, which was sputtered and subsequently annealed at 620 K (a). $U = +500$ mV, $I_T = 1$ nA. A quasi-hexagonal superstructure with 20–23 nm periodicity is visible in constant current images (black arrows show corresponding unit cell vectors). The apparent height amplitude is approximately 100 pm, as revealed by the line scan of (b). On top of this modulation, some protrusions appear with an apparent height of 40 pm, see also Fig. 7.4(a) and (b).

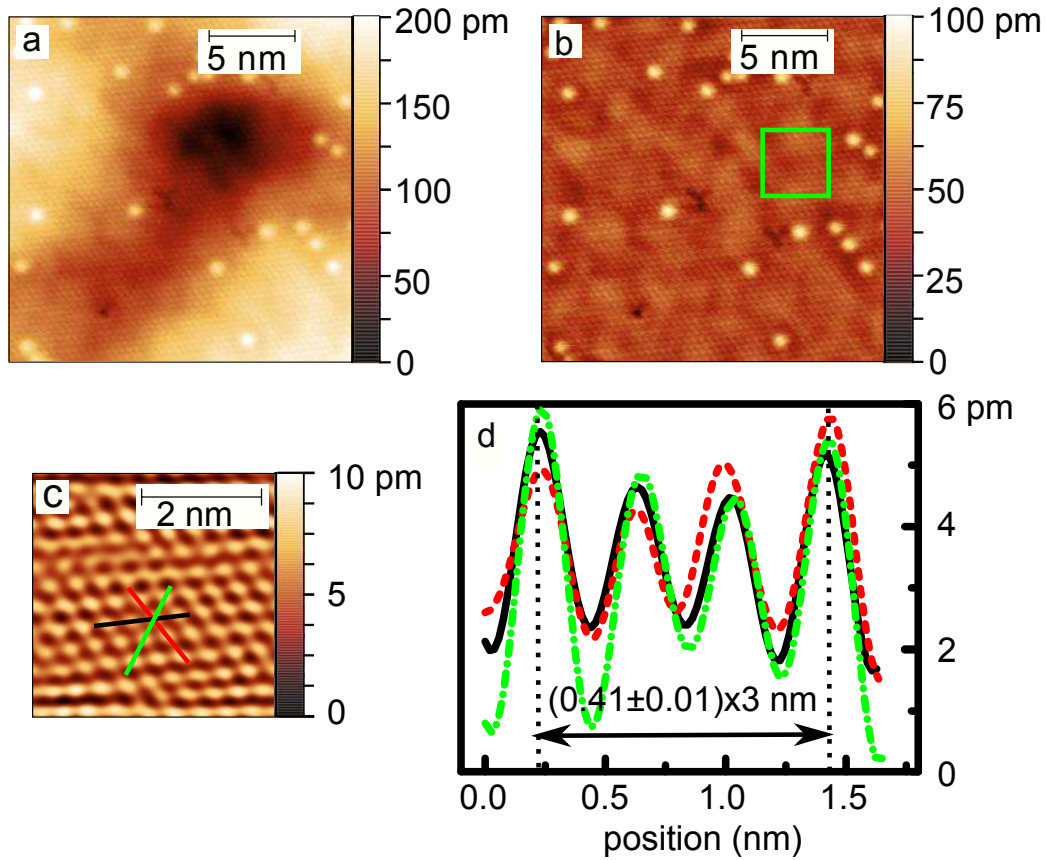


Figure 7.4: (a) STM image of Bi_2Se_3 (zoom-in into region shown in Fig. 7.3(a)) ($U = +0.5$ V, $I_T = 0.7$ nA). (b) Region of (a) after subtraction of a polynomial surface, 5th order fit. (c) Zoom-in of the area in the green square. Atomic resolution STM images in (b) and (c) show an hexagonal surface corrugation. Atomic distances are equal within the error bar to the surface lattice constant of the pristine Bi_2Se_3 crystal surface, 4.1 ± 0.1 Å, see chapter 4. This is shown in (d) by line profiles along the black, red and green lines in (c) respectively

The evaporation starts around defects. In case of Bi_2Se_3 it was reported that screw dislocations play the main role in this process [174]. Screw dislocation is a linear defect which creates the overlapping of the different atomic planes. So there is a screw like structure inside the crystal which is presented on the surface as a step with a height which is smaller than the structural cell size [175]. This explains the depth of the depressions, which is not equal to the thickness of 1 QL.

The formation of triangular depressions during the annealing process can also be seen in the PEEM image (see Fig. 7.2(c)), which was taken on a similarly prepared sample by my colleagues [164]. These depressions can grow in size up to $10 \mu\text{m}$. As was shown in Fig. 4.4, this surface modification leads to changes of sample reflectivity and to the destruction of the surface, if the annealing temperature was higher than 700 K, or if the annealing time was increased to one hour.

Ion bombardment and subsequent annealing at $T_{\text{ann}} \approx 620$ K leads to the formation of a long-range quasi-hexagonal superstructure, as shown in the constant current image of Fig. 7.3. Although the unit cell vectors of the superstructure are not exactly defined due to disorder in the superlattice, we can estimate their lengths to be of the order of 20–23 nm. On top of the long-range modulation we observe sub-nm wide, circularly shaped, irregularly arranged protrusions with an apparent

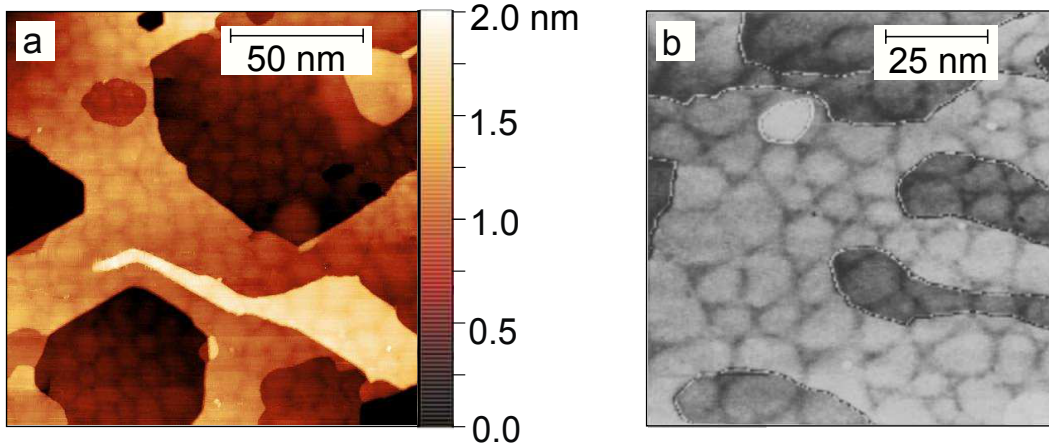


Figure 7.5: (a) STM image of Bi_2Se_3 . Tunneling parameters: $U = +0.3 \text{ V}$, $I_T = 0.2 \text{ nA}$. (b) For comparison: the STM image of a NiPt alloy with a subsurface dislocation network, presented by M. Schmidt *et al.* [173]. The morphology of defects in (a) and (b) looks similar, and this is an indication of a subsurface dislocation network in the Bi_2Se_3 crystal.

height of $\approx 0.4 \text{ \AA}$, e.g. see the small protrusions in Fig. 7.3 and Fig. 7.4. The protrusions cannot be manipulated by the STM tip. This may suggest that they are not adsorbates on the otherwise ideal Bi_2Se_3 surface, but rather atoms embedded below the surface in the QL.

To underline that the quasi-hexagonal superstructure has no significant effect on the atomic corrugation, the STM image after subtraction of the surface, which was obtained by polynomial fit of this image, is presented in Fig. 7.4. Also the clover shaped surface defects, interpreted as vacancies [16] are better seen in Fig. 7.4 (b) after this background subtraction.

According to our results the origin of the quasi-hexagonal superstructure are subsurface defects, which are produced by the ion bombardment. The surface itself presents a top atomic layer with bulk-like corrugation.

A comparison of the large scale image of the Bi_2Se_3 surface with the image from the work by M. Schmidt *et al.* [173] on NiPt indicates striking similarities, as shown in Fig. 7.5. The semi-periodic structure and the superstructure connection through the step edges speaks in favor of a subsurface dislocation network. Mechanical distortions driven by high dislocations density, as was shown in articles [172, 173], can lead to the formation of a preferable recurrent net.

The work by M. Schmid and co-authors present an example, where preferential sputtering of one of the substrate components occurred [172, 173]. We speculate that preferential sputtering of Se could be the reason for the subsurface dislocation formation in the Bi_2Se_3 crystal. Due to the high density of these dislocation a periodic modulation pattern is formed on the surface.

7.2 Bi_2Se_3 surface states

STS of Bi_2Se_3 , prepared by sputtering annealing cycles, is shown in Fig. 7.6 (b). The dI/dV spectroscopy signal is almost constant between -0.07 and -0.34 V , with a shallow dip around -0.3 V . At neighboring voltages the dI/dV signal increases sharply.

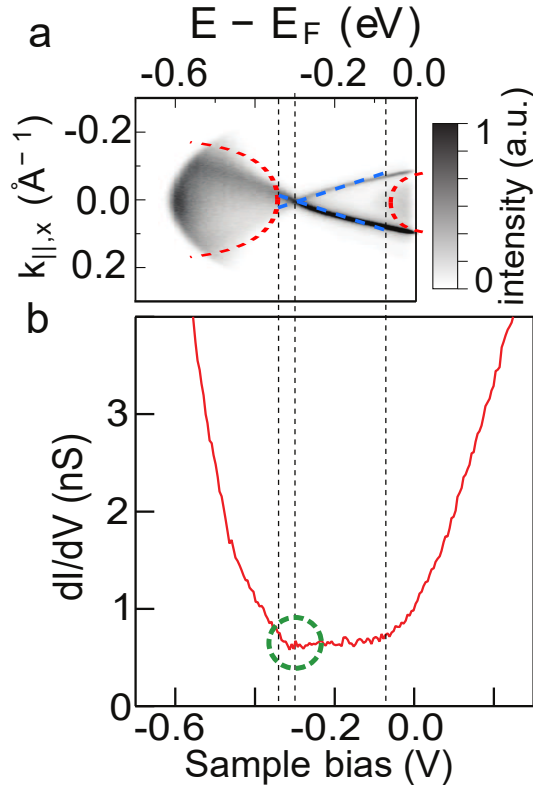


Figure 7.6: (a) Photoemission electron spectroscopy on the sample characterized in Fig. 4.9. It shows a linearly dispersing surface state (Dirac cone, denoted by blue dashed lines) crossing at the Dirac point near -0.3 eV. Bulk bands are schematically shown by red dashed lines. (b) STS of Bi_2Se_3 with a shallow dip at the Dirac point (marked by the green circle).

To explain this result I provide a photoemission electron spectroscopy of the same sample obtained by my colleagues [164], see Fig. 7.6(a). For the sake of simplicity I neglect the second direction of k_{\parallel} in my qualitative discussion.

In Fig. 7.6(a) we can see two linear dispersion branches (denoted by blue dashed lines) which cross each other around -0.3 eV below the Fermi level. These lines of high intensity are interpreted as a section of the so-called Dirac cone, which is a surface of revolution around the $k_{\parallel} = 0 \text{ \AA}^{-1}$ axis in (k_{\parallel}, E) space. The Dirac cone is a double-cone with the apex called Dirac point.

We can also see in Fig. 7.6(a) an additional wide blurred signal in a range higher than -0.070 eV and lower than -0.34 eV, with the intensity increasing towards the boundaries of the figure. We can see that the integration over the intensity and k_{\parallel} will give us almost constant DOS between -0.07 and -0.34 eV, with a narrow dip around -0.3 eV, while it increases in the neighboring region. This photoemission result corresponds nicely to the dI/dV signal in (b).

Previous photoemission studies and theoretical results [15, 176, 177] showed that Bi_2Se_3 has a bulk band gap of approximately 0.3 eV [177], which lies below the Fermi level due to the usual n-doping of the Bi_2Se_3 crystals [15]. Thus, the band gap was observed between approximately -0.1 and -0.4 eV. In the same articles, a topologically protected surface state with linear dispersion was reported, which lies inside the bulk band gap, with the Dirac point around -0.3 eV. The experimental studies were done previously on cleaved Bi_2Se_3 crystals. The n-doping

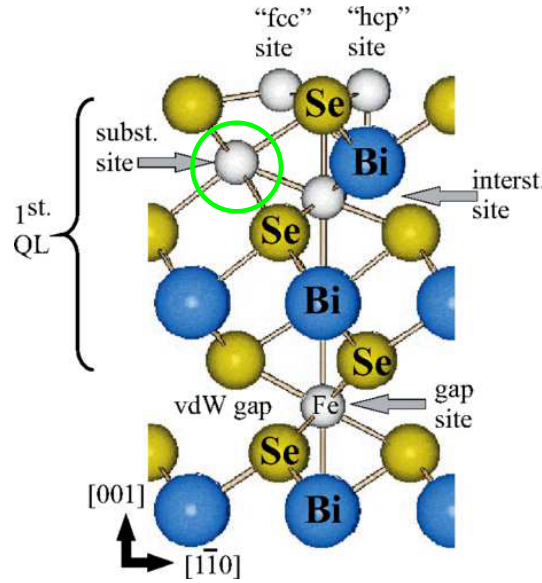


Figure 7.7: Possible adsorption sites for iron on $\text{Bi}_2\text{Se}_3(0001)$ [166]. Substitutional site (encircled by green) was shown to be preferential for Fe atoms by X-ray absorption fine structure and theoretical predictions [166].

was explained by the presence of Se vacancies, which were shown to be double donors by first principles calculation [178]. Our STM images also show subsurface defects (see chapter 4), which are interpreted as Se vacancies [159, 179], in agreement with the previous discussion.

Thus, I interpret the STS curve, see Fig. 7.6(a), as a signature of the surface Dirac cone inside the bulk band gap, which extends from -0.07 to -0.34 eV, with the Dirac point at -0.3 eV. The width of the band gap is approximately 0.27 eV.

The TI surface state should be robust against any surface defect [2, 64, 65]. Thus, one may expect that it is always possible to detect by STS the surface state Dirac cone feature. However, the spatial location of the TI surface state is determined by surface conditions. Surface defects move the TI border deeper to the bulk, away from the surface.

The STM constant current images of the surface (see chapter 4) prepared by sputtering and subsequent annealing show a clean surface with a contamination of less than 1%, see Fig. 4.9. The amount of subsurface defects is similar to that obtained after the cleavage procedure. The observation of the TI surface state in the STS curve (see Fig. 7.6(b)) is not only a new report on the Bi_2Se_3 Dirac cone state, but it is also a confirmation of the successful preparation of the $\text{Bi}_2\text{Se}_3(0001)$ surface by sputtering and annealing cycles.

7.3 Formation of FeSe nanocrystals on the Bi_2Se_3 surface

FeSe is prepared by Fe deposition onto $\text{Bi}_2\text{Se}_3(0001)$ at 300 K, followed by annealing at $T \approx 620$ K. X-ray absorption fine structure (XAFS) shows that, during the deposition, among all possible sites for Fe, see Fig. 7.7, the preferential one is the substitutional site, where Fe replaces Bi atoms [166]. Also it was shown that mild

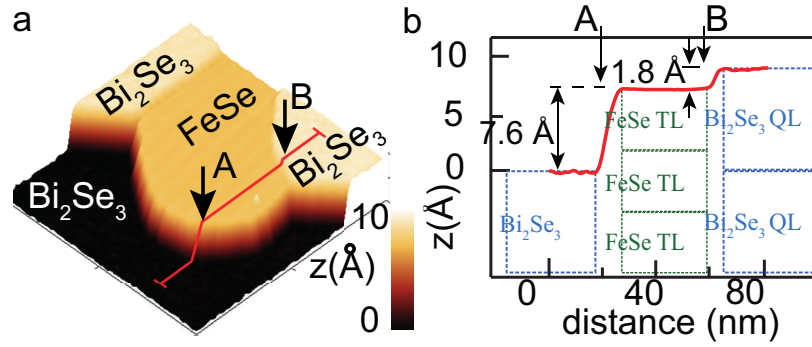


Figure 7.8: (a) Constant-current STM topography image ($100 \times 100 \text{ nm}^2$) of an embedded FeSe nanocrystal on Bi₂Se₃. (b) The line profile across the FeSe island indicates step heights of 7.6 and 1.8 Å which can be rationalized by the model of an embedded FeSe nanocrystal.

annealing up to 520 K leads to a bulk-like FeSe crystal structure formation with a local order up to the 6th shell at a distance of $\approx 6 \text{ \AA}$ [166].

Figure 5.5 reveals that FeSe islands appear either slightly lower or higher than the surrounding Bi₂Se₃ substrate. The apparent height difference between FeSe and Bi₂Se₃ areas is often negative, $\Delta z = z_{\text{FeSe}} - z_{\text{Bi}_2\text{Se}_3}$. A plausible explanation is that FeSe nanocrystals are embedded in the Bi₂Se₃ crystal, i.e. they extend below the Bi₂Se₃ surface.

A dedicated STM measurement enables a closer look onto the step heights occurring in an area around FeSe nanocrystals. Figure 7.8 shows a 3D representation of that STM measurement. Here, atomically resolved STM identifies the terraces as either Bi₂Se₃ or FeSe, due to their distinctly different surface symmetries. This will be discussed below. The apparent-height profile (red line) in Fig. 7.8(b) presents three different levels, separated by $\Delta z = 7.6$ and 1.8 \AA , respectively. These values are compatible with a 3 TL thick embedded FeSe nanocrystal, as illustrated by the sketched stacking of FeSe TLs and Bi₂Se₃ QLs.

However, not all the step heights are straightforwardly identified due to the possible occurrence of surface defects on the underlying Bi₂Se₃, and the resulting small differences between the heights of the different stacking models. Quantitative insight about the average FeSe thickness was obtained by SXRD by my colleagues [164].

The SXRD experiments reveal an average lattice parameter of $c = 5.74 \text{ \AA}$ for the thickness of one TL FeSe. This reflects a lattice expansion along the vertical direction in comparison with the FeSe bulk value ($c^{\text{bulk}} = 5.51 \text{ \AA}$). This difference indicates a lattice strain along the out-of-plane direction of $\epsilon_3 = +4.2\%$.

The combined use of SXRD, LEED and STM provides insight into the peculiar growth mode resulting from the deposition of Fe on Bi₂Se₃ and subsequent annealing. We speculate that there is an upper limit for the thickness of FeSe nanocrystals which can be prepared this way on Bi₂Se₃. The average thickness of the FeSe nanoislands is three TL. This limit is probably given by the maximum depth from which Se atoms can be extracted from the bulk of Bi₂Se₃ to form FeSe. This growth process is thus different from the progressive build-up of FeSe TLs obtained when co-depositing Fe and Se [180–182].

After Fe deposition Fe atoms start to substitute Bi in the top QL of the Bi₂Se₃ crystal. The annealing procedure initiates the formation of FeSe sub-nm crystals

and then helps to unite small FeSe inclusions into FeSe nanoislands. The amount of iron limits this process.

The open question is, what happens to the Bi atoms? Further research is needed to understand the fate of Bi in this process. Currently, there are three different speculations on this. The Bi atoms can desorb from the surface during annealing. Bi atoms, which stay on the surface, can be taken into account as surface contamination. The high surface mobility of the usual contamination on the Bi_2Se_3 surface speaks in favor of this. Finally, the Bi atoms can also migrate into the crystal and form bulk defects.

7.4 FeSe nanocrystal: in-plane crystal structure

The starting point of the discussion is an analysis of the 7.4 ± 0.8 nm periodic stripe pattern, which is reminiscent of that observed for a few atomic layer thick Bi_2Se_3 film grown on a bulk FeSe crystal [167], see Fig. 7.10(c).

The different atomic spacing of Bi_2Se_3 and FeSe gives rise to a Moiré structure by superimposing the corresponding surface unit cells. The heterostructure represents a Moiré coincidence superlattice with period λ , where

$$\lambda = a_{\text{FeSe}}n = d(n + 1) \quad (7.1)$$

and a , d are indicated by the sketch in Fig. 7.11(b). With the bulk Bi_2Se_3 in-plane lattice constant for the substrate, $4.14 \text{ \AA} = d\frac{2}{\sqrt{3}}$, Eq. (7.1) yields $a_{\text{FeSe}} = 3.77 \text{ \AA}$ and $n = 19.6 \pm 2.2$ for $\lambda = 7.4$ nm.

An angle α between the FeSe lattice and the Moiré stripe direction, see Fig. 7.11(a), was observed. This angle indicates a rotation between the Bi_2Se_3 and the FeSe lattice. The model of Fig. 7.11(b) shows the simplest case of an alignment with vanishing rotation between the sublattices, *i.e.* $\alpha = 0$. As a result, the symmetry of

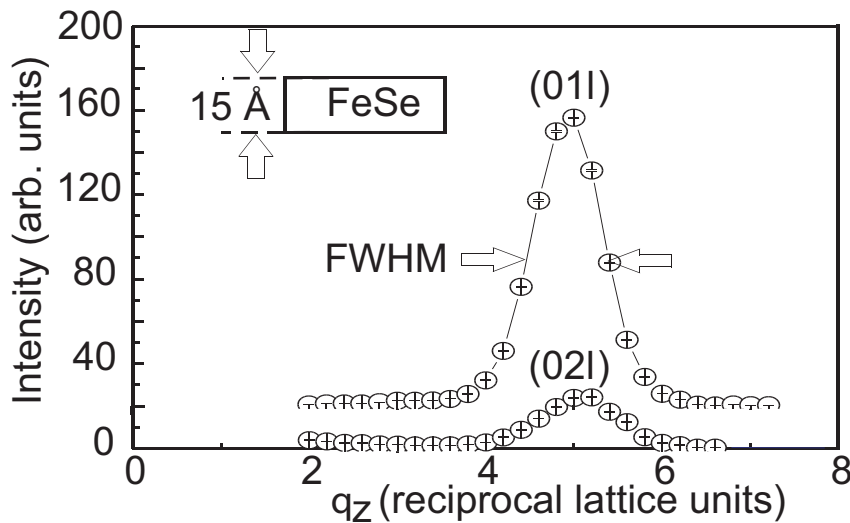


Figure 7.9: X-ray intensity along the first $(01l)$ and second $(02l)$ order rod of FeSe on Bi_2Se_3 . The finite full width at half maximum corresponds to a film thickness of $t \approx 15 \text{ \AA}$, while the peak position is related to a lattice constant of $c \approx 5.74 \text{ \AA}$. A reciprocal lattice unit equals to $(28.64 \text{ \AA})^{-1}$ [164].

the FeSe nanocrystal is lowered from tetragonal in bulk to two-fold ($a \neq b, \gamma = 90^\circ$) by proximity to the substrate.

Next, the LEED results are analyzed. For the sake of simplicity I start with the analysis of a single FeSe domain, shown in real space in Fig. 7.12(a). The surface unit cell is shown by a solid blue line, while the solid red circles represent the lattice points of the trigonal Bi_2Se_3 substrate in real space. Due to the symmetry of the substrate, we expect three rotated domains, and the other two domain orientations of FeSe are shown by faint blue lines in (a). They originate from the first domain by a rotation by 120° and 240° .

The resulting LEED pattern shows diffraction spots due to the trigonal substrate unit cell, and due to FeSe in three rotational domains. The calculated resulting pattern [183] is superimposed with the measured diffraction pattern in Fig. 7.12(c). Here, red dots represent diffraction spots due to $\text{Bi}_2\text{Se}_3(0001)$, and blue dots are due to diffraction from FeSe in three domains.

The six plus six sets of FeSe spots form inequivalent alternating equilateral triangles in the outermost ring (green and blue dashed triangles in Fig. 7.12(b)). The difference in area between the dashed triangles directly indicates a difference between the lengths a and b , which were introduced in (a). This finding was established by the variation of the model parameters. This difference signifies an orthorhombic symmetry of FeSe on Bi_2Se_3 . Analyzing the positions of the diffraction spots we obtain $b/a = 1.02 \pm 0.01$, which translates to $b_{\text{FeSe}} = 3.85 \pm 0.04 \text{ \AA}$, with the STM Moiré analysis estimate of $a_{\text{FeSe}} = 3.77 \pm 0.02 \text{ \AA}$.

Thus, the in-plane lattice constants of the orthorhombic FeSe nanocrystals are obtained.

The orthorhombicity of FeSe is much larger than that of the phase in the phase transition [162], which happens around the 90 K and is usually employed in the

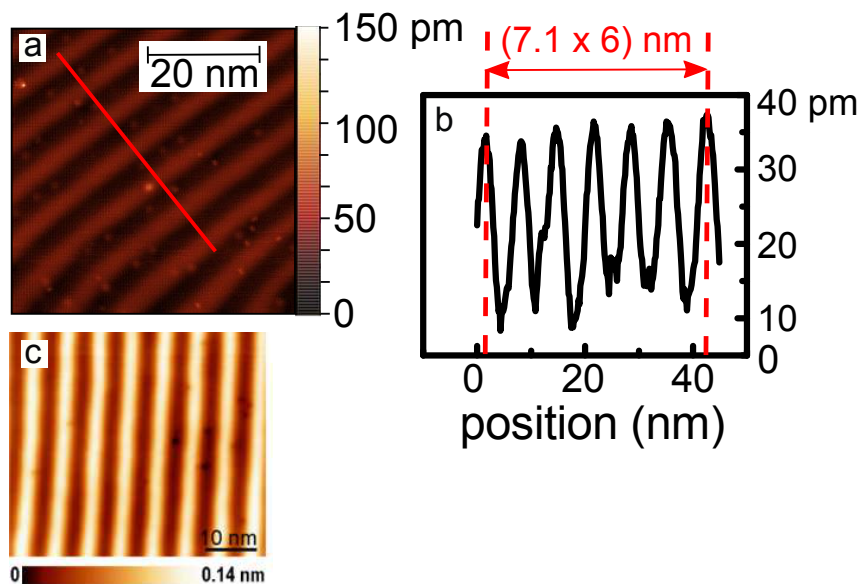


Figure 7.10: (a) STM image of FeSe on $\text{Bi}_2\text{Se}_3(0001)$. A periodic stripe pattern is visible. Tunneling parameters: $U = +700 \text{ mV}$, $I = 200 \text{ pA}$. The amplitude of this modulation is $\approx 20 \text{ pm}$ and the periodicity is 7.1 nm , which is clear in the line profile (b), taken along the red line in (a). (c) An example of a STM image of the inverted system, Bi_2Se_3 on FeSe, adopted from Wang *et al.* [167].

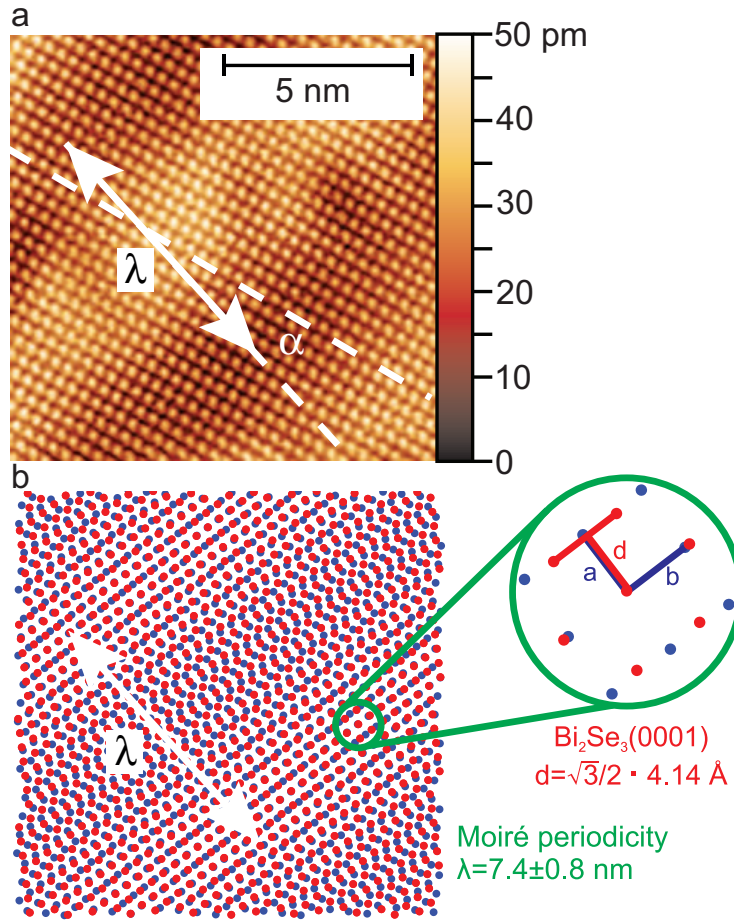


Figure 7.11: (a) STM image of FeSe on Bi₂Se₃(0001). A 7.4 nm periodic modulation, as indicated by the white arrow, of the apparent height of the FeSe lattice is clearly visible. The amplitude of this modulation is ≈ 20 pm. Tunneling parameters: $U = +300$ mV, $I = 200$ pA. α is the angle between the normal to the stripe pattern ridge and the FeSe lattice vector. (b) The schematic diagram presents a Moiré coincidence lattice generated by the superposition of Bi₂Se₃ (red) and FeSe (blue) unit cells, each represented by a circular dot. Along the direction λ the FeSe unit vector a does not match the length d , see sketch at the right. A coincidence between the two lattices thus appears every n repetitions, see text for details. The period λ , indicated by the white arrows, characterizes this coincidence Moiré superlattice.

discussions about nematicity of FeSe (2% and 0.5% difference between a and b constants respectively) [184]. Thus, FeSe formed here is distinctly different from that obtained in the temperature phase transition.

7.5 FeSe on Bi₂Se₃: a candidate for an unconventional superconductor

The highest T_c of the FeSe thin film was reported by Ge and co-authors [23]. With a four probe technique they observed zero resistance of FeSe on STO up to 100 K. The largest observed gap in the electron DOS was reported by Wang *et al.* [22]. The STS spectra of unit cell thick FeSe from this work is shown in Fig. 7.13(b). The size of the SC gap (from -20 to $+20$ meV) is similar to the STS spectra of the FeSe nanocrystal, which was observed by us, see Fig. 7.13(a).

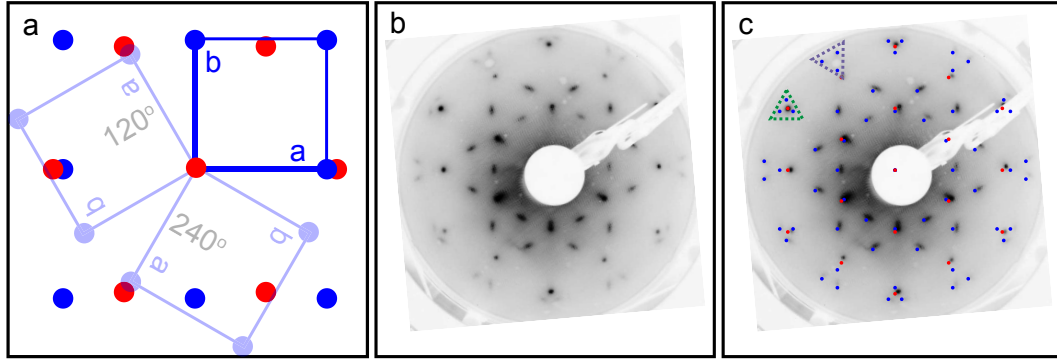


Figure 7.12: (a) Real-space model of the surface atomic positions of Bi₂Se₃(0001) (solid red circles) and FeSe (solid blue circles) in three rotational domains. This structural model is used to calculate the LEED pattern in (c) [183]. Red and blue dots correspond to diffraction from Bi₂Se₃ and FeSe, respectively. (b) Experimental LEED image at 97 eV. (c) Superposition of the calculated LEED pattern and the experimental LEED pattern (b).

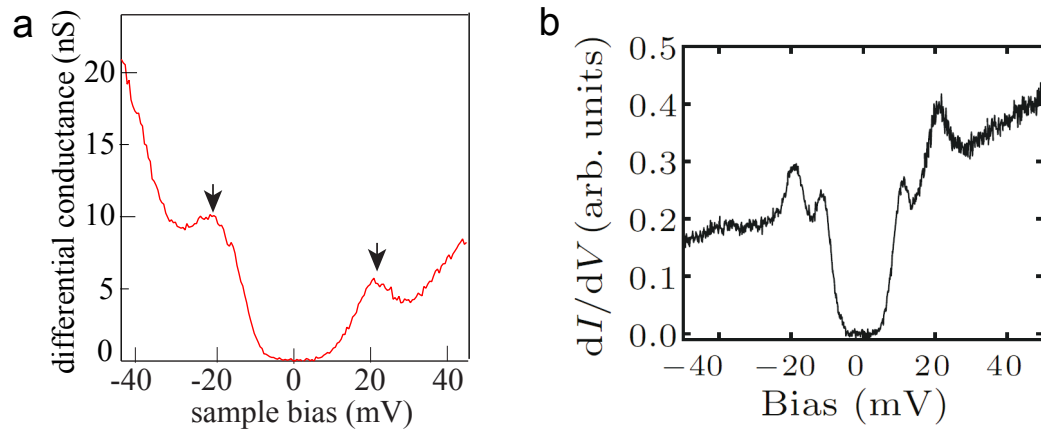


Figure 7.13: (a) Differential conductance of a three triple layer (TL) thick FeSe nanocrystal with two peaks at +22 and -22 mV (arrows), and the gap ($dI/dV=0$) between them. Stabilization parameters: $U_{stab} = +50$ mV, $I_{stab} = 0.5$ nA, $T = 10$ K. (b) For comparison: Tunneling spectrum taken on the TL of FeSe on SrTiO₃(001) (STO) at 4.2 K adopted from reference [22].

In conventional SC, discussed in chapter 2, the critical temperature (T_c) and the SC gap size (Δ_{SC}) are linked via BCS theory ($\frac{2\Delta_{SC}}{k_B T_c} = 3.52$).

However, the magnitude of this ratio for bulk FeSe is linked to a phenomenological description [95]:

$$\frac{2\Delta_{SC}}{k_B T_c} = 5.5. \quad (7.2)$$

This ratio was also used by Wang *et al.* [22]. Considering data from thin FeSe films [22, 88] then the ratio coefficient is approximately 5.8–6.1. However, SC in FeSe is not fully understood yet, thus it is better to use the common 5.5 ratio for our estimate. The observed gap $2\Delta_{SC} = 44$ meV suggests within this model a critical temperature as high as 92 K.

Another important parameter of the SC state is the critical field. A vortex in SC FeSe on STO was observed at 11 T [22]. This means that the critical field condition of SC FeSe requires high fields beyond our maximum field of 8 T.

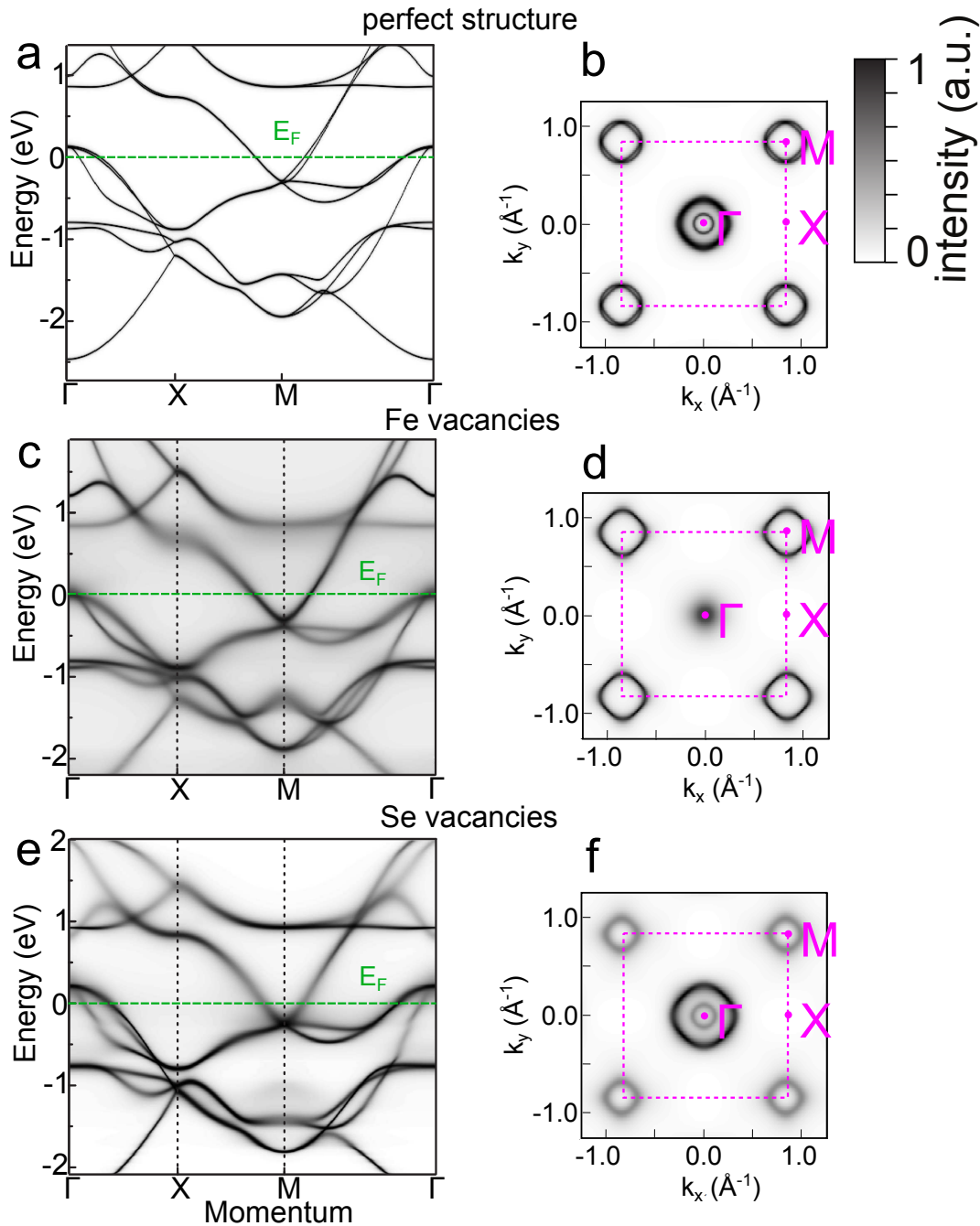


Figure 7.14: Band structures (a), (c), (e) and Fermi surfaces (b), (d), (f) of pristine FeSe (a), (b), FeSe with Fe vacancies (c), (d) and Se vacancies (e), (f). In both cases, vacancy concentrations are 5% of the respective atom. The FeSe unit cell volume is approximately 83 \AA^3 with one Fe and two Se atoms per unit cell. This means $0.6 \times 10^{21} \text{ cm}^{-3}$ is the concentration of the Fe vacancies, and $0.3 \times 10^{21} \text{ cm}^{-3}$ is the concentration of the Se vacancies. The surface Brillouin zone (edge length 1.67 \AA^{-1}) of FeSe is indicated by dashed squares in (b), (d), (f) and the Γ -, M- and X- points are indicated respectively. The closed contours in (b), (d), (f) identify so-called electron (at the M-points, positive electron effective mass) and hole (at the Γ -point, negative electron effective mass) pockets, respectively. Calculations were performed and provided by Athur Ernst from the MPI theory department.

Why can the T_c of the FeSe film be higher than the T_c of bulk FeSe? Arthur Ernst, my colleague from the theory department MPI (Halle), studied a strain effect on the FeSe electronic band structure, and he did not find any significant changes. Also the thickness of FeSe does not play a role, when it is larger than one UC (our sample is 3 UC thick). However, the stoichiometry of the FeSe film is shown to have a great impact on the electronic bands. In Fig. 7.14 we can see three different cases of electronic band structures and Fermi surfaces of FeSe: pristine FeSe, FeSe with Fe vacancies and with Se vacancies.

In Fig. 7.14(b), (d), (f) Fermi surfaces of pristine FeSe (b), FeSe with Fe vacancies (d) and FeSe with Se vacancies (f) are presented. The definition of electron and hole Fermi pockets is necessary to discuss these results. An electron/hole pocket is a contour of the Fermi energy in the Brillouin zone with a positive/negative electron effective mass. As can be seen in Fig. 7.14(b) there are Fermi pockets at the Γ and M-points in pristine FeSe. We can clearly see the bands in the electronic band structure (a), which correspond to these pockets. Thus, a hole pocket at the Γ -point and four electron pockets at the M-points in the FeSe surface Brillouin zone are expected in the calculation. When the Fe vacancies are considered, we can see in Fig. 7.14(c) that the band at the Γ -point is moving down in energy, and it reduces its weight at the Fermi level, while the band at the M-point is also moving down in energy and thus the corresponding electron pockets increase in size in the Fermi contour, as can be seen in Fig. 7.14(d). The Se vacancies give us an opposite effect, see Fig. 7.14(e) and (f). Also one can notice that the band at the M-point becomes shallower. The position of the Fermi level tells us that Fe vacancies are “donors”, while Se vacancies are “acceptors”, this result was already shown in previous works [133, 185].

The observations during the preparation of the FeSe nanostructures on Bi₂Se₃, discussed in chapter 5, tell us that during the sample annealing Fe atoms tend to migrate deeper in to the bulk, which can be the reason for a lower amount of Fe in the FeSe 3 TL film, especially in the bottom layer. This hypothesis speaks in favor of Fe vacancies. The photoemission data, provided by my colleagues, Martin Ellguth and Christian Tusche, also has an indication of the Fe vacancies, see Fig. 7.15, due to the size of a spot at the Γ -point.

The photoemission image of Fig. 7.15(c) should reveal twelve features from three different domains of FeSe on Bi₂Se₃ (four features from each domain) at the position of the M-points (indicated by the dashed purple circle). However, due to the low signal-to-noise ratio I can barely see only four regions with a slightly increased photoemission signal, indicated by dark and light blue dashed circles. Only the feature at the Γ -point is clearly visible. If we compare the size of this feature with the sizes of the hole pockets presented at the Γ -points of the calculated images (a) and (b), we can clearly see that the size of the photoemission feature is slightly bigger than the size of the hole pocket in (a). Thus, I may speculate that the FeSe nanostructures, prepared in our work, have Fe vacancies. The amount of Fe vacancies is approximately the same as in the calculations presented in Fig. 7.14, which considered that $\approx 5\%$ of the Fe atoms are missing. I conclude that the concentration of Fe vacancies is approximately $0.6 \times 10^{21} \text{ cm}^{-3}$.

Thus I assume that the FeSe nanostructures, presented in my thesis, can be described by the electronic band structure presented in Fig. 7.14 (c), which corresponds to n-doping, caused by Fe vacancies. This compares favorably with the photoemission results on the FeSe films on STO [133, 186], which was also shown to be n-doped. The hole pocket at the Γ -point was also shown to be weak or even absent [133, 187].

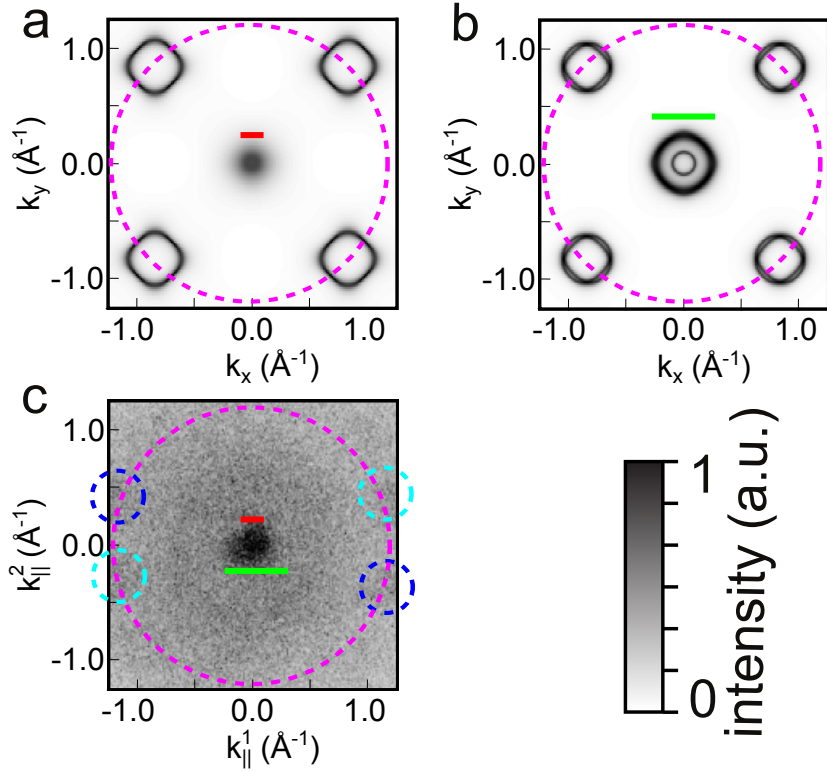


Figure 7.15: Calculated Fermi surfaces of pristine FeSe (a) and FeSe with Fe vacancies (b). (c) Experimental k_{\parallel} -resolved photoemission of FeSe on Bi_2Se_3 probing initial states at E_F with the He-I line ($h\nu = 21.2$ eV, unpolarized radiation). We cannot expect that the directions of the FeSe growth coincide with x and y axes of the theoretical calculations. This is why the position of the M-points is indicated only by dashed purple circles. The red line in (a) and (c) indicates the size of the Γ -point pocket in (a). The green line in (b) and (c) indicates the size of the Γ -point pocket in (b). The dark and light blue dashed circles indicate shallow features at the M-points of two different FeSe domains.

Such tendencies were usually observed in different materials based on FeSe, when an increased critical temperature was observed [187]. We may conclude, that the observed photoemission data are in agreement with the presented STS spectra (see Fig. 7.13(a)), and that the SC gap indicates a high critical temperature.

The theory, which was recently employed to explain high T_c of FeSe on STO, was discussed in chapter 2 [132]. It tells us that electrons interact with each other inside the relatively large electron pockets at the M-points via phonons, and, in the same process, they interact also with electrons from the band which is presented by a small hole pocket at the Fermi level or even stays beneath it at the Γ -point. The interband interaction is provided by spin fluctuations. These two different interactions lead to SC. This theory also concludes that an energy shift of the band at the Γ -point beneath the Fermi level is proportional to the critical temperature.

On the base of this theory, we can speculate that Fe vacancies lead to n-doping. This electron doping moves the bands at the Γ and at the M-points down (relative to the Fermi level). This is why the hole pocket at the Γ -point is reduced, while the electron pockets at the M-points are increased, and this leads to the high T_c , confirmed by the SC gap observation in the STS results. However, a full theory on the critical conditions for FeSe on Bi_2Se_3 has not been established yet.

Chapter 8

Conclusion and Outlook

FeSe and Bi nanostructures on $\text{Bi}_2\text{Se}_3(0001)$ surface were investigated by low-temperature STM with complementary AES and LEED experiments. This investigation was done in close connection with ARPES, XAFS, x-ray diffraction and theoretical studies. The physical implications of this work are based on the complimentary techniques and theory to elucidate the rich physical phenomena of these systems.

The starting point of this thesis is the preparation and study of the $\text{Bi}_2\text{Se}_3(0001)$ surface. Cleavage is a usual technique for the Bi_2Se_3 surface preparation [16–18]. However, it is impossible to use with thin crystals and epitaxial films. Cleavage also can lead to a lot of wasted material. *In situ* cleavage is a demanding process in respect of time and cleavage preparation. Thus an ion bombardment (sputtering) and subsequent annealing process was developed.

The results show that Ar-ion bombardment (energy: ≈ 1.5 keV, sample current density: $j \approx 0.1 \mu\text{A}/\text{mm}^2$, for 15 min) with annealing at 670–690 K for one hour lead to atomically flat surfaces with a coherent structure.

STM also shows us that the Bi_2Se_3 surface prepared by this method has the same surface unit cell shape and size as the surface unit cell of the *in situ* cleaved Bi_2Se_3 crystal. *In situ* cleavage was also done during this work with specially designed cleavage stages, and the cleaved surfaces were used as a reference for the calibration of the scanners in the STM study.

Also, STS and photoemission measurements show features, which are attributed to the so-called topologically protected Dirac cone surface state, with the Dirac point at -0.3 eV. This is an indication of the pristine surface of the 3D topological insulator (TI).

So I can clearly answer the question, which was raised in the beginning of my work. The $\text{Bi}_2\text{Se}_3(0001)$ surface can be prepared by sputtering and annealing at 670–690 K, and it compares favorably with the *in situ* cleaved Bi_2Se_3 surface. Due to this result, the prepared Bi_2Se_3 samples are promising substrates for future work on the combination of 3D TI with SCs and magnetic materials.

An important finding of my study is that an increased annealing temperature above 670–690 K leads to the destruction of the surface due to the evaporation of Bi_2Se_3 . A low annealing temperature (< 620 K) leads to the formation of a subsurface dislocation network, which is ascribed to preferential Se sputtering.

The clean $\text{Bi}_2\text{Se}_3(0001)$ surface was used for the preparation of FeSe and Bi nanostructures. The FeSe nanocrystals were grown by iron deposition with subsequent annealing. The combined application of the complementary techniques (surface X-ray diffraction, LEED) and STM clarifies the atomic structure of the FeSe

nanoislands. The presented results show that FeSe forms embedded nanoislands with an average height of three TL. The height of one TL on the Bi₂Se₃ surface is approximately 5.74 Å. This indicates an expansion of the crystal lattice along the vertical direction by 4.2 %. The lateral size of the islands is from few tens to 100–200 nm. FeSe on Bi₂Se₃ gives rise to a Moiré stripe pattern in the surface corrugation. The analysis of this pattern allows to determine the lateral crystal constants. FeSe has a reduced (compared to bulk) orthorhombic symmetry, with the surface lattice constants $a = 3.77 \pm 0.02$ Å and $b = 3.85 \pm 0.04$ Å (2 % expansion along b direction). Thus, the second question raised in the beginning of my thesis is answered. Epitaxial FeSe can be prepared on the Bi₂Se₃ surface with no additional source of Se. The atomic structure of the obtained FeSe nanostructures is quantitatively determined.

FeSe is a candidate for iron-based unconventional superconductors. The STS measurements show a gap-like feature, which can be ascribed to a SC gap. The size of the gap is 44 meV, which corresponds to the critical temperature as high as 90 K. However, the possible critical temperature and the critical field stay out of reach for the STM used here. Potential FeSe SC is comparable to the results obtained on FeSe films on STO substrates [22, 23]. With insights from theory and photoemission results, we can speculate that a high critical temperature can be the result of Fe vacancies and their influence on the FeSe electronic bands. Theory shows that Fe vacancies affect the band structure in such a way that on the Fermi surface we can see a reduction of the number of states around the Γ -point and an enlargement of the number of states around the M-points. Similar electronic structure difference from the pristine bulk FeSe band structure are features of other SC materials, which are based on FeSe and also shows an increased critical temperature (in comparison with the bulk pristine FeSe crystal) [132, 187–190].

A possible general theoretical explanation for the high critical temperature in FeSe compounds has been discussed [132]. This explanation includes an interband spin fluctuation driven electron interaction in combination with an intraband phonon driven interaction. The result of this article [132] tells that a down shift of the band, which corresponds to the reduction of the number of states around the Γ -point at the Fermi level, can lead to a stronger electron pairing and thus to an increased critical temperature. However, further theoretical insight into the critical temperature of FeSe on Bi₂Se₃ is needed.

So I cannot clearly answer the question if the FeSe nanostructures on the Bi₂Se₃ surface are an example of a high T_c unconventional SC. But this thesis provides new insights into this topic.

Bi bilayer (BL) were prepared by an atomic hydrogen exposure of the Bi₂Se₃(0001) surface. The formation of Bi BL is explained by the chemical etching of Se. The STM images show atomically flat surfaces of Bi BL, which covers the Bi₂Se₃ surface almost fully. A minor amount of holes and second Bi BL is observed. The first STS measurements of Bi BL on the Bi₂Se₃ surface are presented. They show a peak in dI/dV signal at positive sample bias voltages, which shifts from 0.2 to 0.28 V in proximity of defects. Also the dip in differential conductance at -0.2 V allows to speculate that during the preparation we also tune the position of the Bi₂Se₃ surface state Dirac point. Further experiments and theoretical studies are needed to clarify these findings.

In view of the results presented in this thesis, it would be interesting to continue

the studies of the FeSe nanocrystals on the Bi₂Se₃ surface. Further theory work can make a connection between electronic structure and the critical temperature. Also, temperature and magnetic field dependent STS would scrutinize our speculation on parameters of the FeSe SC state.

A fascinating extension would be STM research on a proximity effect of SC on the surface of the 3D TI Bi₂Se₃. This demanding task is tremendously interesting due to a possibility to create Majorana bound states [12, 13], which are extremely important for the quantum computation [25].

Bi BL offer the possibility for work on the preparation of MnBi. This compound is a candidate for showing non-collinear spin textures in the form of skyrmions [30]. Spin-STM in magnetic fields can contribute to the analysis of these magnetic structures. Thus it would be interesting to study skyrmions on the surface of a 3D TI, because it was shown that this combination can lead to a better control of skyrmion parameters [11].

The new preparation chamber, which was installed during my work, in the combination with the low-temperature STM is an excellent instrument to pursue future research in the field of topological insulators in connection with superconductivity and non-collinear spin textures.

Bibliography

- [1] Joel E. Moore. In: *Nature* 464 (2010), pp. 194–198.
- [2] M. Z. Hasan and C. L. Kane. In: *Rev. Mod. Phys.* 82 (4 2010), pp. 3045–3067. DOI: 10.1103/RevModPhys.82.3045.
- [3] Charles L. Kane. In: *Nat Phys* 4 (2008), pp. 348–349.
- [4] Walter Kohn. In: *Phys. Rev.* 133 (1A 1964), A171–A181. DOI: 10.1103/PhysRev.133.A171.
- [5] K. v. Klitzing, G. Dorda, and M. Pepper. In: *Phys. Rev. Lett.* 45 (6 1980), pp. 494–497. DOI: 10.1103/PhysRevLett.45.494.
- [6] J.E. Avron, D. Oscadchy, and R. Seiler. In: *Physics Today* (2003), pp. 38–42.
- [7] C. Pauly. *Strong and Weak Topology Probed by Surface Science: Topological Insulator Properties of Phase Change Alloys and Heavy Metal Graphene*. MatWerk. Springer Fachmedien Wiesbaden, 2016.
- [8] M. Franz and L. Molenkamp. *Topological Insulators*. Contemporary Concepts of Condensed Matter Science. Elsevier Science, 2013.
- [9] T. Schäpers. *Semiconductor Spintronics*. De Gruyter Textbook. De Gruyter, 2016.
- [10] Jiannis K Pachos and Steven H Simon. In: *New Journal of Physics* 16.6 (2014), p. 065003.
- [11] Hilary M. Hurst, Dmitry K. Efimkin, Jiadong Zang, and Victor Galitski. In: *Phys. Rev. B* 91 (6 2015), p. 060401. DOI: 10.1103/PhysRevB.91.060401.
- [12] L. Fu and C.L. Kane. In: *Phys. Rev. Lett.* 100 (2008), p. 096407. DOI: 10.1103/PhysRevLett.100.096407.
- [13] Liang Fu and C. L. Kane. In: *Phys. Rev. B* 79 (16 2009), p. 161408. DOI: 10.1103/PhysRevB.79.161408.
- [14] Haijun Zhang, Chao-Xing Liu, Xiao-Liang Qi, Xi Dai, Zhong Fang, and Shou-Cheng Zhang. In: *Nat Phys* 5.6 (2009), pp. 438–442. DOI: 10.1038/nphys1270.
- [15] Lin Miao, Z. F. Wang, Wenmei Ming, Meng-Yu Yao, Meixiao Wang, Fang Yang, Y. R. Song, Fengfeng Zhu, Alexei V. Fedorov, Z. Sun, C. L. Gao, Canhua Liu, Qi-Kun Xue, Chao-Xing Liu, Feng Liu, Dong Qian, and Jin-Feng Jia. In: *Proceedings of the National Academy of Sciences* 110.8 (2013), pp. 2758–2762. DOI: 10.1073/pnas.1218104110. eprint: <http://www.pnas.org/content/110/8/2758.full.pdf>.
- [16] S. Urazhdin, D. Bilc, S. H. Tessmer, S. D. Mahanti, Theodora Kyratsi, and M. G. Kanatzidis. In: *Phys. Rev. B* 66 (2002), p. 161306. DOI: 10.1103/PhysRevB.66.161306.

- [17] Sunghun Kim, M. Ye, K. Kuroda, Y. Yamada, E. E. Krasovskii, E. V. Chulkov, K. Miyamoto, M. Nakatake, T. Okuda, Y. Ueda, K. Shimada, H. Namatame, M. Taniguchi, and A. Kimura. In: *Phys. Rev. Lett.* 107 (2011), p. 056803. DOI: 10.1103/PhysRevLett.107.056803.
- [18] Y. S. Hor, A. Richardella, P. Roushan, Y. Xia, J. G. Checkelsky, A. Yazdani, M. Z. Hasan, N. P. Ong, and R. J. Cava. In: *Phys. Rev. B* 79 (2009), p. 195208. DOI: 10.1103/PhysRevB.79.195208.
- [19] Sumalay Roy, H.L. Meyerheim, A. Ernst, K. Mohseni, C. Tusche, M.G. Vergniory, T.V. Menshchikova, M.M. Otrokov, A.G. Ryabishchenkova, Z.S. Aliev, M.B. Babanly, K.A. Kokh, O.E. Tereshchenko, E.V. Chulkov, J. Schneider, and J. Kirschner. In: *Phys. Rev. Lett.* 113 (2014), p. 116802. DOI: 10.1103/PhysRevLett.113.116802.
- [20] Johnpierre Paglione and Richard L. Greene. In: *Nat Phys* 6.9 (2010), pp. 645–658. ISSN: 1745-2473. DOI: 10.1038/nphys1759.
- [21] Hideo Hosono and Kazuhiko Kuroki. In: *Physica C: Superconductivity and its Applications* 514 (2015). Superconducting Materials: Conventional, Unconventional and Undetermined, pp. 399–422. ISSN: 0921-4534. DOI: <http://dx.doi.org/10.1016/j.physc.2015.02.020>.
- [22] Wang Qing-Yan, Li Zhi, Zhang Wen-Hao, Zhang Zuo-Cheng, Zhang Jin-Song, Li Wei, Ding Hao, Ou Yun-Bo, Deng Peng, Chang Kai, Wen Jing, Song Can-Li, He Ke, Jia Jin-Feng, Ji Shuai-Hua, Wang Ya-Yu, Wang Li-Li, Chen Xi, Ma Xu-Cun, and Xue Qi-Kun. In: *Chinese Physics Letters* 29.3 (2012), p. 037402.
- [23] Jian-Feng Ge, Zhi-Long Liu, Canhua Liu, Chun-Lei Gao, Dong Qian, Qi-Kun Xue, Ying Liu, and Jin-Feng Jia. In: *Nat Mater* 14.3 (2015). Letter, pp. 285–289. ISSN: 1476-1122.
- [24] Fong-Chi Hsu, Jiu-Yong Luo, Kuo-Wei Yeh, Ta-Kun Chen, Tzu-Wen Huang, Phillip M. Wu, Yong-Chi Lee, Yi-Lin Huang, Yan-Yi Chu, Der-Chung Yan, and Maw-Kuen Wu. In: *Proceedings of the National Academy of Sciences* 105.38 (2008), pp. 14262–14264. DOI: 10.1073/pnas.0807325105.
- [25] Sankar Das Sarma, Michael Freedman, and Chetan Nayak. In: *Npj Quantum Information* 1 (2015). Review Article, 15001 EP –.
- [26] Frank Wilczek. In: *Nat Phys* 5.9 (2009), pp. 614–618. ISSN: 1745-2473. DOI: 10.1038/nphys1380.
- [27] Dongchao Wang, Li Chen, Hongmei Liu, and Xiaoli Wang. In: *Journal of the Physical Society of Japan* 82.9 (2013), p. 094712. DOI: 10.7566/JPSJ.82.094712. eprint: <http://dx.doi.org/10.7566/JPSJ.82.094712>.
- [28] Zheng Liu, Chao-Xing Liu, Yong-Shi Wu, Wen-Hui Duan, Feng Liu, and Jian Wu. In: *Phys. Rev. Lett.* 107 (13 2011), p. 136805. DOI: 10.1103/PhysRevLett.107.136805.
- [29] Li Chen, Z. F. Wang, and Feng Liu. In: *Phys. Rev. B* 87 (23 2013), p. 235420. DOI: 10.1103/PhysRevB.87.235420.
- [30] Michael A. McGuire, Huibo Cao, Bryan C. Chakoumakos, and Brian C. Sales. In: *Phys. Rev. B* 90 (17 2014), p. 174425. DOI: 10.1103/PhysRevB.90.174425.
- [31] Roozbeh Shokri, Holger L. Meyerheim, Sumalay Roy, Katayoon Mohseni, A. Ernst, M. M. Otrokov, E. V. Chulkov, and J. Kirschner. In: *Phys. Rev. B* 91 (20 2015), p. 205430. DOI: 10.1103/PhysRevB.91.205430.

- [32] J. A. Hoerni. In: *U. S. Patent 3,025,589*. (1959).
- [33] George E. Anner. “Planar Processing Primer”. In: Dordrecht: Springer Netherlands, 1990. Chap. Planar Processing and Basic Devices, pp. 1–37. DOI: 10.1007/978-94-009-0441-5_1.
- [34] G. Binnig, H. Rohrer, Ch. Gerber, and E. Weibel. In: *Phys. Rev. Lett.* 49 (1 1982), pp. 57–61. DOI: 10.1103/PhysRevLett.49.57.
- [35] G. Binnig, H. Rohrer, Ch. Gerber, and E. Weibel. In: *Phys. Rev. Lett.* 50 (2 1983), pp. 120–123. DOI: 10.1103/PhysRevLett.50.120.
- [36] Gerd Binnig and Heinrich Rohrer. In: *Rev. Mod. Phys.* 59 (3 1987), pp. 615–625. DOI: 10.1103/RevModPhys.59.615.
- [37] W.J. Kaiser and R.C. Jaklevic. In: *IBM Journal of Research and Development* 30.4 (1986), pp. 411–416. ISSN: 0018-8646. DOI: 10.1147/rd.304.0411.
- [38] J. Tersoff and D. R. Hamann. In: *Phys. Rev. B* 31 (2 1985), pp. 805–813. DOI: 10.1103/PhysRevB.31.805.
- [39] S. Ouazi, S. Wedekind, G. Rodary, H. Oka, D. Sander, and J. Kirschner. In: *Phys. Rev. Lett.* 108 (10 2012), p. 107206. DOI: 10.1103/PhysRevLett.108.107206.
- [40] S.-H. Phark, J. A. Fischer, M. Corbetta, D. Sander, K. Nakamura, and J. Kirschner. In: *Nature Communications* 5 (2014). Article, 5183 EP –.
- [41] C. J. Chen. *Introduction to scanning tunneling microscopy*. Ed. by Oxford. 2nd. Oxford University Press, 2008.
- [42] L. D. Landau and E. M. Lifschitz. “The transmission coefficient”. In: *Quantum Mechanics: Non-relativistic Theory. Course of Theoretical Physics*. London: Pergamon Press, 1977, pp. 76–81.
- [43] R. Landauer. In: *IBM Journal of Research and Development* 1.3 (1957), pp. 223–231. ISSN: 0018-8646. DOI: 10.1147/rd.13.0223.
- [44] H. Ohnishi, Y. Kondo, and K. Takayanagi. In: *Nature* 395.6704 (1998), pp. 780–783. ISSN: 0028-0836. DOI: 10.1038/27399.
- [45] Nicols Agrat, Alfredo Levy Yeyati, and Jan M. van Ruitenbeek. In: *Physics Reports* 377.23 (2003), pp. 81 –279. ISSN: 0370-1573. DOI: [http://dx.doi.org/10.1016/S0370-1573\(02\)00633-6](http://dx.doi.org/10.1016/S0370-1573(02)00633-6).
- [46] Ivar Giaever. In: *Phys. Rev. Lett.* 5 (10 1960), pp. 464–466. DOI: 10.1103/PhysRevLett.5.464.
- [47] James Nicol, Sidney Shapiro, and Paul H. Smith. In: *Phys. Rev. Lett.* 5 (10 1960), pp. 461–464. DOI: 10.1103/PhysRevLett.5.461.
- [48] J. Bardeen. In: *Phys. Rev. Lett.* 6 (2 1961), pp. 57–59. DOI: 10.1103/PhysRevLett.6.57.
- [49] J. Tersoff and D. R. Hamann. In: *Phys. Rev. Lett.* 50 (25 1983), pp. 1998–2001. DOI: 10.1103/PhysRevLett.50.1998.
- [50] J. Wintterlin, J. Wiechers, H. Brune, T. Gritsch, H. Höfer, and R. J. Behm. In: *Phys. Rev. Lett.* 62 (1 1989), pp. 59–62. DOI: 10.1103/PhysRevLett.62.59.
- [51] V. M. Hallmark, S. Chiang, J. F. Rabolt, J. D. Swalen, and R. J. Wilson. In: *Phys. Rev. Lett.* 59 (25 1987), pp. 2879–2882. DOI: 10.1103/PhysRevLett.59.2879.

- [52] J. E. Demuth, U. Koehler, and R. J. Hamers. In: *Journal of Microscopy* 152.2 (1988), pp. 299–316. ISSN: 1365-2818. DOI: 10.1111/j.1365-2818.1988.tb01391.x.
- [53] Shuhei Ohnishi and Masaru Tsukada. In: *Solid State Communications* 71.5 (1989), pp. 391–394. ISSN: 0038-1098. DOI: [http://dx.doi.org/10.1016/0038-1098\(89\)90777-1](http://dx.doi.org/10.1016/0038-1098(89)90777-1).
- [54] A. Baratoff. In: *Physica B+C* 127.1 (1984), pp. 143–150. ISSN: 0378-4363. DOI: [http://dx.doi.org/10.1016/S0378-4363\(84\)80022-4](http://dx.doi.org/10.1016/S0378-4363(84)80022-4).
- [55] C. Julian Chen. In: *Phys. Rev. Lett.* 65 (4 1990), pp. 448–451. DOI: 10.1103/PhysRevLett.65.448.
- [56] M. Büttiker, Y. Imry, R. Landauer, and S. Pinhas. In: *Phys. Rev. B* 31 (10 1985), pp. 6207–6215. DOI: 10.1103/PhysRevB.31.6207.
- [57] M. Büttiker. In: *Phys. Rev. Lett.* 57 (14 1986), pp. 1761–1764. DOI: 10.1103/PhysRevLett.57.1761.
- [58] J. Cerdá, M. A. Van Hove, P. Sautet, and M. Salmeron. In: *Phys. Rev. B* 56 (24 1997), pp. 15885–15899. DOI: 10.1103/PhysRevB.56.15885.
- [59] Kamal K. Saha, Jürgen Henk, Arthur Ernst, and Patrick Bruno. In: *Phys. Rev. B* 77 (8 2008), p. 085427. DOI: 10.1103/PhysRevB.77.085427.
- [60] J. Enkovaara, D. Wortmann, and S. Blügel. In: *Phys. Rev. B* 76 (5 2007), p. 054437. DOI: 10.1103/PhysRevB.76.054437.
- [61] C. Bai. *Scanning tunneling microscopy and its applications*. Ed. by Berlin Springer. Springer series in surface sciences, 2000.
- [62] D. A. Bonnell. *Scanning probe microscopy and spectroscopy. Theory, techniques, and applications*. Ed. by NY New York. 2. edition. Wiley-VCH, 2001.
- [63] R. Wiesendanger. *Theory of STM and Related Scanning Probe Methods*. Ed. by Berlin Springer. 2. edition. Springer Series in Surface Sciences, 1996.
- [64] Joel Moore. In: *Nat Phys* 5.6 (2009), pp. 378–380. ISSN: 1745-2473. DOI: 10.1038/nphys1294.
- [65] Xiao-Liang Qi and Shou-Cheng Zhang. In: *Rev. Mod. Phys.* 83 (4 2011), pp. 1057–1110. DOI: 10.1103/RevModPhys.83.1057.
- [66] T.W. Gamelin and R.E. Greene. *Introduction to Topology*. Dover books on mathematics. Dover Publications, 1983.
- [67] S. K. Mishra, S. Satpathy, and O. Jepsen. In: *Journal of Physics: Condensed Matter* 9.2 (1997), p. 461.
- [68] Balazs L. Gyorffy. In: *Molecular Physics* 109.7-10 (2011), pp. 1403–1412. DOI: 10.1080/00268976.2011.565288. eprint: <http://dx.doi.org/10.1080/00268976.2011.565288>.
- [69] A. Aharoni. *Introduction to the Theory of Ferromagnetism*. International Series of Monographs on Physics. Clarendon Press, 2000, pp. 63–66.
- [70] Tomas Jungwirth, Jorg Wunderlich, and Kamil Olejnik. In: *Nat Mater* 11.5 (2012), pp. 382–390. ISSN: 1476-1122. DOI: 10.1038/nmat3279.
- [71] L. D. Landau and E. M. Lifschitz. “Motion in a uniform magnetic field”. In: *Quantum Mechanics: Non-relativistic Theory. Course of Theoretical Physics*. London: Pergamon Press, 1977, pp. 458–463.

- [72] Walter Kohn. In: *Phys. Rev.* 133 (1A 1964), A171–A181. DOI: 10.1103/PhysRev.133.A171.
- [73] D. J. Thouless, M. Kohmoto, M. P. Nightingale, and M. den Nijs. In: *Phys. Rev. Lett.* 49 (6 1982), pp. 405–408. DOI: 10.1103/PhysRevLett.49.405.
- [74] F. D. M. Haldane. In: *Phys. Rev. Lett.* 93 (20 2004), p. 206602. DOI: 10.1103/PhysRevLett.93.206602.
- [75] Y. K. Kato, R. C. Myers, A. C. Gossard, and D. D. Awschalom. In: *Science* 306.5703 (2004), pp. 1910–1913. ISSN: 0036-8075. DOI: 10.1126/science.1105514. eprint: <http://science.sciencemag.org/content/306/5703/1910.full.pdf>.
- [76] Jairo Sinova, Dimitrie Culcer, Q. Niu, N. A. Sinitsyn, T. Jungwirth, and A. H. MacDonald. In: *Phys. Rev. Lett.* 92 (12 2004), p. 126603. DOI: 10.1103/PhysRevLett.92.126603.
- [77] C. L. Kane and E. J. Mele. In: *Phys. Rev. Lett.* 95 (22 2005), p. 226801. DOI: 10.1103/PhysRevLett.95.226801.
- [78] C. L. Kane and E. J. Mele. In: *Phys. Rev. Lett.* 95 (14 2005), p. 146802. DOI: 10.1103/PhysRevLett.95.146802.
- [79] A13ean. *Topological insulator band structure.svg*. used under CC BY / position of Fermi level was changed. URL: https://commons.wikimedia.org/wiki/File:Topological_insulator_band_structure.svg.
- [80] C. Brüne, H. Buhmann, and L.W. Molenkamp. *Topological Insulators: Chapter 5. Quantum Spin Hall State in HgTe*. Contemporary Concepts of Condensed Matter Science. Elsevier Science, 2013.
- [81] B.A. Bernevig and T.L. Hughes. *Topological Insulators and Topological Superconductors*. Princeton University Press, 2013.
- [82] Ilya K. Drozdov, A. Alexandradinata, Sangjun Jeon, Stevan Nadj-Perge, Huiwen Ji, R. J. Cava, B. Andrei Bernevig, and Ali Yazdani. In: *Nat Phys* 10.9 (2014). Article, pp. 664–669. ISSN: 1745-2473.
- [83] Sung Hwan Kim, Kyung-Hwan Jin, Joonbum Park, Jun Sung Kim, Seung-Hoon Jhi, Tae-Hwan Kim, and Han Woong Yeom. In: *Phys. Rev. B* 89 (15 2014), p. 155436. DOI: 10.1103/PhysRevB.89.155436.
- [84] Fang Yang, Lin Miao, Z. F. Wang, Meng-Yu Yao, Fengfeng Zhu, Y. R. Song, Mei-Xiao Wang, Jin-Peng Xu, Alexei V. Fedorov, Z. Sun, G. B. Zhang, Canhua Liu, Feng Liu, Dong Qian, C. L. Gao, and Jin-Feng Jia. In: *Phys. Rev. Lett.* 109 (1 2012), p. 016801. DOI: 10.1103/PhysRevLett.109.016801.
- [85] Z. F. Wang, Meng-Yu Yao, Wenmei Ming, Lin Miao, Fengfeng Zhu, Canhua Liu, C. L. Gao, Dong Qian, Jin-Feng Jia, and Feng Liu. In: *Nat Commun* 4 (2013), p. 1384. DOI: 10.1038/ncomms2387.
- [86] K. Govaerts, K. Park, C. De Beule, B. Partoens, and D. Lamoen. In: *Phys. Rev. B* 90 (15 2014), p. 155124. DOI: 10.1103/PhysRevB.90.155124.
- [87] Wenbin Qiu, Zongqing Ma, Yongchang Liu, Mohammed Shahriar Al Hossain, Xiaolin Wang, Chuanbing Cai, and Shi Xue Dou. In: *ACS Applied Materials & Interfaces* 8.12 (2016). PMID: 26955971, pp. 7891–7896. DOI: 10.1021/acsami.6b00574. eprint: <http://dx.doi.org/10.1021/acsami.6b00574>.
- [88] Can-Li Song, Yi-Lin Wang, Ye-Ping Jiang, Zhi Li, Lili Wang, Ke He, Xi Chen, Xu-Cun Ma, and Qi-Kun Xue. In: *Phys. Rev. B* 84 (2 2011), p. 020503. DOI: 10.1103/PhysRevB.84.020503.

- [89] J. Bardeen, L. N. Cooper, and J. R. Schrieffer. In: *Phys. Rev.* 108 (5 1957), pp. 1175–1204. DOI: 10.1103/PhysRev.108.1175.
- [90] J.F. Annett. *Superconductivity, Superfluids and Condensates*. Oxford Master Series in Physics. OUP Oxford, 2004.
- [91] T.P. Orlando and K.A. Delin. *Foundations of Applied Superconductivity*. Electrical Engineering Series. Addison-Wesley, 1991.
- [92] M. Tinkham. *Introduction to Superconductivity: Second Edition*. Dover Books on Physics. Dover Publications, 2004.
- [93] Y. Kobayashi, T. Imai, and T. Sakakibara. “Phenomenological description of ”coherence peak” of high- T_c superconductors by improved three-fluid model”. In: *Microwave Conference, 1993. 23rd European*. 1993, pp. 596–599. DOI: 10.1109/EUMA.1993.336639.
- [94] C.K. Poole, H.A. Farach, and R.J. Creswick. *Handbook of Superconductivity*. Elsevier Science, 1999.
- [95] C.-L. Song, Y.-L. Wang, P. Cheng, Y.P. Jiang, E. Li, T. Zhang, Z. Li, K. He, L. Wang, J.-F. Jia, H.-H. Hung, C. Wu, X. Ma, and Q.-K. Chen X.and Xue. In: *Science* 332 (2011), p. 1410. DOI: 10.1126/science.1202226.
- [96] R.D. Parks. *Superconductivity: Part 1 (In Two Parts)*. Superconductivity. Taylor & Francis, 1969.
- [97] F. Steglich, J. Aarts, C. D. Bredl, W. Lieke, D. Meschede, W. Franz, and H. Schäfer. In: *Phys. Rev. Lett.* 43 (25 1979), pp. 1892–1896. DOI: 10.1103/PhysRevLett.43.1892.
- [98] J. G. Bednorz and K. A. Müller. In: *Zeitschrift für Physik B Condensed Matter* 64.2 (1986), pp. 189–193. ISSN: 1431-584X. DOI: 10.1007/BF01303701.
- [99] V.L. Ginzburg. In: *Physics Letters* 13.2 (1964), pp. 101–102. ISSN: 0031-9163. DOI: [http://dx.doi.org/10.1016/0031-9163\(64\)90672-9](http://dx.doi.org/10.1016/0031-9163(64)90672-9).
- [100] W. A. Little. In: *Phys. Rev.* 134 (6A 1964), A1416–A1424. DOI: 10.1103/PhysRev.134.A1416.
- [101] V. L. Ginzburg. In: *Soviet Physics Uspekhi* 34.4 (1991), p. 283.
- [102] A. P. Drozdov, M. I. Erements, I. A. Troyan, V. Ksenofontov, and S. I. Shylin. In: *Nature* 525.7567 (2015). Letter, pp. 73–76. ISSN: 0028-0836.
- [103] D. J. Scalapino, J. R. Schrieffer, and J. W. Wilkins. In: *Phys. Rev.* 148 (1 1966), pp. 263–279. DOI: 10.1103/PhysRev.148.263.
- [104] A. S. Alexandrov. In: *Journal of Physics: Conference Series* 286.1 (2011), p. 012012.
- [105] R. Lal and S. K. Joshi. In: *Phys. Rev. B* 45 (1 1992), pp. 361–369. DOI: 10.1103/PhysRevB.45.361.
- [106] T. Yoshida, S. Ideta, T. Shimojima, W. Malaeb, K. Shinada, H. Suzuki, I. Nishi, A. Fujimori, K. Ishizaka, S. Shin, Y. Nakashima, H. Anzai, M. Arita, A. Ino, H. Namatame, M. Taniguchi, H. Kumigashira, K. Ono, S. Kasahara, T. Shibauchi, T. Terashima, Y. Matsuda, M. Nakajima, S. Uchida, Y. Tomioka, T. Ito, K. Kihou, C. H. Lee, A. Iyo, H. Eisaki, H. Ikeda, R. Arita, T. Saito, S. Onari, and H. Kontani. In: *Sci Rep* 4 (2014). 25465027[pmid], p. 7292. ISSN: 2045-2322. DOI: 10.1038/srep07292.

- [107] D. J. Van Harlingen, I. E. Milliard, B. L T Plourde, and B. D. Yanoff. In: *Physica C: Superconductivity and its Applications* 317-318 (May 1999), pp. 410–420. ISSN: 0921-4534. DOI: 10.1016/S0921-4534(99)00088-X.
- [108] E. Kaldis, E. Liarokapis, and K.A. Müller. *High-Tc Superconductivity 1996: Ten Years after the Discovery*. Nato Science Series E: Springer Netherlands, 2012.
- [109] A.V. Narlikar. *Frontiers in Superconducting Materials*. Springer Berlin Heidelberg, 2005.
- [110] N. Plakida. *High-Temperature Cuprate Superconductors: Experiment, Theory, and Applications*. Springer Series in Solid-State Sciences. Springer Berlin Heidelberg, 2010.
- [111] J.R. Waldram. *Superconductivity of Metals and Cuprates*. Superconductivity of Metals and Cuprates. Taylor & Francis, 1996.
- [112] Evgenii G Maksimov. In: *Physics-Uspekhi* 43.10 (2000), p. 965.
- [113] A. Bill, V. Z. Kresin, and S. A. Wolf. “The Isotope Effect in Superconductors”. In: *Pair Correlations in Many-Fermion Systems*. Ed. by Vladimir Z. Kresin. Boston, MA: Springer US, 1998, pp. 25–55. DOI: 10.1007/978-1-4899-1555-9_2.
- [114] D. N. Basov and Andrey V. Chubukov. In: *Nat Phys* 7.4 (2011), pp. 272–276. ISSN: 1745-2473. DOI: 10.1038/nphys1975.
- [115] Yoichi Kamihara, Takumi Watanabe, Masahiro Hirano, and Hideo Hosono. In: *Journal of the American Chemical Society* 130.11 (2008). PMID: 18293989, pp. 3296–3297. DOI: 10.1021/ja800073m. eprint: <http://dx.doi.org/10.1021/ja800073m>.
- [116] W. L. Yang, A. P. Sorini, C-C. Chen, B. Moritz, W.-S. Lee, F. Vernay, P. Olalde-Velasco, J. D. Denlinger, B. Delley, J.-H. Chu, J. G. Analytis, I. R. Fisher, Z. A. Ren, J. Yang, W. Lu, Z. X. Zhao, J. van den Brink, Z. Hussain, Z.-X. Shen, and T. P. Devereaux. In: *Phys. Rev. B* 80 (1 2009), p. 014508. DOI: 10.1103/PhysRevB.80.014508.
- [117] X. J. Wu, D. Z. Shen, Z. Z. Zhang, J. Y. Zhang, K. W. Liu, B. H. Li, Y. M. Lu, B. Yao, D. X. Zhao, B. S. Li, C. X. Shan, X. W. Fan, H. J. Liu, and C. L. Yang. In: *Applied Physics Letters* 90.11, 112105 (2007). DOI: <http://dx.doi.org/10.1063/1.2712497>.
- [118] Yoshikazu Mizuguchi, Keita Deguchi, Shunsuke Tsuda, Takahide Yamaguchi, Hiroyuki Takeya, Hiroaki Kumakura, and Yoshihiko Takano. In: *Applied Physics Express* 2.8 (2009), p. 083004.
- [119] Jasmine N. Millican, Daniel Phelan, Evan L. Thomas, Juscelino B. Leo, and Elisabeth Carpenter. In: *Solid State Communications* 149.1718 (2009), pp. 707 –710. ISSN: 0038-1098. DOI: <http://dx.doi.org/10.1016/j.ssc.2009.02.011>.
- [120] D Braithwaite, B Salce, G Lapertot, F Bourdarot, C Marin, D Aoki, and M Hanfland. In: *Journal of Physics: Condensed Matter* 21.23 (2009), p. 232202.
- [121] A. Linscheid, S. Maiti, Y. Wang, S. Johnston, and P. J. Hirschfeld. *High T_c via spin fluctuations from incipient bands: application to monolayers and intercalates of FeSe*. 2016. eprint: [arXiv:1603.03739](https://arxiv.org/abs/1603.03739).
- [122] Xiao Chen, S. Maiti, A. Linscheid, and P. J. Hirschfeld. In: *Phys. Rev. B* 92 (22 2015), p. 224514. DOI: 10.1103/PhysRevB.92.224514.

- [123] F. Essenberger, P. Buczek, A. Ernst, L. Sandratskii, and E. K. U. Gross. In: *Phys. Rev. B* 86 (6 2012), p. 060412. DOI: 10.1103/PhysRevB.86.060412.
- [124] C.-T. Chen, C. C. Tsuei, M. B. Ketchen, Z.-A. Ren, and Z. X. Zhao. In: *Nat Phys* 6.4 (2010), pp. 260–264. ISSN: 1745-2473. DOI: 10.1038/nphys1531.
- [125] H. Ding, P. Richard, K. Nakayama, K. Sugawara, T. Arakane, Y. Sekiba, A. Takayama, S. Souma, T. Sato, T. Takahashi, Z. Wang, X. Dai, Z. Fang, G. F. Chen, J. L. Luo, and N. L. Wang. In: *EPL (Europhysics Letters)* 83.4 (2008), p. 47001.
- [126] I.I. Mazin and J. Schmalian. In: *Physica C: Superconductivity* 469.912 (2009). Superconductivity in Iron-Pnictides, pp. 614–627. ISSN: 0921-4534. DOI: <http://dx.doi.org/10.1016/j.physc.2009.03.019>.
- [127] F. Essenberger, A. Sanna, P. Buczek, A. Ernst, L. Sandratskii, and E. K. U. Gross. In: *Phys. Rev. B* 94 (1 2016), p. 014503. DOI: 10.1103/PhysRevB.94.014503.
- [128] Q. Fan, W. H. Zhang, X. Liu, Y. J. Yan, M. Q. Ren, R. Peng, H. C. Xu, B. P. Xie, J. P. Hu, T. Zhang, and D. L. Feng. In: *Nat Phys* 11.11 (2015). Article, pp. 946–952. ISSN: 1745-2473.
- [129] Yuko Senga and Hiroshi Kontani. In: *New Journal of Physics* 11.3 (2009), p. 035005.
- [130] X. Chen, V. Mishra, S. Maiti, and P.J. Hirschfeld. In: *ArXiv e-prints* (2016). eprint: 1606.00501.
- [131] I.I. Mazin. In: *Nature* 464.7286 (2010), pp. 183–186. ISSN: 0028-0836. DOI: 10.1038/nature08914.
- [132] Xiao Chen, S. Maiti, A. Linscheid, and P. J. Hirschfeld. In: *Phys. Rev. B* 92 (22 2015), p. 224514. DOI: 10.1103/PhysRevB.92.224514.
- [133] Y. Fang, D. H. Xie, W. Zhang, F. Chen, W. Feng, B. P. Xie, D. L. Feng, X. C. Lai, and S. Y. Tan. In: *Phys. Rev. B* 93 (18 2016), p. 184503. DOI: 10.1103/PhysRevB.93.184503.
- [134] M.Y. Kagan. *Modern trends in Superconductivity and Superfluidity*. Lecture Notes in Physics. Springer Netherlands, 2013.
- [135] Hai-Yuan Cao, Shiyong Tan, Hongjun Xiang, D. L. Feng, and Xin-Gao Gong. In: *Phys. Rev. B* 89 (1 2014), p. 014501. DOI: 10.1103/PhysRevB.89.014501.
- [136] I. I. Mazin. In: *Nat Mater* 14.8 (2015). News and Views, pp. 755–756. ISSN: 1476-1122.
- [137] Hans J. Hug, B. Stiefel, P. J. A. van Schendel, A. Moser, S. Martin, and H.-J. Gntherodt. In: *Review of Scientific Instruments* 70.9 (1999), pp. 3625–3640. DOI: <http://dx.doi.org/10.1063/1.1149970>.
- [138] *Temperature Measurement and Control Catalogue*. Lake Shore Cryogenics, Inc., 2004.
- [139] Inc. Lake Shore Cryotronics. *Model 340 Cryogenic Temperature Controller*. 2016. URL: <http://www.lakeshore.com/products/Cryogenic-Temperature-Controllers/Model-340/pages/Overview.aspx>.
- [140] Sebastian Wedekind. “A spin-polarized scanning tunneling microscopy and spectroscopy study of individual nanoscale particles grown on copper surfaces”. MA thesis. Halle, Univ., Naturwissenschaftliche Fakultt II, 2009.

- [141] Marco Corbetta. “Spin-polarized Scanning Tunneling Microscopy and Spectroscopy Study of Fe and Co Nanostructures on Cu(111)”. MA thesis. Halle, Univ., Naturwissenschaftliche Fakultt II, 2013.
- [142] Øystein Fischer, Martin Kugler, Ivan Maggio-Aprile, Christophe Berthod, and Christoph Renner. In: *Rev. Mod. Phys.* 79 (1 2007), pp. 353–419. DOI: 10.1103/RevModPhys.79.353.
- [143] *Polytec PT: Graphitgefüllt, bis 2980C*. URL: <http://www.polytec-pt.com>.
- [144] *Pyrometer IMPAC IP 140*. URL: <http://www.lumasenseinc.com>.
- [145] M. Bode. In: *Rep. Prog. Phys.* 66 (2003), p. 523.
- [146] R. Wiesendanger, H.-J. Güntherodt, G. Güntherodt, R. J. Gambino, and R. Ruf. In: *Phys. Rev. Lett.* 65 (2 1990), pp. 247–250. DOI: 10.1103/PhysRevLett.65.247.
- [147] Roland Wiesendanger. In: *Rev. Mod. Phys.* 81 (4 2009), pp. 1495–1550. DOI: 10.1103/RevModPhys.81.1495.
- [148] Richard P. Gunawardane and Christopher R. Arumainayagam. “AUGER ELECTRON SPECTROSCOPY”. In: *Handbook of Applied Solid State Spectroscopy*. Ed. by R. D. Vij. Boston, MA: Springer US, 2006, pp. 451–483. DOI: 10.1007/0-387-37590-2_10.
- [149] T.E. Gallon and J.A.D. Matthew. In: *Review of Physics in Technology* 3.1 (1972), p. 31.
- [150] F. Jona, J. A. Strozier Jr., and W. S. Yang. In: *Reports on Progress in Physics* 45.5 (1982), p. 527.
- [151] M. Prutton. In: *Journal of Applied Crystallography* 8.3 (1975), pp. 403–404. DOI: 10.1107/S0021889875010886.
- [152] Laboratory for Surface Physics and Electron Spectroscopies at Boston University. *Topological Insulators Bi_2Se_3 / Bi_2Te_3* . 2014. URL: <http://physics.bu.edu/surflab/projects.html>.
- [153] Zhanybek Alpichshev, Rudro R. Biswas, Alexander V. Balatsky, J. G. Analytis, J.-H. Chu, I. R. Fisher, and A. Kapitulnik. In: *Phys. Rev. Lett.* 108 (20 2012), p. 206402. DOI: 10.1103/PhysRevLett.108.206402.
- [154] Alineason Materials, Technology, Design, and Concept. *Crystal Growth*. 2013. URL: <http://www.alineason.com/index.php/en/knowhow/crystal-growth>.
- [155] V. V. Atuchin, V. A. Golyashov, K. A. Kokh, I. V. Korolkov, A. S. Kozhukhov, V. N. Kruchinin, S. V. Makarenko, L. D. Pokrovsky, I. P. Prosvirin, K. N. Romanyuk, and O. E. Tereshchenko. In: *Crystal Growth & Design* 11.12 (2011), pp. 5507–5514. DOI: 10.1021/cg201163v. eprint: <http://dx.doi.org/10.1021/cg201163v>.
- [156] D. D. L. Chung. In: *Journal of Materials Science* 22.12 (1987), pp. 4190–4198.
- [157] PLANO GmbH. *G3939 Doppelseitig klebendes, leitfhiges Kohleband*. URL: <https://www.plano-em.de/katalog/rem-zubehoer/klebe-baender-tabs-aufkleber-bleche/#cid1890>.

- [158] Sumalay Roy, H. L. Meyerheim, K. Mohseni, A. Ernst, M.M. Otrokov, M.G. Vergniory, G. Mussler, J. Kampmeier, D. Grutzmacher, C. Tusche, J. Schneider, E.V. Chulkov, and J. Kirschner. In: *Phys. Rev. B* 90 (2014), p. 155456. DOI: 10.1103/PhysRevB.90.155456.
- [159] Chris Mann, Damien West, Ireneusz Miotkowski, Yong P. Chen, Shengbai Zhang, and Chih-Kang Shih. In: *Nat Commun* 4 (2013).
- [160] G. Garbarino, A. Sow, P. Lejay, A. Sulpice, P. Toulemonde, M. Mezouar, and M. Nez-Regueiro. In: *EPL (Europhysics Letters)* 86.2 (2009), p. 27001.
- [161] S. Margadonna, Y. Takabayashi, Y. Ohishi, Y. Mizuguchi, Y. Takano, T. Kagayama, T. Nakagawa, M. Takata, and K. Prassides. In: *Phys. Rev. B* 80 (6 2009), p. 064506. DOI: 10.1103/PhysRevB.80.064506.
- [162] T. M. McQueen, A. J. Williams, P. W. Stephens, J. Tao, Y. Zhu, V. Ksenofontov, F. Casper, C. Felser, and R. J. Cava. In: *Phys. Rev. Lett.* 103 (2009), p. 057002. DOI: 10.1103/PhysRevLett.103.057002.
- [163] Serena Margadonna, Yasuhiro Takabayashi, Martin T. McDonald, Karolina Kasperkiewicz, Yoshikazu Mizuguchi, Yoshihiko Takano, Andrew N. Fitch, Emmanuelle Suard, and Kosmas Prassides. In: *Chem. Commun.* (43 2008), pp. 5607–5609. DOI: 10.1039/B813076K.
- [164] Alberto Cavallin, Vasili Sevriuk, Kenia Novakoski Fischer, Sujit Manna, Safia Ouazi, Martin Ellguth, Christian Tusche, Holger L. Meyerheim, Dirk Sander, and Jürgen Kirschner. In: *Surface Science* 646 (2016). Surface science for heterogeneous catalysis, a special issue in Honour of Richard Lambert, pp. 72–82. ISSN: 0039-6028. DOI: <http://dx.doi.org/10.1016/j.susc.2015.09.001>.
- [165] E. Wang, H. Ding, A. V. Fedorov, W. Yao, Z. Li, Y.-F. Lv, K. Zhao, L.-G. Zhang, Z. Xu, J. Schneeloch, R. Zhong, S.-H. Ji, L. Wang, K. He, X. Ma, G. Gu, H. Yao, Q.-K. Xue, X. Chen, and S. Zhou. In: *Nat Phys* 9.10 (2013). Letter, pp. 621–625. ISSN: 1745-2473.
- [166] A. Polyakov, Holger L. Meyerheim, E. Daryl Crozier, R. A. Gordon, K. Mohseni, S. Roy, A. Ernst, M. G. Vergniory, X. Zubizarreta, M. M. Otrokov, E. V. Chulkov, and J. Kirschner. In: *Phys. Rev. B* 92 (4 2015), p. 045423. DOI: 10.1103/PhysRevB.92.045423.
- [167] Y. Wang, Y. Jiang, M. Chen, Z. Li, C. Song, L. Wang, K. He, X. Chen, X. Ma, and Q.-K. Xue. In: *J. Phys. Condens. Matter* 24 (2012), p. 475604. DOI: 10.1088/0953-8984/24/47/475604.
- [168] S. Chandra and A.K.M.A. Islam. In: *Physica C: Superconductivity* 470.22 (2010), pp. 2072–2075. ISSN: 0921-4534. DOI: 10.1016/j.physc.2010.10.001.
- [169] A. Eich, M. Michiardi, G. Bihlmayer, X.-G. Zhu, J.-L. Mi, Bo B. Iversen, R. Wiesendanger, Ph. Hofmann, A. A. Khajetoorians, and J. Wiebe. In: *Phys. Rev. B* 90 (15 2014), p. 155414. DOI: 10.1103/PhysRevB.90.155414.
- [170] T. Kuech. *Handbook of Crystal Growth: Thin Films and Epitaxy*. Handbook of Crystal Growth. Elsevier Science, 2014.
- [171] Gao Chun-Lei, Qian Dong, Liu Can-Hua, Jia Jin-Feng, and Liu Feng. In: *Chinese Physics B* 22.6 (2013), p. 067304.
- [172] M. Schmid, A. Biedermann, H. Stadler, and P. Varga. In: *Phys. Rev. Lett.* 69 (1992), pp. 925–928. DOI: 10.1103/PhysRevLett.69.925.

- [173] M. Schmid, A. Biedermann, H. Stadler, C. Slama, and P. Varga. In: *Applied Physics A* 55.5 (1992), pp. 468–475. DOI: 10.1007/BF00348334.
- [174] Jixia Dai, Wenbo Wang, Matthew Brahlek, Nikesh Koirala, Maryam Salehi, Seongshik Oh, and Weida Wu. In: *Nano Research* (2014), pp. 1–7. DOI: 10.1007/s12274-014-0607-8.
- [175] G. Dhanaraj, K. Byrappa, V. Prasad, and M. Dudley. *Springer Handbook of Crystal Growth*. Springer Handbook of Crystal Growth. Springer Berlin Heidelberg, 2010.
- [176] P. Larson, V. A. Greanya, W. C. Tonjes, Rong Liu, S. D. Mahanti, and C. G. Olson. In: *Phys. Rev. B* 65 (8 2002), p. 085108. DOI: 10.1103/PhysRevB.65.085108.
- [177] Y. Xia, D. Qian, D. Hsieh, L. Wray, A. Pal, H. Lin, A. Bansil, D. Grauer, Y. S. Hor, R. J. Cava, and M. Z. Hasan. In: *Nat Phys* 5.6 (2009), pp. 398–402. ISSN: 1745-2473. DOI: 10.1038/nphys1274.
- [178] L. Xue, P. Zhou, C. X. Zhang, C. Y. He, G. L. Hao, L. Z. Sun, and J. X. Zhong. In: *AIP Advances* 3.5 (2013), p. 052105. DOI: <http://dx.doi.org/10.1063/1.4804439>.
- [179] S. Urazhdin, D. Bilc, S. D. Mahanti, S. H. Tessmer, Theodora Kyratsi, and M. G. Kanatzidis. In: *Phys. Rev. B* 69 (2004), p. 085313. DOI: 10.1103/PhysRevB.69.085313.
- [180] Can-Li Song, Yi-Lin Wang, Ye-Ping Jiang, Zhi Li, Lili Wang, Ke He, Xi Chen, Xu-Cun Ma, and Qi-Kun Xue. In: *Phys. Rev. B* 84 (2 2011), p. 020503. DOI: 10.1103/PhysRevB.84.020503.
- [181] Wenhao Zhang, Zhi Li, Fangsen Li, Huimin Zhang, Junping Peng, Chenjia Tang, Qingyan Wang, Ke He, Xi Chen, Lili Wang, Xucun Ma, and Qi-Kun Xue. In: *Phys. Rev. B* 89 (2014), p. 060506. DOI: 10.1103/PhysRevB.89.060506.
- [182] Jian-Feng Ge, Zhi-Long Liu, Canhua Liu, Chun-Lei Gao, Dong Qian, Qi-Kun Xue, Ying Liu, and Jin-Feng Jia. In: *Nature Mater.* 14 (2014), p. 285. DOI: 10.1038/nmat4153.
- [183] K. Hermann and M.A. van Hove. URL: <http://www.fhi-berlin.mpg.de/KHsoftware/LEEDpat>.
- [184] S-H. Baek, D.V. Efremov, J.S. Ok J.M.and Kim, J. van den Brink, and B. Büchner. In: *Nature Mater.* 14 (2015), p. 210. DOI: 10.1038/nmat4138.
- [185] Tom Berlijn, Hai-Ping Cheng, P. J. Hirschfeld, and Wei Ku. In: *Phys. Rev. B* 89 (2 2014), p. 020501. DOI: 10.1103/PhysRevB.89.020501.
- [186] K. V. Shanavas and David J. Singh. In: *Phys. Rev. B* 92 (3 2015), p. 035144. DOI: 10.1103/PhysRevB.92.035144.
- [187] Shiyong Tan, Yan Zhang, Miao Xia, Zirong Ye, Fei Chen, Xin Xie, Rui Peng, Difei Xu, Qin Fan, Haichao Xu, Juan Jiang, Tong Zhang, Xinchun Lai, Tao Xiang, Jiangping Hu, Binping Xie, and Donglai Feng. In: *Nat Mater* 12.7 (2013). Article, pp. 634–640. ISSN: 1476-1122.
- [188] Y. Zhang, L. X. Yang, M. Xu, Z. R. Ye, F. Chen, C. He, H. C. Xu, J. Jiang, B. P. Xie, J. J. Ying, X. F. Wang, X. H. Chen, J. P. Hu, M. Matsunami, S. Kimura, and D. L. Feng. In: *Nat Mater* 10.4 (2011), pp. 273–277. ISSN: 1476-1122. DOI: 10.1038/nmat2981.

-
- [189] L. X. Yang, Y. Zhang, H. W. Ou, J. F. Zhao, D. W. Shen, B. Zhou, J. Wei, F. Chen, M. Xu, C. He, Y. Chen, Z. D. Wang, X. F. Wang, T. Wu, G. Wu, X. H. Chen, M. Arita, K. Shimada, M. Taniguchi, Z. Y. Lu, T. Xiang, and D. L. Feng. In: *Phys. Rev. Lett.* 102 (10 2009), p. 107002. DOI: 10.1103/PhysRevLett.102.107002.
- [190] Bo Zhou, Yan Zhang, Le-Xian Yang, Min Xu, Cheng He, Fei Chen, Jia-Feng Zhao, Hong-Wei Ou, Jia Wei, Bin-Ping Xie, Tao Wu, Gang Wu, Masashi Arita, Kenya Shimada, Hirofumi Namatame, Masaki Taniguchi, X. H. Chen, and D. L. Feng. In: *Phys. Rev. B* 81 (15 2010), p. 155124. DOI: 10.1103/PhysRevB.81.155124.
- [191] *LabVIEW 2016 Help*. URL: <http://zone.ni.com/reference/en-XX/help/371361N-01/>.
- [192] *Scienta Omicron, the provider of the Matrix software*. URL: <http://www.scientaomicron.com/en/software-downloads-matrix-spm-control/77>.

Publications and conference contributions

Publications

1. Alberto Cavallin, Vasilii Sevriuk, Kenia Novakoski Fischer, Sujit Manna, Safia Ouazi, Martin Ellguth, Christian Tusche, Holger L. Meyerheim, Dirk Sander, and Jürgen Kirschner. Preparation and characterization of $\text{Bi}_2\text{Se}_3(0001)$ and of epitaxial FeSe nanocrystals on $\text{Bi}_2\text{Se}_3(0001)$. *Surface Science*, 646 Surface science for heterogeneous catalysis, a special issue in Honour of Richard Lambert, pp. 72-82, 2016 .
2. Vasilii Sevriuk, Arthur Ernst, Antonio Sanna, Alberto Cavallin, Kenia Novakoski Fischer, Sujit Manna, Safia Ouazi, Martin Ellguth, Christian Tusche, Holger L. Meyerheim, Dirk Sander, K. Mohseni, and Jürgen Kirschner. FeSe on $\text{Bi}_2\text{Se}_3(0001)$: possible high T_c superconductor. In preparation.

Publications prior to the PhD thesis

3. G. V. Klimko, S. V. Sorokin, I. V. Sedova, S. V. Gronin, F. Liaci, V. Kh. Kaibyshev, V. A. Sevryuk, P. N. Brunkov, A. A. Sitnikova, A. A. Toropov, S. V. Ivanov. Molecular beam epitaxy of AlGaAs/Zn(Mn)Se hybrid nanostructures with InAs/AlGaAs quantum dots near the heterovalent interface. *Semiconductors*, 48(1), pp. 34-41, 2014 .
4. S. Chervinskii, V. Sevriuk, I. Reduto, A. Lipovskii. Formation and 2D-patterning of silver nanoisland film using thermal poling and out-diffusion from glass. *Applied Physics*, 114(22):224301-224301-5, 2013.
5. A. E. Aleksenskii, P. N. Brunkov, A. T. Dideikin, D. A. Kirilenko, Yu. V. Kudashova, D. A. Sakseev, V. A. Sevryuk, M. S. Shestakov. Single-layer graphene oxide films on a silicon surface. *Technical Physics*, 58(11), pp. 1614-1618, 2013.
6. V. A. Sevriuk, P. N. Brunkov, I. V. Shalnev, A. A. Gutkin, G. V. Klimko, S. V. Gronin, S. V. Sorokin, S. G. Konnikov. Statistical analysis of AFM topographic images of self-assembled quantum dots. *Semiconductors*, 47(7), pp. 930-934, 2012.

Conference contributions

1. Preparation of $\text{Bi}_2\text{Se}_3(0001)$ surface studied by scanning tunneling microscopy. V.A. Sevriuk, A. Cavallin, S. Ouazi, D. Sander, J. Kirschner. Talk, Deutschen

Physikalischen Gesellschaft, DPG, 15 March-20 March,, 2015, Berlin, Germany.

2. FeSe nanocrystals on Bi₂Se₃(0001). S. Manna, R. Shokri, H. L. Meyerheim, S. Roy, K. Mohseni, A. Cavallin, V. Sevriuk, D. Sander, J. Kirschner. Talk, Deutschen Physikalischen Gesellschaft, DPG, 15 March-20 March, 2015, Berlin, Germany.
3. Modifying the spin-dependent electronic properties of a Co nanoisland by Fe decoration. Vasilii A. Sevriuk, Soo-hyon Phark, Jeison A. Fischer, Marco Corbetta, Dirk Sander, Jrgen Kirschner. Poster, Deutschen Physikalischen Gesellschaft, DPG, 30 March-01 April, 2014, Dresden, Germany.

Appendix A

Photographs of the STM system

I present large-scale images of the STM system with the new preparation chamber, which I added during my work. The ultra-high vacuum (UHV) chamber, supported by a stainless steel frame, consisting of (separated by gate valves) the low-temperature scanning tunneling microscope chamber, newly added preparation chamber (with additional surface characterization tools) and load lock and transfer rod part are shown.

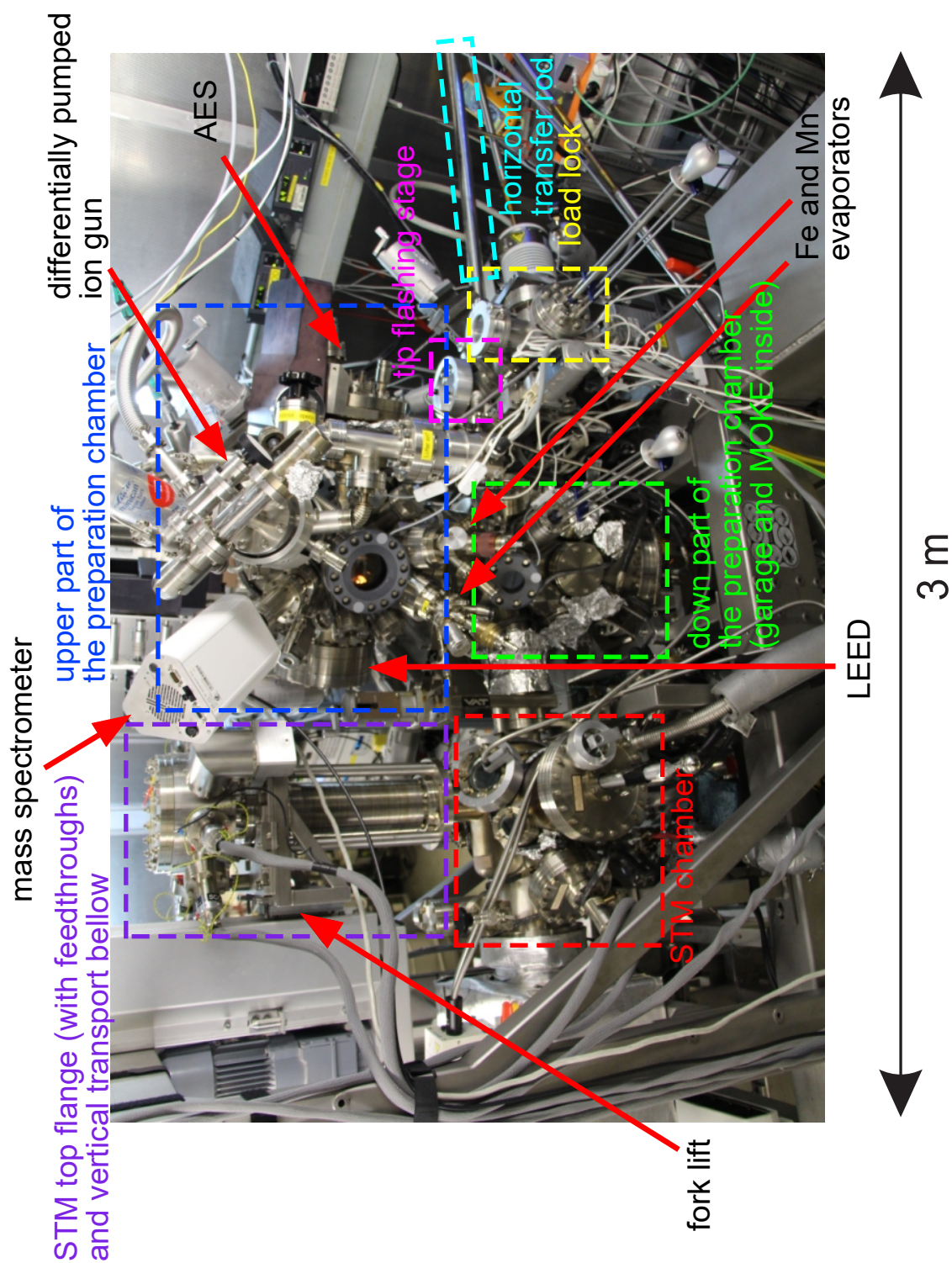


Figure A.1: South side view with STM lowered down into the cryostat.

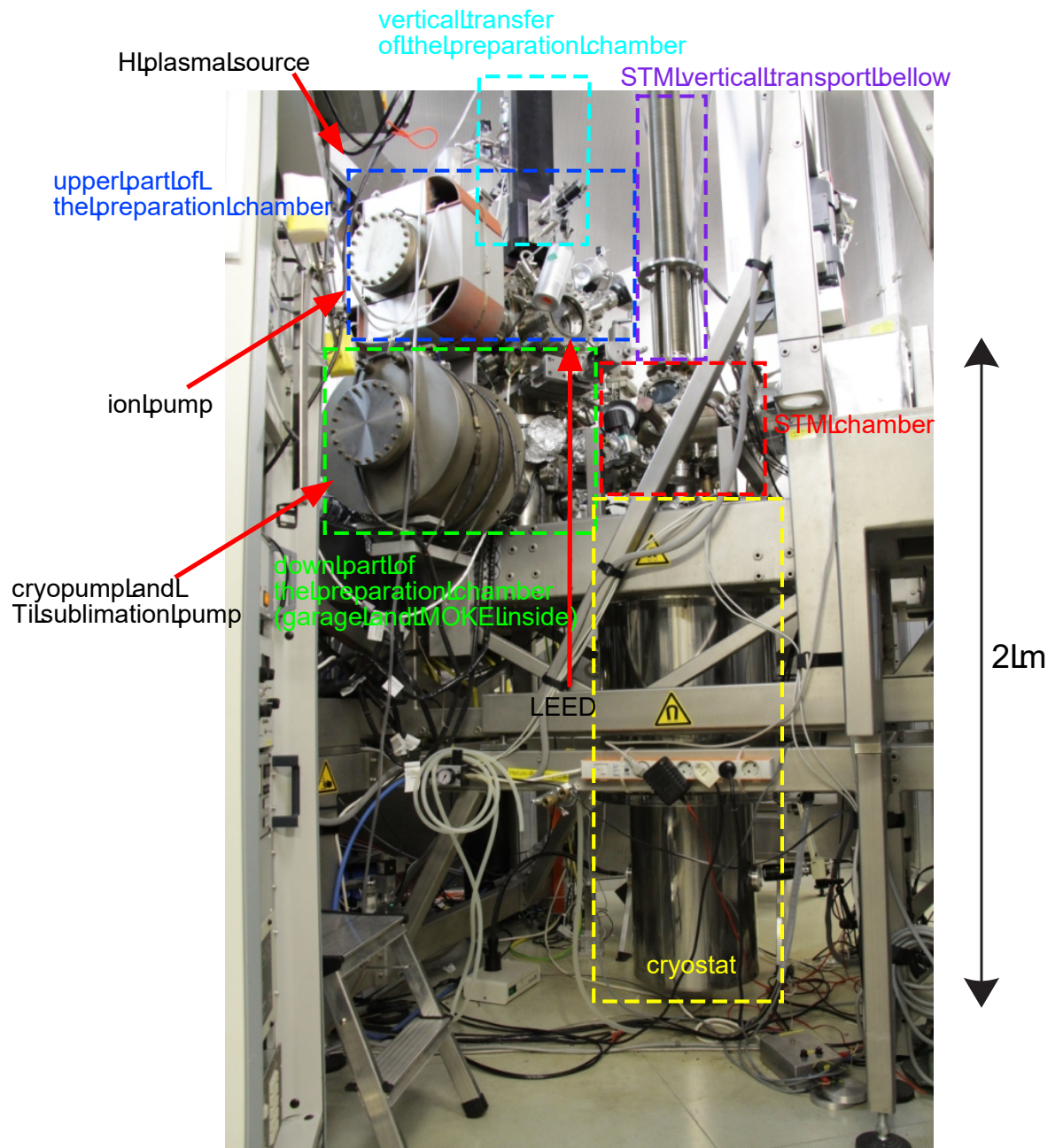


Figure A.2: North side view.

Appendix B

Example of a Matrix script and a LabVIEW program

An example of a program, which adds the lock in amplifier parameters to the Matrix file with a captured STM image, is given. The Program has two parts. The first part is a LabVIEW program [191], which requests the amplifier parameters and stores them in the buffer file, see Fig. B.1. The second part is a Matrix script [192], which takes these parameters when the STM image is saved and adds the parameters to the saved file, the script is given below:

```
//function, which implements when the STM data is ready to be
saved

function $SCOPE.Bricklet_Ready () {

//open the buffer file
var li = $SYS::IO.openTextFile("C:\\Documents and Settings
\\...lock-in.txt", false);

//read the parameters
phasvalue=$SYS::IO.read(li);
amplvalue=$SYS::IO.read(li);
freqvalue=$SYS::IO.read(li);
timecvalue=$SYS::IO.read(li);
sensunit=$SYS::IO.read(li);
sensvalue=$SYS::IO.read(li);

$SYS::IO.closeFile(li);
//end read, close the file

//assign the values with the registered foreign parameters
$SCOPE.lock_in_phase=phasvalue;
$SCOPE.lock_in_sin_ampl=amplvalue;
```

```
$SCOPE.lock_in_sin_freq=freqvalue;
$SCOPE.lock_in_time_constant=timecvalue;
$SCOPE.lock_in_sensitivity=sensunit+" "+sensvalue;
}

function main() {

    //register foreign parameters in the Matrix program when the
    script is started

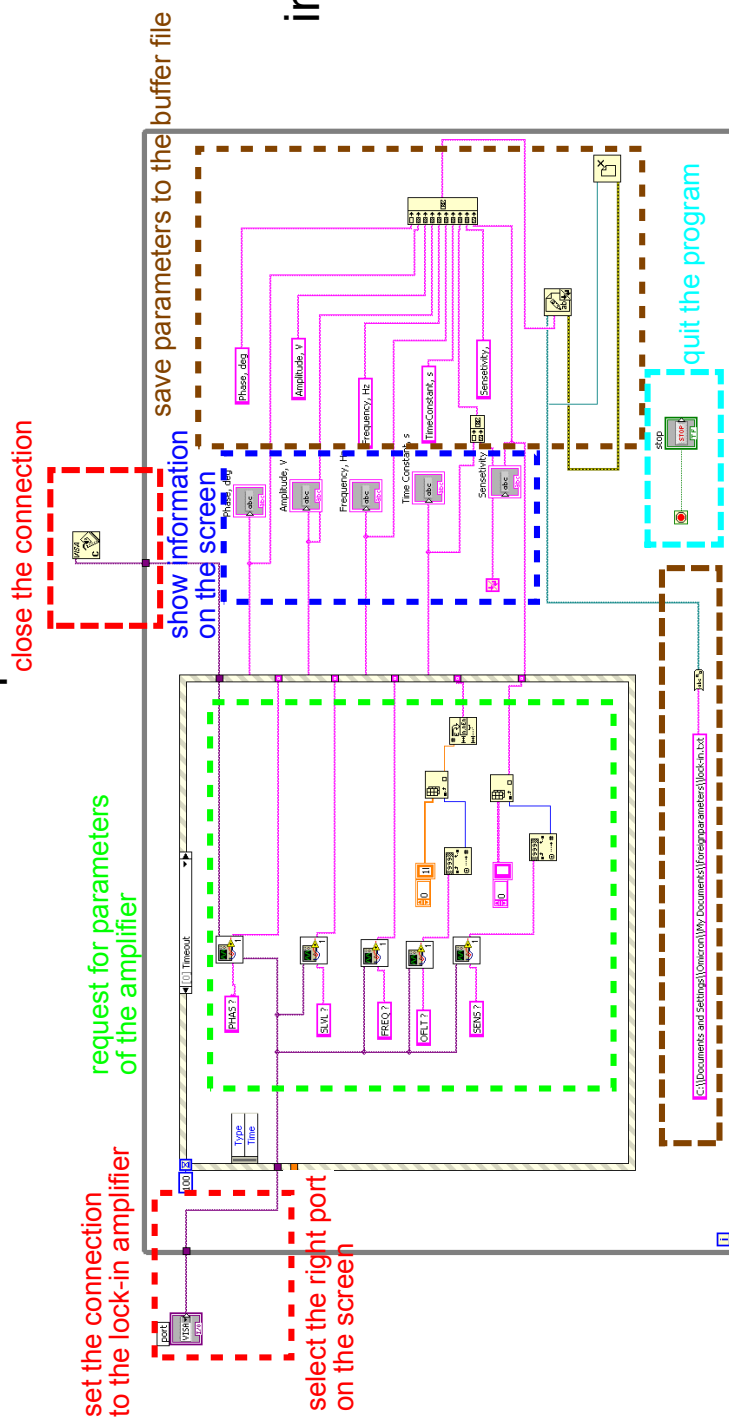
    $SCOPE.addForeignParameter("lock_in_phase", "double", "deg", 0.0);
    $SCOPE.addForeignParameter("lock_in_sin_ampl", "double", "V", 0.0);
    $SCOPE.addForeignParameter("lock_in_sin_freq", "double", "Hz", 0.0);
    $SCOPE.addForeignParameter("lock_in_time_constant", "double", "s", 0.0);
    $SCOPE.addForeignParameter("lock_in_sensitivity", "string");
}

function on_abort() {

    //remove the registered foreign parameters from the Matrix pro-
    gram when the script is switched off

    $SCOPE.removeForeignParameter("lock_in_phase");
    $SCOPE.removeForeignParameter("lock_in_sin_ampl");
    $SCOPE.removeForeignParameter("lock_in_sin_freq");
    $SCOPE.removeForeignParameter("lock_in_time_constant");
    $SCOPE.removeForeignParameter("lock_in_sensitivity");
}
```

LabVIEW implementation scheme



interface of the program

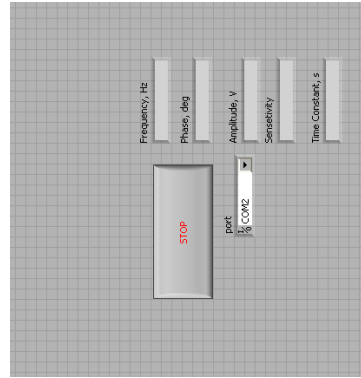


Figure B.1: LabVIEW program, which was developed to request the lock in amplifier parameters and to store them in the buffer file.

Acknowledgements

I am indebted to my supervisor PD Dr. Dirk Sander for his constant support of my work and professional growth. His kindly guidance is difficult to overestimate.

I would like to express my indebtedness to Dr. Ilya Kostanovskiy, Dr. Antonio Sanna and Dr. Jeison Fisher for the valuable discussions, which helped me to improve my manuscript.

I am grateful to our collaborators from the theory department and other labs for their contributions to my work and helpful discussions. In particular, I would like to thank Dr. Arthur Ernst, Dr. Antonio Sanna, Dr. Martin Ellguth, Dr. Christian Tusche, Dr. Holger L. Meyerheim, Dr. Roozbeh Shokri, Dr. Sumalay Roy, Dr. Katayoon Mohseni and Prof. Jürgen Kirschner.

I am very thankful to all my friends and colleges from the 3He-STM, Cryo-STM and Stress labs: Sujit Manna, Augusto Leon Vanegas, Alberto Cavallin, Michael Caminale, Agnietzka Stepniak, Hirofumi Oka, Soo-Hyon Park, Jeison Fisher, Wolfgang Greie, Jörg Prempfer, Kenia Novakovski and Safia Ouazi for their help, contributions, comments and encouragement.

A special acknowledgment to the staff from the electronic, mechanical workshops and administration for the technical and administrative support and to all my colleges from the Max Planck Institute for their collaboration.

Last, but not least I would like to express my gratitude to my friends, to my family and specially to my wife for their support and cheer.

Curriculum vitae

Personal details

Name: Vasili Sevriuk
Date of birth: 29 December 1989
Sex: male
Place of birth: Leningrad, USSR
Nationality: russian
Marital status: married
Present address: Friesenstrasse, 06112, Halle (Saale), Germany
Email: vsevriuk@mpi-halle.mpg.de

Education

- 10/2013 – present Doctoral Fellow at Max Planck Institute of Microstructure Physics, Halle, Germany
- 09/2011 – 12/2013 Master of Science, Physics and Technology of Nano-Structures, St.-Petersburg Academic University, St.-Petersburg, Russia. Topic of thesis: *Monolayer GO (graphene oxide) film conductivity, after the reduction in molecular hydrogen flow.*
- 09/2007 – 07/2011 Bachelor of Science, Technical Physics, Saint-Petersburg State Polytechnical University, St.-Petersburg, Russia. Topic of thesis: *Atomic force microscopy study of detonation nanodiamonds.*

Erklärung an Eides statt

Hiermit erkläre ich, dass ich die vorliegende Arbeit selbstständig und ohne fremde Hilfe verfasst, andere als die von mir angegebenen Quellen und Hilfsmittel nicht benutzt und die den benutzten Werken wörtlich oder inhaltlich entnommenen Stellen als solche kenntlich gemacht habe.

Eine Anmeldung der Promotionsabsicht habe ich an keiner anderen Fakultät einer Universität oder Hochschule beantragt.

Halle (Saale), 26.10.2016

Vasilii Sevriuk